SUBMARINE ERUPTIVE PROCESSES IN THE BROOK ST TERRANE AT COLAC BAY, SOUTHLAND, NEW ZEALAND

JASMINE MAWSON

A thesis submitted in fulfilment of the requirements for the degree of Master of Science

Department of Geology

University of Otago

Dunedin, New Zealand

October, 2018

Acknowledgements

Firstly I would like to thank my supervisor James White for his support, advice, and interesting questions, and co-supervisor Mike Palin for his guidance on matters geochemical and his help with the facilities at the Centre for Trace Element Analysis. Thanks also to Marco Brenna for his ideas and discussion.

I have benefited from the technical expertise of several other people at the Geology Department. Thank you to Brent Pooley for help in the thin section lab and for making polished sections for me. Thanks to Marianne Negrini for operating and teaching me to use the Scanning Electron Microscope, and the Otago Centre for Electron Microscopy for use of this equipment. Thanks to Gemma Kerr for advice on preparing samples for trace element geochemistry.

The Geology Department's volcanology group has provided interesting and useful discussion, and plenty of silliness. My thanks go particularly to Rosie Cole for organising meetings and providing cake. My fellow Masters students in the Department have also provided much-appreciated mutual support and encouragement.

My gratitude goes to Jenna Halder of Te Hikoi Museum and Information Centre, an invaluable contact in Riverton whose local geological knowledge and enthusiastic support has enhanced my visits there. Thanks also to the local landowners, Don Moir and Nola Goble, who allowed me access to or through their properties to look at rocks.

Finally, my heartfelt thanks go to my parents, Bill Mawson and Sue White, for their love, encouragement, and tactical assistance.

List of Contents

List of Figures

Abstract

A sequence of volcanic and volcaniclastic rocks of the Brook Street Terrane crops out along the Southland coast from Howells Point, Riverton, into Colac Bay. This sequence provides an along-strike exposure, revealing lateral variations in these submarine deposits of a Permian oceanic island arc; such sequences are rarely studied, and allow examination of an arc environment within a thin slice of time, in a manner which is impossible in the more common vertical sequences.

Lithofacies analysis and mapping, and geochemical analyses were carried out. The sequence includes pillow lavas, dikes, hydroclastic breccias, tuffs, lapilli tuffs and argillites. All is hydrothermally altered and metamorphosed to prehnite-pumpellyite facies, so major and trace element analyses were conducted on the freshest augite phenocrysts wherein the magmatic signal is likely to be preserved.

Geochemical data indicate variable primitive island arc to MORB-like magma sources. Two distinct groups of signatures exist, one with typical island arc characteristics, the other more closely resembling back-arc (MORB-like) magma. The distribution of these suggests two separate small volcanic centres, perhaps tapping different mantle domains in a source region transitional between the arc and back-arc. The size and proximity of the two may indicate they are satellite vents of a larger arc volcano.

The sedimentary structures and facies relations of tuffs and lapilli tuffs suggest formation in association with pillow lava as hyaloclastite, and redeposition by subaqueous mass flows. The pillow lavas observed have peperitic contacts with the volcaniclastic rocks, indicating that they intruded into these deposits while they were unconsolidated. These relationships indicate that two generations of pillow lava formed in the sequence, the first associated with production of hyaloclastite which was redeposited in fans and channels on the volcano flanks, and the second intruding into these deposits.

1. Introduction

1.1 Motivation

This thesis presents results from a study of Permian arc-derived rocks of the Brook Street Terrane, exposed along the southern coast of New Zealand's South Island, near Riverton. The aim of the work is to characterise lateral, and to a lesser degree, vertical changes through a well-exposed succession of submarine-emplaced island arc rocks. What eruption processes were dominant, how were lavas and primary volcaniclastic debris emplaced, and what, if any, was the role of longer-distance transport of volcaniclastic sediment in producing this succession? Does the succession represent a single eruption, or even a single volcano?

Submarine volcanoes are abundant in the modern ocean, their coherent and volcaniclastic deposits are abundant globally, and they host many significant economic deposits (e.g. White et al., 2003). Despite their significance, much remains to be learned about their emplacement, particularly in the context of different volcanic settings on the seafloor. The Riverton section holds information about processes of eruption and sedimentation in an oceanic island arc. Its extensive along-strike exposures reveal lateral environments in a thin slice of time during the development of the Brook Street Terrane, and give a view of the Permian arc seafloor that is highly complementary to that analysed by Houghton and Landis (1989) based on ridge-crest exposures of subvertically dipping strata in the Takitimu Mountains.

1.2 The Brook Street Terrane

The Brook Street Terrane comprises Permian ocean island volcanic arc rocks. It is over 400 km long (Spandler et al., 2005) and a thickness greater than 14 km is exposed (Bradshaw, 1994). According to Haston et al. (1989), oxygen isotopic and paleomagnetic data indicate that it formed at a low paleolatitude and is allochthonous to the Gondwana margin. Price et al. (2006) and Spandler et al. (2003, 2005) classify the Brook Street Terrane as a primitive oceanic arc. Spandler et al. (2005) also posit that the Brook Street volcanics were part of an extensive island arc in Permian times, which also included the

Australian Gympie Terrane and the Tembera Terrane of New Caledonia. Conversely, according to Haston et al. (1989) and Price et al. (2006) the terrane comprises parts of several fragmented Permian arcs of subtly different ages and compositions, all accreted to the Gondwana margin. The polarity of the subduction zone is not established, although Bradshaw (1994) suggests that its structure implies subduction eastwards away from the Gondwana margin.

The Brook St Terrane includes intrusive and extrusive rocks, mostly basaltic to andesitic in composition, volcaniclastic material, and sedimentary units of the associated back-arc basin (Houghton and Landis, 1989, Haston et al., 1989, Spandler et al., 2005). The environments of volcanism ranged from deep submarine to marginally emergent, and volcanism included effusive and explosive eruptions (Houghton and Landis, 1989). Elsewhere in the basin turbidite sedimentation predominated, and some volcaniclastic sediments show evidence of having been redeposited in this way; steep and unstable near-vent slopes are prone to collapse and trigger mass flows (Houghton and Landis, 1989).

The extrusive volcanic rocks of the Brook Street arc are of a primitive island arc tholeiitic series (Sivell and Rankin, 1983, Spandler et al., 2005), and Spandler et al. (2005) assert that the parent magmas were ankaramitic in composition. The arc is immature, with no continental input (Houghton and Landis, 1989, Spandler et al., 2005). Systematic geochemical variation along the terrane has not been observed, so Spandler et al. (2005) attribute variability to magmatic differentiation within the crust.

The Brook Street rocks are hydrothermally altered, and regionally metamorphosed to prehnite-pumpellyite facies, which indicates burial to between ~2 and 10 km depth (Spandler et al., 2003). According to Sivell and Rankin (1983) these processes have altered the deposit mineralogy significantly, but movement of elements is generally on a local scale and has caused little change in the geochemistry of whole-rock samples. Strata are also folded in a series of open anticlines and synclines (Mortimer et al., 1999).

A wide range of ages, all within the Permian, have been published for the Brook Street Terrane rocks. Fossil ages range from Sakmarian to Wuchiapingian (~288 to 253 Ma) (Mortimer et al., 1999). Ar-Ar ages from intrusive rocks range from 252-249 Ma (Mortimer et al., 1999), while U-Pb zircon ages were interpreted by Mortimer et al. (1999) to indicate two intrusive events at 261 and 292 Ma respectively. Price et al. (2006)

interpret these data to indicate that the Brook Street intrusive rocks were emplaced quickly over a few million years around 260 Ma; this is supported by their primitive nature, because a long period of emplacement would produce evidence of crustal recycling. In contrast, Spandler et al. (2005) contend that the radiometric dates correlate with the youngest fossil ages, and that together they could represent the cessation of volcanism in the arc. Mortimer et al. (1999) suggest that the Brook Street Terrane was accreted to the Gondwana margin at 230-245 Ma (during the Triassic).

1.3 Submarine Volcanism

Most island arc volcanoes are stratovolcanoes (Cas, 1992). The general structure of a stratovolcano includes lavas, primary and reworked volcaniclastic rocks, and intrusions (e.g. de Silva and Lindsay, 2015), formed by repeated eruptions in the same location (Manville et al., 2009). On submarine stratovolcanoes, small-volume debris flows and larger volcaniclastic turbidity currents, triggered by gravitational instability or eruption, are common (Kralj, 2012); such particle remobilisation, both subaerially and underwater, typically results in a large apron of volcaniclastic material surrounding the volcano (Manville et al., 2009). Such aprons are divided into the proximal apron, dominated by coarse clasts, with steep slopes promoting slumping; the medial apron with gentler slopes and deposits recording explosive activity and debris flows; and the distal apron, dominated by finer-grained volcaniclastic material deposited by suspension settling and/or dilute turbidity currents (Allen et al., 2007), often mixing with and grading into ambient sedimentary deposits (Kralj, 2012). Satellite vents may provide direct input of lava to the apron (Allen et al., 2007). The size of the apron may range from a few kilometres (Kralj, 2012) to tens of kilometres (Cas, 1992, Allen et al., 2007).

Aprons are dominated by sedimentary processes, and structures such as fans, ramps, and canyons (Orton, 1996). There are a restricted range of transport processes which may operate on particles, and thus a limited set of sedimentary structures they may display (McPhie et al., 1993). Clasts may move together with interstitial fluid and interact in mass flows, behave independently while entrained in moving fluid (traction transport), or move suspended in fluid in suspension transport (McPhie et al., 1993). Flows may form as a direct result of volcanic activity, such as pyroclastic flows or surges, or as redeposition of loose material formed by volcanic activity, such as avalanches or turbidity

currents (McPhie et al., 1993). The deposition of these various types of flows builds the apron. Flows with point sources, such as satellite vents or canyon structures, may produce submarine fans (Nichols, 2009). Avalanches may produce scar and slump structures (Orton, 1996). Channels and canyons occur where erosion is dominant (Gamberi, 2001); they may form levees where the upper, more dilute part of a flow overspills their banks, and currents commonly spread out to form fans at the ends of channels (Nichols, 2009). Submarine fans form a number of depositional lobes, each comprising a succession of mass flow deposits which prograde over time and shift as their local gradients change (Nichols, 2009).

Submarine eruptions may be effusive or explosive, though explosive eruptions are less common, as most submarine eruptions are of basaltic magmas which have lost volatiles during ascent (White et al., 2015). Explosive activity can be a result of magma reaching the surface with its original volatiles, or of rapid heat transfer from magma to water (White et al., 2015). The explosivity of a subaqueous eruption is controlled by depth, the properties of the magma (composition, temperature, volatile content, viscosity, etc.), rate and volume of magma discharge, vent geometry, and magma-water interaction (Cas, 1992, Portner et al., 2010).

When eruptions are effusive and submarine, pillow lava is a common form for lava flows to take. An outer edge of the lava flow chills in the cold water to produce a glassy rind, which insulates the rest of the flow. Lava flows into the bulbous shape thus formed until the crust is too thick and hard for further inflation; at this point, either the crust fails and a new pillow forms at the leading edge of the flow, or flow is redirected within the feeder system to produce pillows elsewhere (White et al., 2015). This results in a stack of branching pillow lobes growing slowly away from the vent, fed by larger lava tubes that divide to feed the lobes (Moore, 1975). Pillows accumulate both laterally and vertically, piling on top of one another, commonly resulting in high-relief piles which do not extend far from the source vent (White et al., 2015). Pillows may experience multiple pulses of lava, leaving them with concentric zones of vesiculation (Duraiswami et al., 2013). Wells et al. (1979) assert that the depth of water pillow lava is erupted into dictates the vesicularity, with shallower water corresponding to larger, more abundant vesicles; this is due to the confining pressure of water (Jones, 1969). More recent work (e.g. Hekinian et al., 2000) places more importance on the initial volatile content of the magma; high volatile content will result in greater vesicularity for a given depth than lower volatile

content. Cas (1992) adds that the sizes of pillows are controlled by magma eruption rate, viscosity (controlled mainly by composition and temperature), and the slope they are erupted onto, resulting in variation in size between flows and within single flows.

When magma intrudes into unconsolidated sediment, intrusive pillows, irregular lobes, and peperite may form. The magma stalls, disintegrates and mingles with the sediment, and the heat of the magma causes water in the sediment to expand, pushing grains apart and allowing the mixture to behave as a viscous fluid (White et al., 2015). Magma may fragment by quenching, mechanical stress, magma-sediment density contrasts, surface tension, fluid shearing, or hydromagmatic explosions, and a mixture of these processes is likely to operate to form any given peperite (Skilling et al., 2002). Magma and host sediment mingle through forceful intrusion of magma, liquefaction and/or fluidisation of sediment, and hydromagmatic explosions (Skilling et al., 2002). Peperite may be blocky (with blocky juvenile clast shapes formed by brittle quenching) or fluidal (with bulbous juvenile clast shapes formed by ductile fragmentation of low-viscosity magma) (Doyle, 2000, Portner et al., 2010). It may have a closely-packed fabric with jigsaw-fit between clasts or sediment-filled fractures between pseudo-pillows, or a dispersed fabric forming a matrix-rich breccia (Doyle, 2000). The presence of peperite establishes that magmatism and sedimentation were approximately contemporaneous where it occurs, and thus is important in paleoenvironmental reconstruction (Skilling et al., 2002).

Hyaloclastite is a clastic deposit of fragmented lava that forms by quenching or other brittle-state fragmentation, as when lavas flow over steep subaqueous slopes or come into contact with cold water, chilling and producing thermal stresses (Cas, 1992, White et al., 2015). Hyaloclastite may occur as pillow breccia, or consist of smaller clasts of microcrystalline lava (White et al., 2015). It is common for hyaloclastite to slump down the steep face of the lava that generated it, or be redeposited by mass flows; these processes enable it to extend for tens of metres of vertical section, and considerable lateral distances (Cas, 1992).

1.4 This study

The studied coastal section crops out along the Southland coast from Howells Point, Riverton, into Colac Bay (fig. 1). This sequence includes pillow lavas, dikes, tuffs, lapilli tuffs, hydroclastic breccias that include hyaloclastite, and argillites. It is well-exposed for 8 km along strike in a section 220 m thick that reveals lateral variations in deposits of an oceanic island arc; such sequences are rarely studied, and provide different constraints on arc volcanism than do the more common vertical sequences. The whole sequence is hydrothermally altered and lightly metamorphosed to prehnite-pumpellyite facies, and deformed into a series of open folds striking NW-SE. Detailed mapping, lithofacies analysis, and geochemical analysis were undertaken in order to ascertain the eruptive processes of the succession, the environment of deposition and emplacement, the magmatic conditions, and the sequence of events.

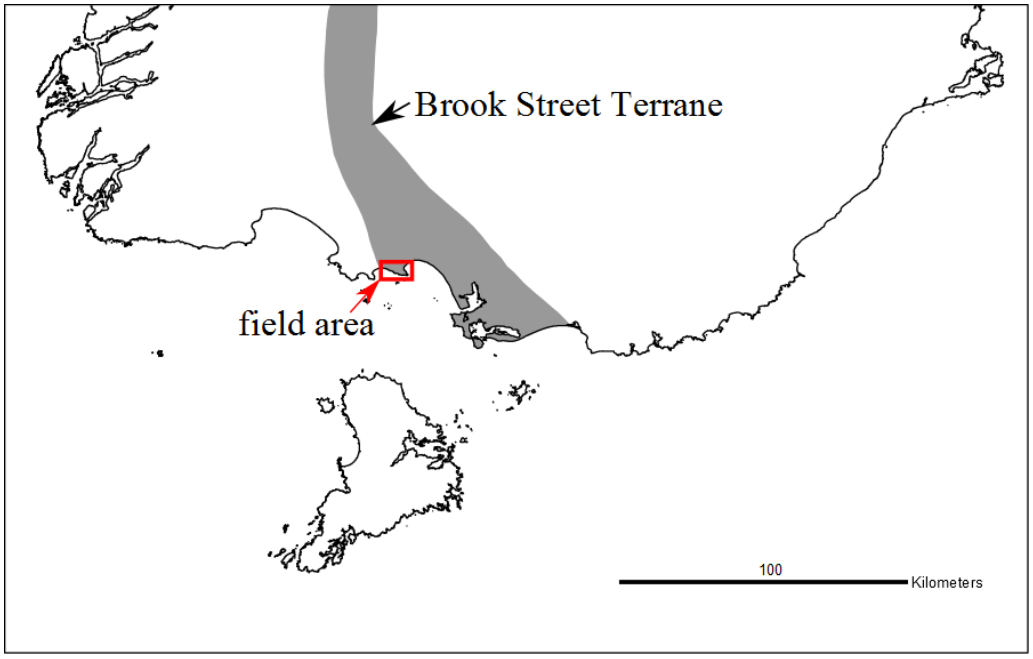

Figure 1: location map; box shows the location of the field area on the southern coast of New Zealand and relative to the Brook Street Terrane; the western contact of the terrane is not exposed on this coast.

2. Lithofacies

Field description, mapping and thin section analysis were carried out to ascertain the nature of the lithofacies, the relationships between them, and to understand the processes by which they formed. A geological map is presented in Plate 1. The nomenclature of White and Houghton (2006) is used. Detailed mapping was possible along the coast from Riverton into Colac Bay, with a few exposures inland used to constrain relationships with rocks not exposed (fig. 2).

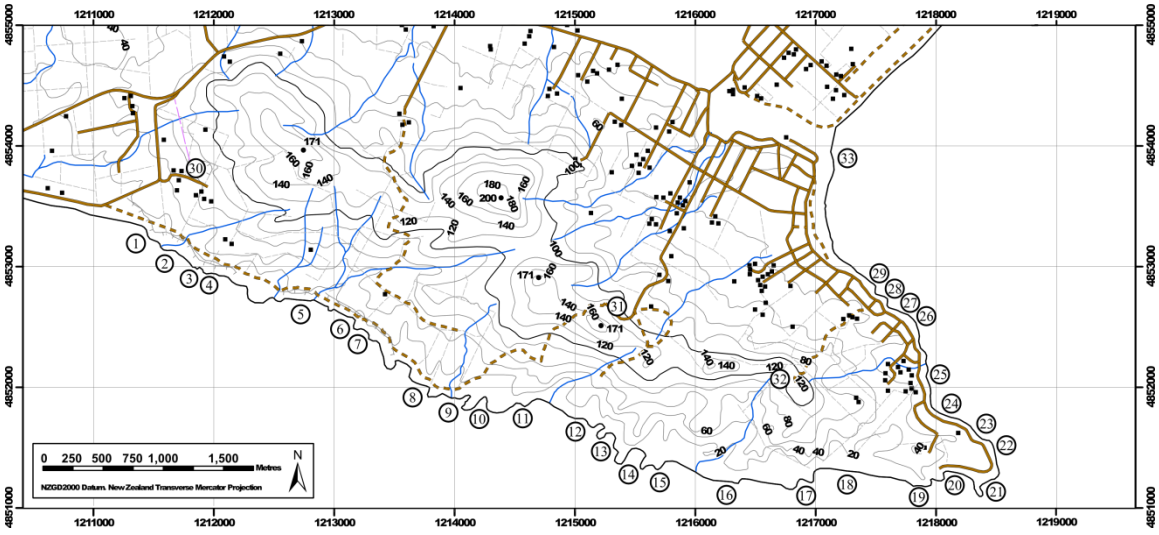

Figure 2: map showing field localities; site numbers are in reference to this map, and thin section numbers also refer to the site from which the sample was collected.

A cross-section along the coast displays the relations between lithofacies (fig. 3). Lapilli tuff forms channels in tuff (see section 2.3 for full description), argillite overlies and interbeds with tuff, and pillow lava intrudes into both of the former.

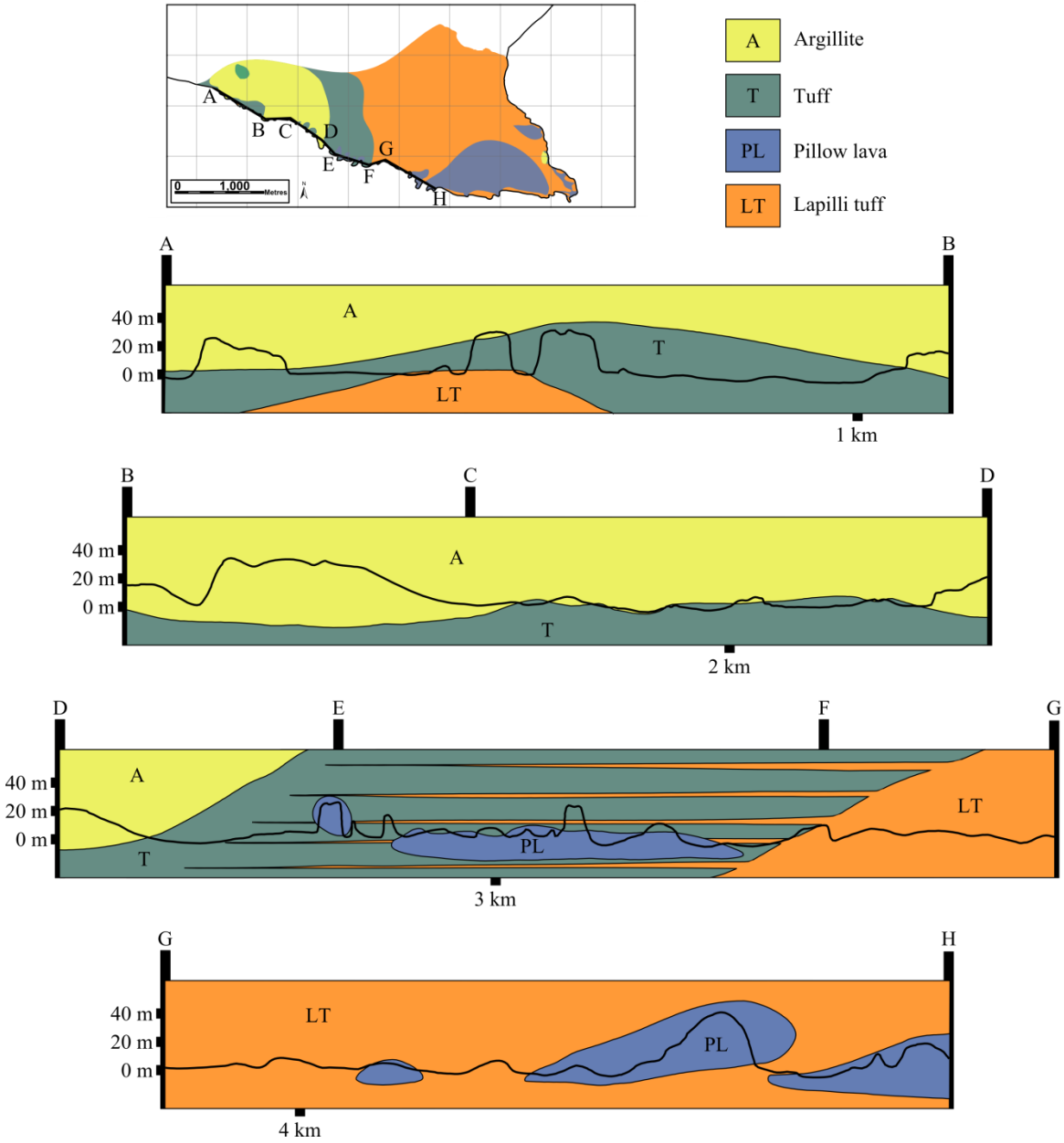

Figure 3: cross-section along the coast (inset map shows location), showing lateral relationships between lithofacies. This section is vertically exaggerated so relationships can be seen in detail. The strips of lapilli tuff in section E-F are a schematic representation of the channel zone (see section 2.3). Argillite and tuff interbedding are not shown.

2.1 Pillow Lava

Pillow lava in the study area crops out mostly as cliffs. It is dark green in colour and displays the prominent pillow lava morphology of sacklike forms filling into the depressions between older pillows (fig. 4a). This shaping makes it clear that the younging direction is upwards throughout the pillow lava formations. Pillows are aphanitic to sparsely porphyritic (1-3 mm phenocrysts), and contain many amygdales which are notable in outcrop, including quartz, chlorite, prehnite and pumpellyite.

Pillow rinds are commonly absent, but in a few places they are visible; darker coloured, sometimes reddish, rock with cracks between it and the body of the pillow. A glassy appearance is never preserved. The quantity of amygdales increases towards the rims of the pillows. In some places (sites 12 and 20) the pillows are weathered leaving the amygdales standing out in relief. A few pillows display concentric layers of amygdales (fig. 4b). At sites 12, 13 and 26 some pillows have a centre of ~10 cm composed entirely of the same material filling the amygdales. Some of these also have concentric rings of amygdales, while others do not. At site 12 there are also a few places with a large (~1 m) core of quartz-replaced rock with 10-20 cm rims of basalt.

Pillows vary in size from 10-50 cm. At sites 15 and 16 they are unusually small, 10 cm on average, and more oval in shape than the larger pillows. In a few localities (sites 16, 18, 19, and 20), the outcrop exposed is sufficiently three-dimensional to reveal the elongate lateral sides of the pillows. At site 20 these are elongate E-W, with a shallow eastward dip, although in the cliff at the same orientation at site 19, immediately below, such shapes are not visible. At site 18, elongate pillows have curving forms, drooping over the pillows below and dipping S (fig. 4c). At site 16 they also plunge southwards.

In some areas there is matrix visible between the pillows (fig. 4d). At sites 13, 16, 17, 18, and 27 this inter-pillow matrix is pale green with dark angular clasts, resembling the lapilli tuff below. At site 15 the matrix is paler in colour and has a sandy texture, with scattered small crystals and a few distinct basalt clasts; in places here the matrix is absent. The matrix at site 10 is similar, but here it is often weathered deeply between pillows. The matrix is invariably highly altered by hydrothermal metamorphism, in many places to the extent that its primary texture is not distinguishable. In these cases (in places at sites 16, 17, 18, and 27) it is coarsely crystalline and appears mottled, composed of large crystals of prehnite, quartz and chlorite that replace the original matrix (fig. 4d). In one location at

site 17, it appears to have widely scattered highly altered basaltic clasts with concentric layers of recrystallised material around and between them. At site 16, in addition to the pillows being smaller, they are more separated, with the matrix between them more dominant.

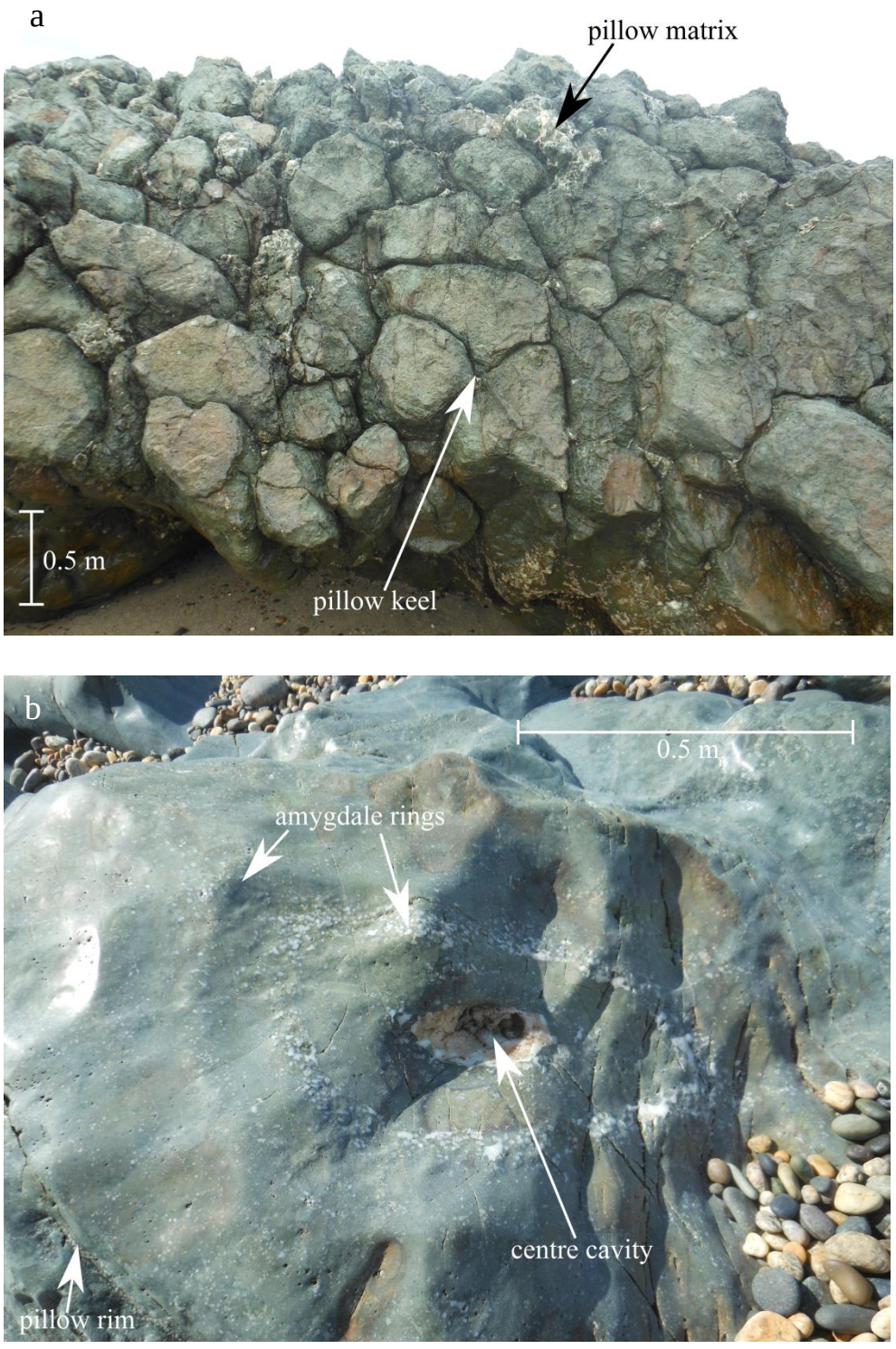

Figure 4: a and b (caption below).

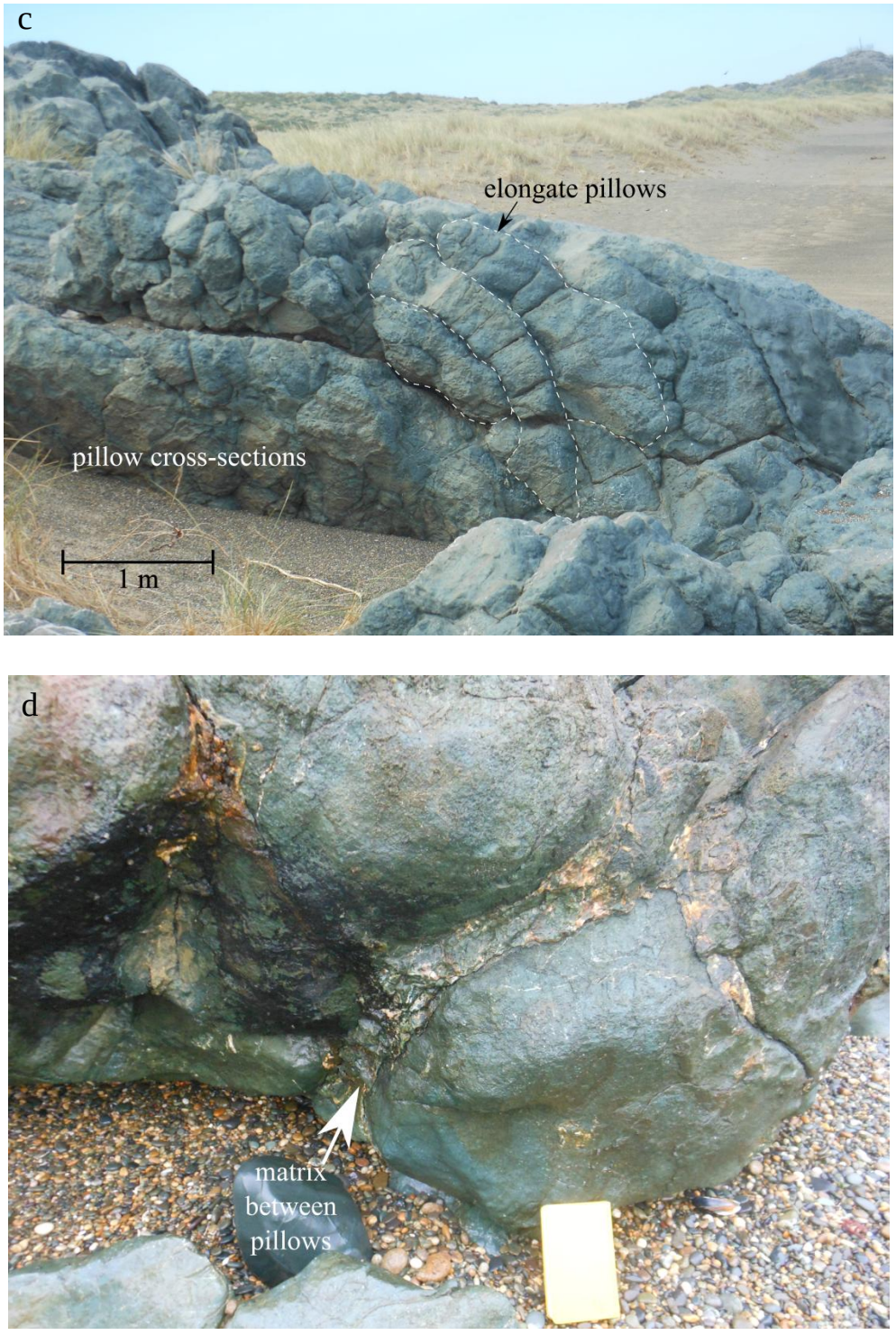

Figure 4 continued: a) pillow lava pile at site 21, showing the keel shapes of pillows filling into gaps between those below, and places where coarsely recrystallised inter-pillow matrix is visible; b) pillow at site 19 with concentric rings of vesicles and a centre cavity composed of the same material (in this case quartz): a crack marks the rim of the pillow; c) elongate pillows in outcrop at site 18, drooping over the underlying pillows and showing that pillows propagated in multiple directions over the area of a single outcrop; d) coarse recrystallised inter-pillow matrix filling the space between pillows at site 27 (notebook for scale is 20 cm lengthways).

2.1.1 Petrography

The pillow lavas are finely crystalline (<0.01-0.5 mm), with a groundmass composed primarily of albite and clinopyroxene, with some chlorite and pumpellyite alteration. The albite occurs in laths with random orientation, whereas the clinopyroxene is present as subhedral crystals. Phenocrysts are sparse and comprise 0.5-1 mm albite crystals. Some clinopyroxene occurs in glomerocrysts up to 0.4 mm across in sample 21a.

Amygdales, 2-6 mm, are abundant in all the pillow lavas, and commonly filled with quartz, chlorite, prehnite, pumpellyite, or some combination of these. Some amygdales have a rim of pumpellyite with quartz in the centre; in sample 20 many of these comprise fine radiating bundles of crystals at the rim, with scattered larger pumpellyite crystals in the centre surrounded by optically continuous quartz (fig. 5a). Some in sample 21a have a wide rim of quartz with a chlorite centre, while others include distinct crystals of albite within an amygdale filled mostly with pumpellyite. Those amygdales that are dominated by quartz comprise several large interlocking crystals, while those filled solely with chlorite or pumpellyite are of numerous very fine crystals.

Pillow lava sample 20 has regions with contrasting amounts and sizes of crystals on the scale of 5-20 mm; more coarsely crystalline areas with large (0.05-0.5 mm), prominent albite laths, and more finely crystalline areas with very small (<0.05 mm) albite laths, wherein the clinopyroxene crystals (with relatively consistent sizes) are more prominent (fig. 5a). Some of the finer regions occur around amygdales (fig. 5b), and chlorite is more abundant in these.

Pillow lava sample 21a is more coarsely crystalline than sample 20, and chlorite occurs in larger crystals, frequently with cores of pumpellyite. There are many regions darker in colour and with finer crystals, dominated by pumpellyite and chlorite, surrounding amygdales; this is particularly common around the irregular-shaped vesicles, where the darker regions have smoother rounded outlines (fig. 5c). These could be the ‘segregation’ vesicles described by Caroff et al. (2000) and Schipper et al. (2012), wherein rapid melt segregation produced extrusions of melt into vesicles. Here the rounded outlines would be the shapes of the original vesicles, and hydrothermal and metamorphic alteration would have obliterated the original glassy textures expected in such features. Elsewhere in the slide is a crack with iron-staining extending from it.

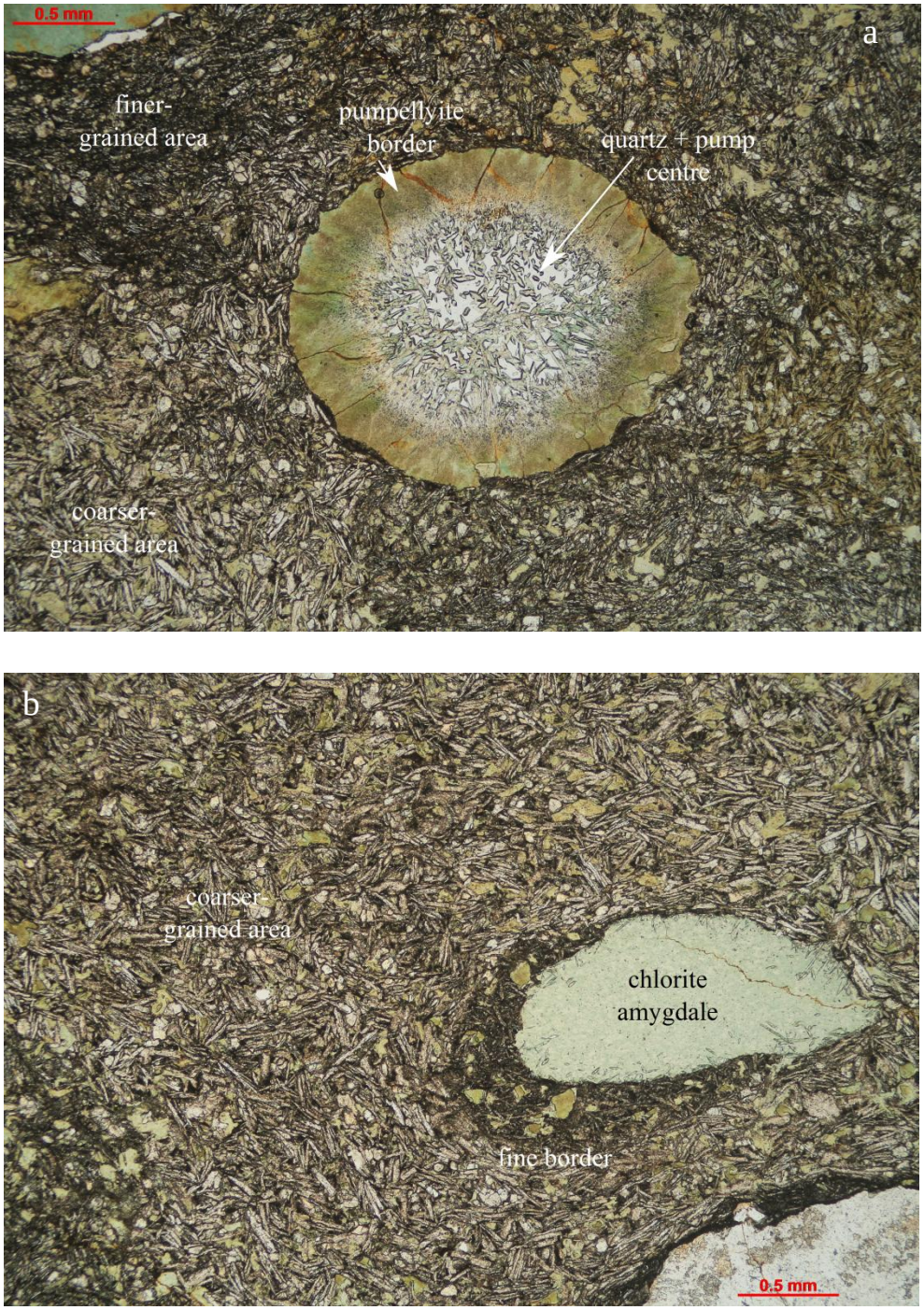

Figure 5: a) amygdale in sample 20 showing pumpellyite rim and mixed centre: regions with different crystal sizes are also visible; b) more finely crystalline region forming a rim around a chlorite amygdale in sample 20.

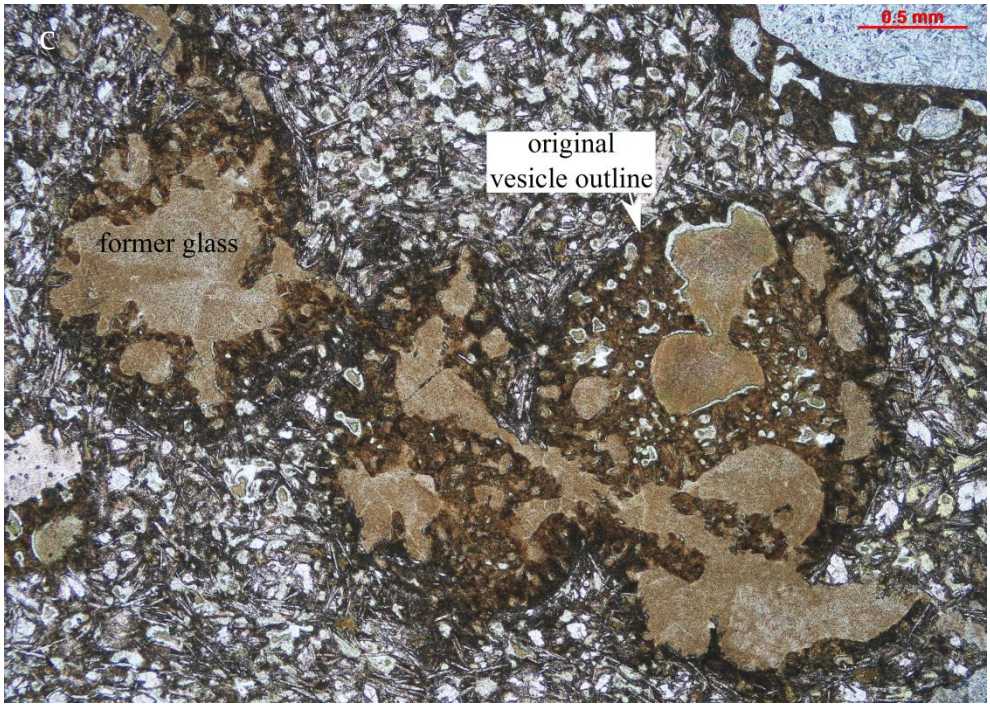

Figure 5 continued: c) segregation vesicles altered to pumpellyite in sample 21a.

2.1.2 Inter-pillow matrix petrography

Two distinct textures of inter-pillow matrix are observed, both of them highly altered and recrystallised.

Sample 15 consists largely of finely crystalline calcite and quartz with complex interlocking textures. While in outcrop the site this sample was taken from appeared to have a fine sand-grained clastic matrix, little evidence of this clastic texture is discernible in thin section. A few scattered crystals throughout the slide retain distinct crystal forms rather than recrystallised texture. Based on these and the basalt clasts visible in outcrop, this rock could originally have been a tuff with crystal clasts of albite and pyroxene, and small lithic fragments. The larger regions of quartz are polycrystalline and have undulose extinction. Faint layering is present, demarked by layers with a greater proportion of larger quartz grains juxtaposed with finer, more calcite-dominated layers. Titanite crystals are rare, scattered throughout the slide; many of them are irregular in shape and bear inclusions of calcite. A quartz vein runs through the slide, 0.1-0.6 mm in thickness, with uneven edges and several jogs (fig. 6a). At one end of the slide is a region with much coarser (0.2-0.5 mm) texture, with large areas dominated by calcite and polycrystalline

quartz, respectively. This region is separated from the rest of the slide by a narrow, opaque wavy line (fig. 6b).

Sample 27 comprises extremely coarse (up to 6 mm) recrystallised quartz, prehnite and epidote, with abundant smaller interlocking laths of chlorite between and within the large crystals. The large crystals have undulose extinction; the prehnite occurs in bundles of crystals which the extinction sweeps across. Some regions of quartz are polycrystalline. Within the slide are several dark, irregularly-shaped regions that include the pseudomorphed shapes of phenocrysts and amygdales (fig. 6c). The former phenocrysts are euhedral and tabular, and most are composed of small crystals of chlorite, although a few are instead composed of quartz. The amygdales are either of small radial chlorite crystals, or have a rim of these with quartz centres.

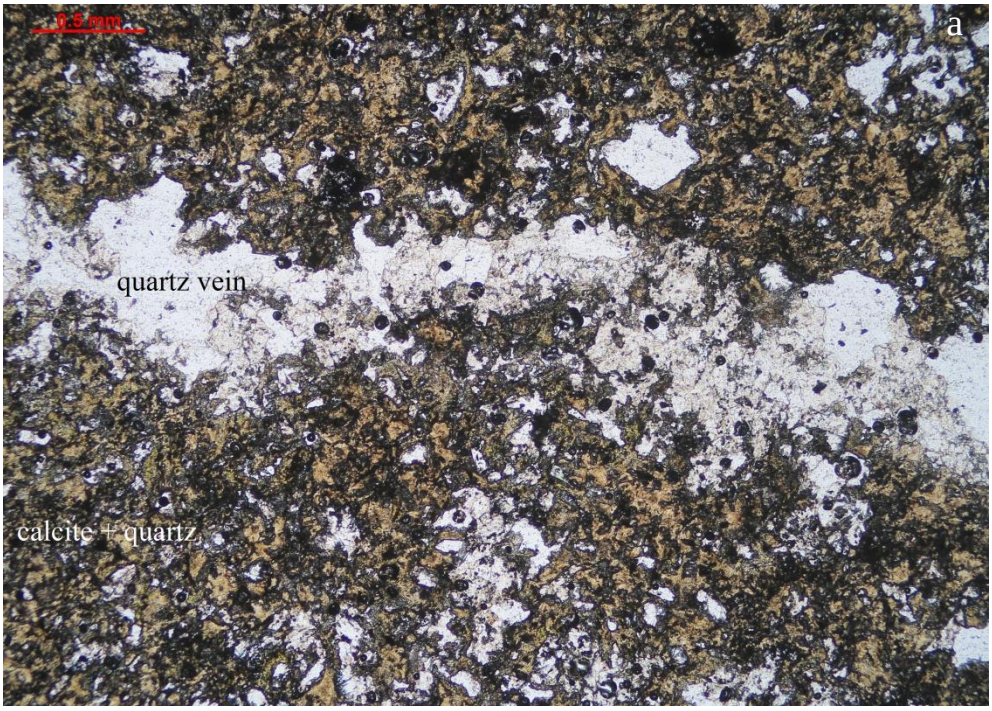

Figure 6: a) quartz vein running through finely crystalline altered matrix in sample 15. Plane polarised light.

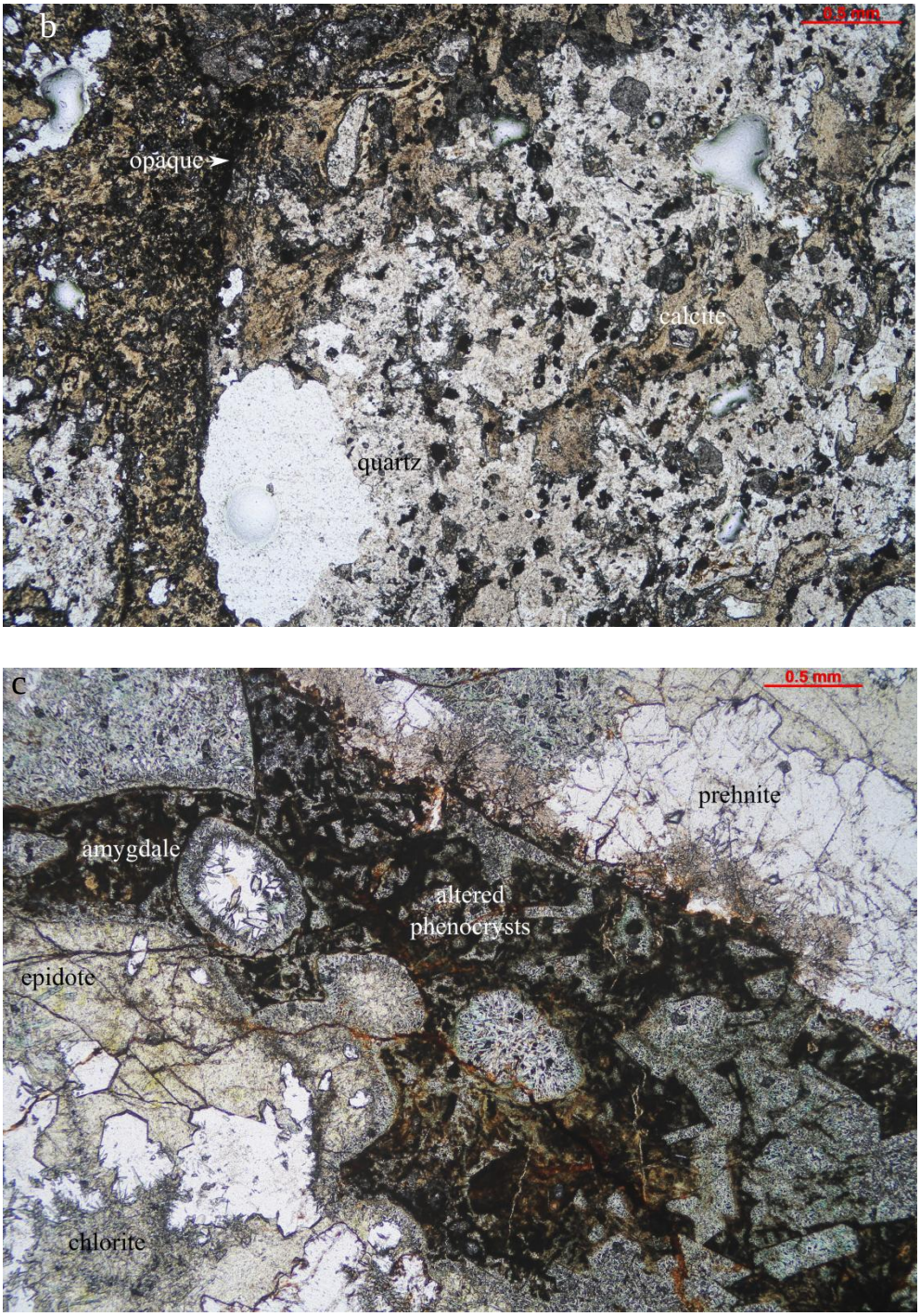

Figure 6 continued: b) transition between finely crystalline and coarser material in sample 15; c) altered remnant basalt clast with amygdales and pseudomorphed phenocrysts in coarse recrystallised matrix in sample 27. Plane polarised light.

2.2 Lapilli Tuff

The lapilli tuff is knobbly, grey-green and smooth in outcrop. It comprises framework basalt clasts of 2-50 cm, and individual crystals of plagioclase, quartz, and clinopyroxene, supported by a matrix with medium sand (0.25-0.5 mm) grainsize. While some of the larger framework clasts are blocks >64 mm, these large particles never comprise more than ~20% of the rock, and thus the lapilli tuff name is used. The framework clasts are mostly subangular, although many appear rounded in outcrop; I infer that this apparent roundness is due to weathering and smoothing by the sea.

Most of the basalt clasts are porphyritic, with phenocrysts of plagioclase and clinopyroxene. The majority of these clasts have vesicles infilled with quartz, chlorite, or prehnite to form amygdales. A few clasts lack these amygdales; some of these are aphyric, and many display flow banding (fig. 7a). One large block in the lapilli tuff at site 28, apparently ~4 m across, is coarser in texture than the other basalt clasts, has 2-7 mm phenocrysts of pyroxene and altered plagioclase, and is distinctly different chemically (sections 3.2.2, 4.2) and in thin section (fig. 8d).

There is lapilli tuff present both overlying and underlying pillow lava, with very little difference between the two. There is at least 8 m of lapilli tuff underlying the pillow lava, and at least 10 m overlying it. There is a greater range of framework clast sizes in the lapilli tuff above the pillow lava than in that below, with the former ranging from 2-50 cm while the latter ranges from 5-20 cm. However, the majority of framework clasts in the overlying lapilli tuff remain within the 5-20 cm range.

Where the pillow lava contacts the lapilli tuff (sites 11, 12, 14, 16, 18, 19, 21, 22, 23, 26), the contact is peperitic, gradational over several metres, with pillows becoming increasingly interspersed in the inter-pillow matrix until they occur as isolated clasts in the lapilli tuff. This is the case for pillow lava both overlying and underlying lapilli tuff, although the nature of the contact varies. In most places peperite blends with the lapilli tuff, as their clast textures, sizes, and compositions are very similar. At sites 21 and 22 (where lapilli tuff underlies pillow lava), the bottoms of pillows form a distinct line, though pillow fragments still occur beyond it (fig. 7b). At site 14 (where lapilli tuff overlies pillow lava), the transition includes a band of fine-grained material with only a few pillows within it.

The lapilli tuff displays beds that are weakly defined by variation in the amount and size of lapilli. The thickness of bedding varies from 0.5-2 m. Bedding is reverse graded in places, becoming framework-supported with smaller proportions of matrix and larger clasts towards the top of the layer (fig. 7c). Beds at site 19 are generally reverse graded, with sequences of 2-4 fine to medium beds followed by a bed with very large clasts (fig. 7d). At site 22 beds are not graded, but display sequences of 1 coarse sand-grained bed then 2-3 increasingly coarse-grained lapilli tuff beds. At site 10 the beds are graded in both normal and reverse directions. Elsewhere there are notable layers of dominantly sand-grained material containing few or no larger clasts. The larger clasts in these layers are generally 1-5 cm in size. Some beds have lower sections dominated by finer ash-grade matrix; in others this zone is missing and the contact with the bed below is more abrupt. At site 23 the bedding is marked by a band of significantly finer-grained material, with fine sand matrix and few lapilli of 2-20 mm. At site 11 the lapilli tuff has far less matrix; it is framework-supported, with 4-20 cm clasts. Between sites 24 and 27, the bedding is indistinct; in places within this region the lapilli tuff appears massive.

At site 3 the lapilli tuff contains 2-20 cm clasts which are very finely crystalline and paler coloured than the surrounding matrix; these have very irregular shapes. Some of the layers here with fewer large juvenile clasts include abundant round pebbles which closely resemble the amygdales in the pillow lava below.

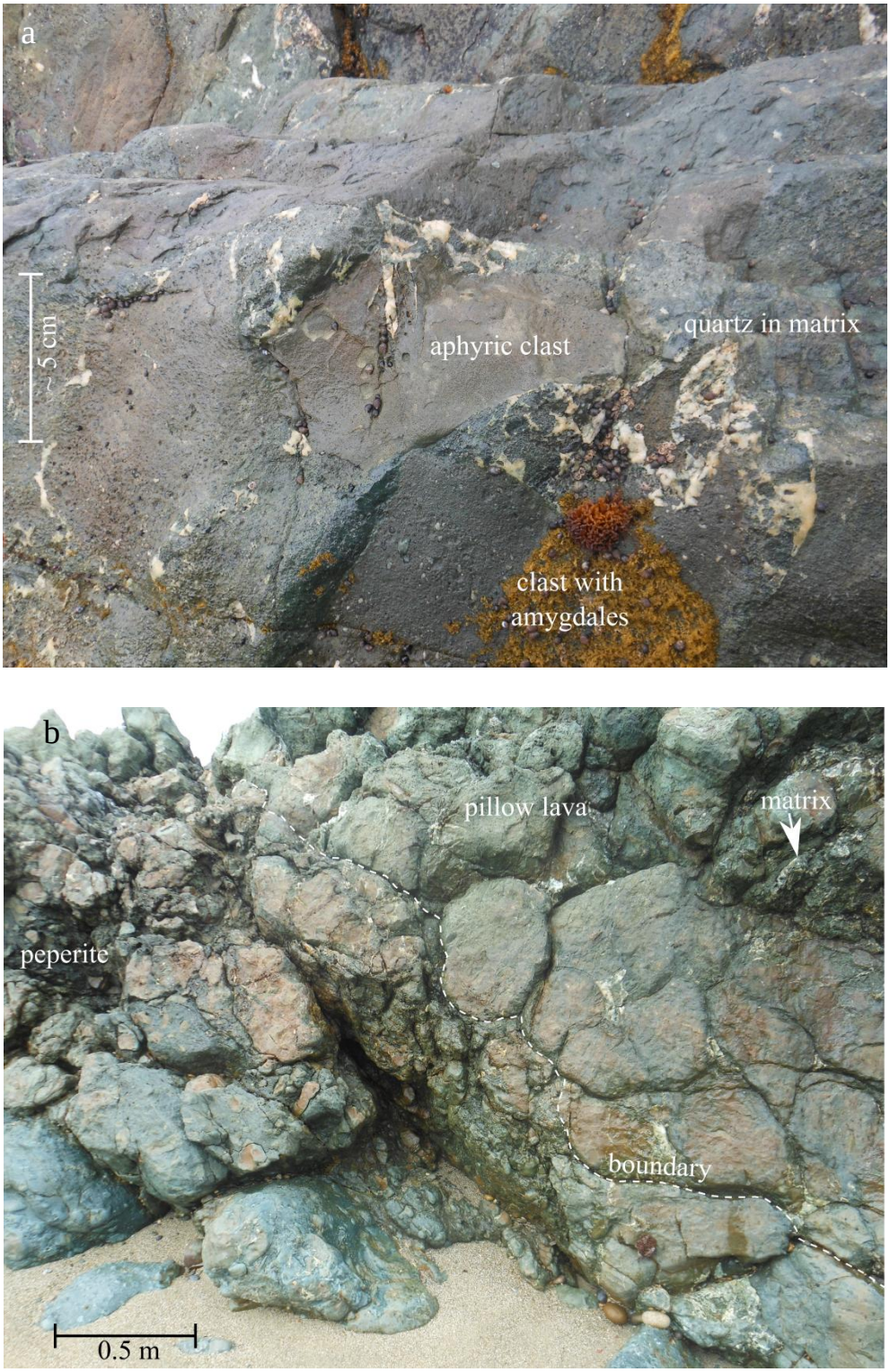

Figure 7: a) clasts in lapilli tuff at site 29, showing the distinction between aphyric clasts and those with abundant amygdales, with quartz cement in the matrix; b) pillow lava forming peperite in lapilli tuff below at site 21, boundary between pillow lava and peperite is unusually sharp, and pillow matrix is visible.

Figure 7 continued: c) reverse graded bedding in the lapilli tuff at site 21, showing the transition between matrix- and framework-supported; d) reverse graded beds in lapilli tuff at site 19, with black arrows showing the direction of grading.

2.2.1 Petrography

Some thin sections have been made of the matrix of the lapilli tuff, while others are of the basalt lapilli within it.

The matrix encompasses subangular crystal clasts of albite, K-feldspar, quartz and clinopyroxene up to 1 mm, with minor titanite and apatite. Many clasts are altered to chlorite or quartz, and some iron-staining is present (fig. 8a). Basalt clasts containing plagioclase laths and/or amygdales are also common in the matrix, though many are more highly altered than the surrounding crystal clasts. Some amygdales in basalt clasts are similar to those visible in the larger lapilli, but most are much smaller and filled solely with chlorite (fig. 8b). Vesicles at the edges of these small clasts are filled with the small crystals of the matrix. At thin section scale some layers defined by different clast sizes are visible. Some chalcopyrite crystals are visible both within larger clasts and in the matrix.

Most larger basalt clasts resemble the basalt of pillow lava in outcrop and thin section. They comprise a groundmass of albite laths in random orientation and up to 0.4 mm, with smaller, euhedral or interstitial clinopyroxene crystals between them (fig. 8c). Minor titanite is also present in the groundmass. Irregularly shaped patches of chlorite are common, ranging from 0.05 to 0.3 mm, which are shown to display radially arranged acicular crystals in cross-polarised light. Some include crystals of spinel in their centres (fig. 8c). Phenocrysts include clinopyroxene (up to 1 mm) and albite (up to 2 mm) with some pumpellyite alteration. The albite commonly and the clinopyroxene rarely occur in glomerocrysts. Vesicles are less common than in the pillow lavas, and some of them are not infilled. Those that are infilled commonly comprise a pumpellyite or chlorite rim with quartz or prehnite centres. As in sample 21a, many amygdales are surrounded by a region of more finely crystalline, more strongly altered groundmass.

A block from site 28 was noted in outcrop to be distinct from the other clasts in lapilli tuff, and this distinction holds true in thin section. The block is non-vesicular, and comprises finer groundmass with larger, more abundant phenocrysts than the other samples. The groundmass comprises very small laths of albite, with larger clinopyroxenes, interstitial chlorite, and much more abundant titanite than seen elsewhere. Many of these small albite laths show preferred orientation parallel to the edges of the phenocrysts. Phenocrysts are up to 3 mm, and consist of cracked, frequently twinned clinopyroxene, and highly altered albite. Some clinopyroxene phenocrysts have inclusions filled with

groundmass (fig. 8d). The albite displays patchy alteration of prehnite, pumpellyite, chlorite and quartz. The pumpellyite occurs in patches like those in other samples, but larger and more pervasive. Elsewhere the phenocrysts are entirely or almost entirely altered, with irregular patches of prehnite and quartz surrounded by chlorite which pseudomorphs the original crystals.

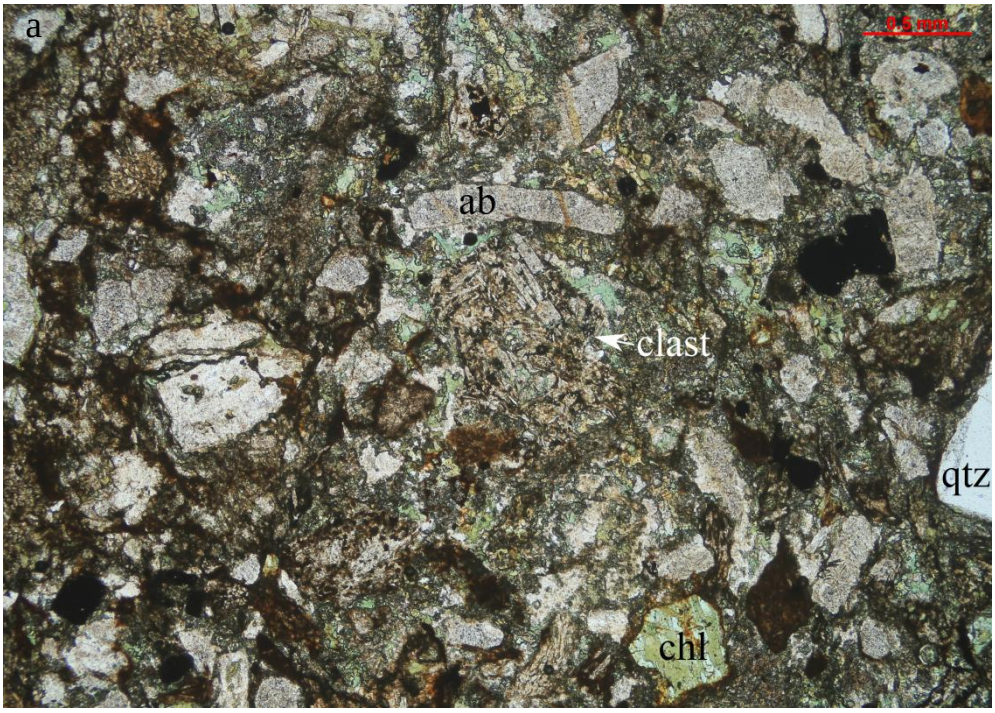

Figure 8: a) a general view of the matrix of the lapilli tuff in sample 2c, with a clast bearing albite laths in the centre of the image. Plane polarised light.

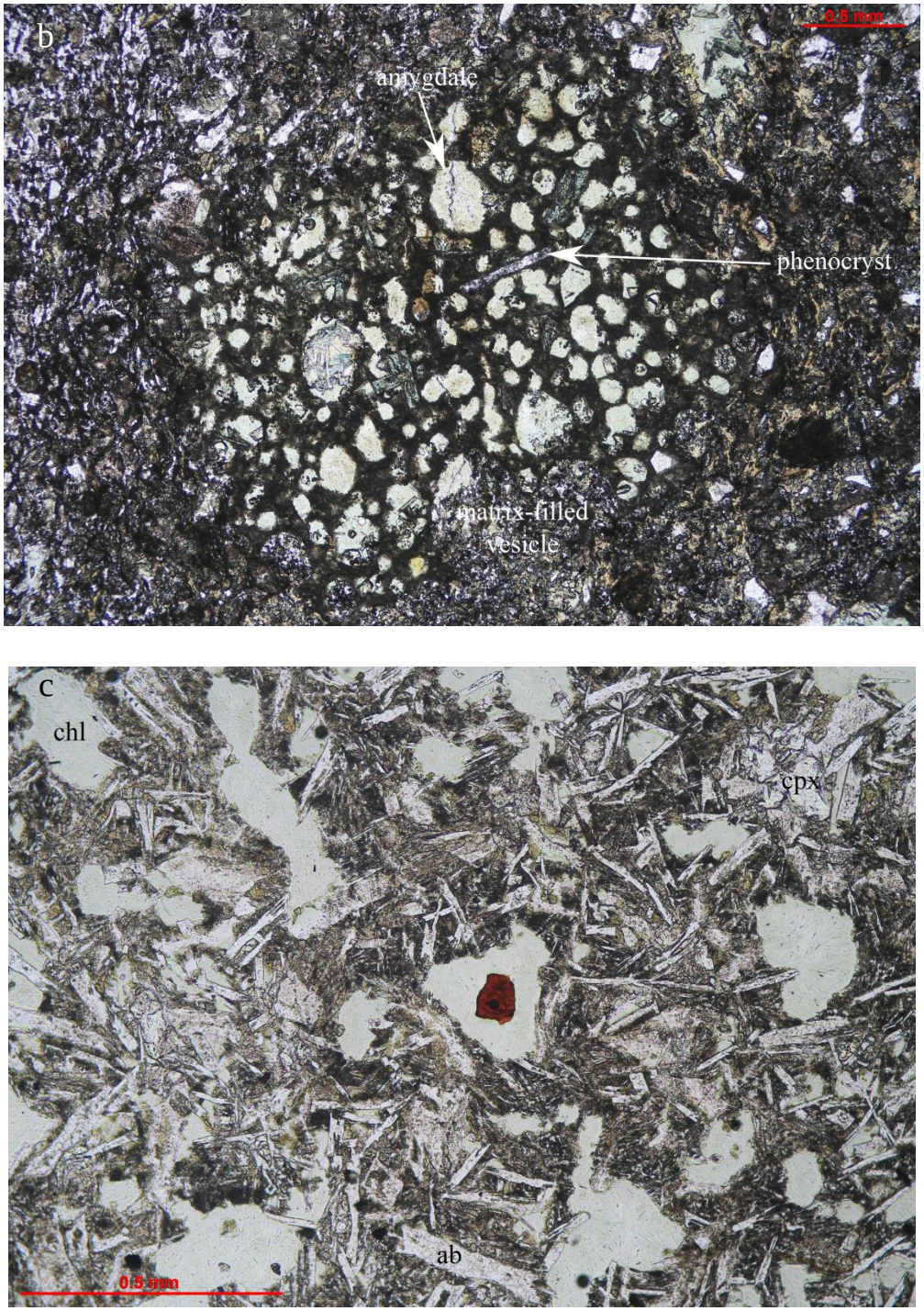

Figure 8 continued: b) a clast within the matrix of the lapilli tuff in sample 17 with chlorite-filled amygdales, note how vesicles at the edges of the clast are filled with matrix; c) a basalt clast within the lapilli tuff (sample 29b), showing groundmass composed predominantly of albite and chlorite, and spinel within chlorite at the centre. Plane polarised light.

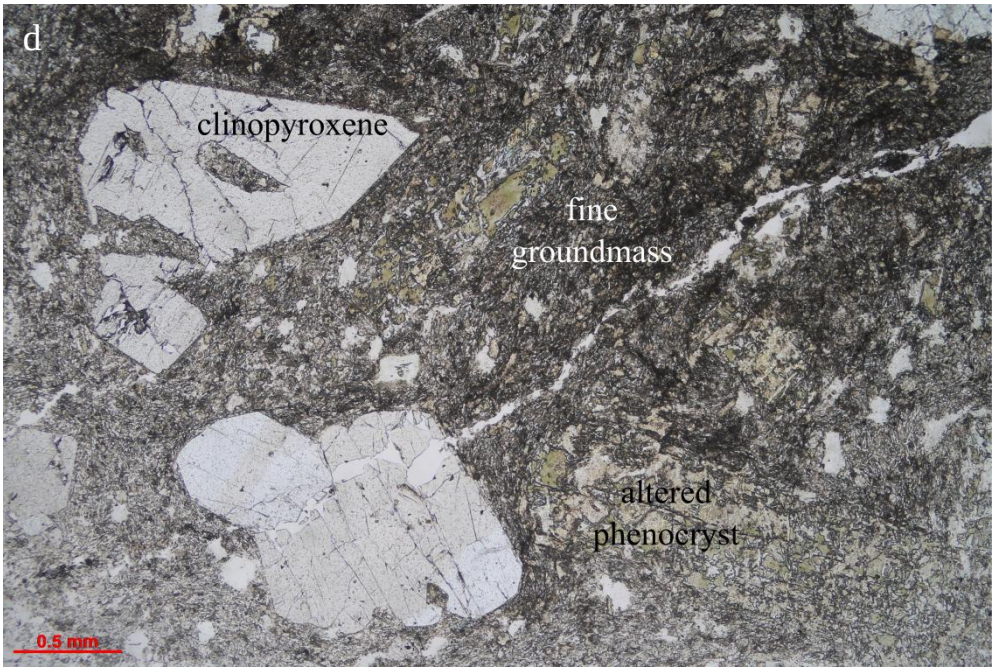

Figure 8 continued: d) sample 28, showing its unusual features: large clinopyroxene phenocrysts with groundmass inclusions, particularly fine groundmass, and highly altered albite phenocrysts. Plane polarised light.

2.3 Tuff

Adjacent to the lapilli tuff is tuff without any larger clasts; its grainsize ranges from silt (3.9-62 μm) to medium sand (0.25-0.5 mm), with variation over the region in which it appears. At site 1 it is very fine-grained, pale green and very smooth in texture, with a 2-3 cm red-brown weathering rind. At sites 2 and 3 it has very fine sand (62-125 μm) grainsize. At site 4 the grains are medium sand-sized. In places throughout the tuff small (1-5 mm) distinct crystals are visible. In places there are scattered euhedral pyrite crystals; these are abundant in localised areas (fig. 9a), and diffuse elsewhere.

The tuff lies laterally to the NW of the lapilli tuff, with the exception of one outcrop at site 25. Between sites 8, 9, and 10, there is an area where the rock is a medium-grained tuff, and lapilli tuff occurs as coarse channel fill (fig. 9b). The channels grow thinner westwards, towards the area where tuff predominates. Channels are approximately 0.2-1 m deep and 1-6 m wide. They are more deeply eroded into the cliff face than the host tuff. The host tuff has weak bedding, and upper surfaces of the channel fill deposits are parallel to it. The channel-fill lapilli tuff does not exhibit any internal structure.

There is some lapilli tuff directly underlying tuff, but the contact between the two is nowhere directly observed. At site 2 there appears to be lapilli tuff vertically underlying tuff, but the contact is low to the ground and buried by sand. Here both units dip at 097/22S, so it is reasonable to infer that the contact also has this orientation. At site 3, on the E side of the adjacent headland, the contact is also not directly observable, but visible high on the cliff, indicating that it is also folded.

At sites 8 and 9, within the channel zone, there are peperitic contacts between pillow lava and tuff (fig. 9c). Pillows bulge upwards into the tuff, with some broken off and dispersed into it, resulting in a lapilli tuff texture over the region in which the peperite occurs; for 1-2 m above the pillow lava. Overlying this region the weak bedding of the tuff is visible again.

At site 2 laminations were observed, and cross-laminations were visible, but only in a detached boulder so directionality was not distinguishable. At site 5 cross-laminations are present in outcrop and indicate that current flowed westwards. There is also subtle lensing of some beds within the tuff discernible at site 5. At site 7 the tuff displays layers 4-40 cm thick of varying grainsize. These layers are often pitted where crystals have been weathered out, and they contain clasts up to 2 cm.

At site 2 the tuff includes bands of pale elongate blebs with irregular shapes. These are inferred to be bioturbation features. At sites 2 and 3 it has irregular clasts of pale, very fine-grained material. At site 5 the tuff includes a large amount of these 1-4 cm clasts, but this lapilli tuff texture extends only over a small area of ~3 m.

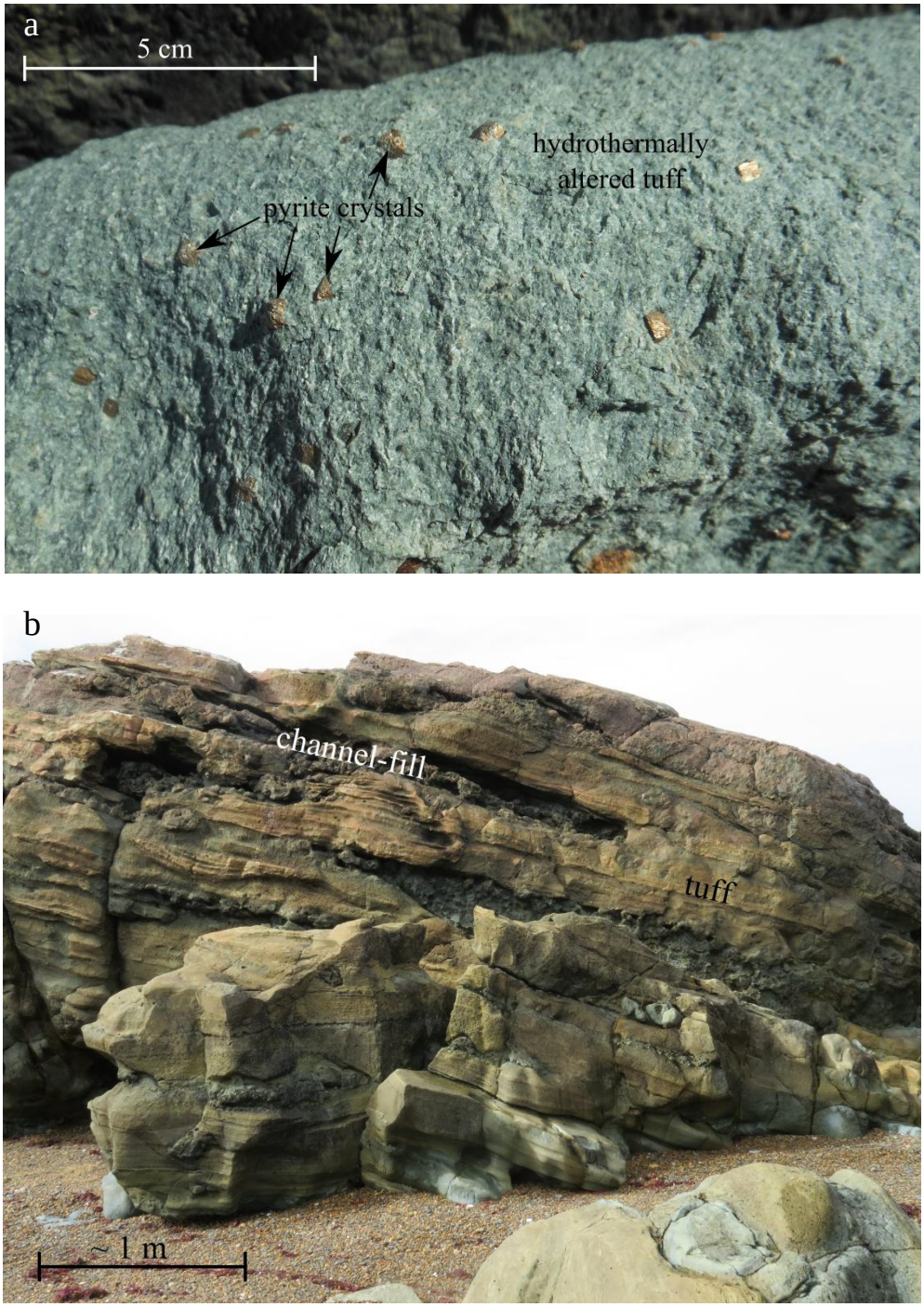

Figure 9: a) euhedral pyrite crystals in tuff at site 4; b) lapilli tuff filling channels within tuff.

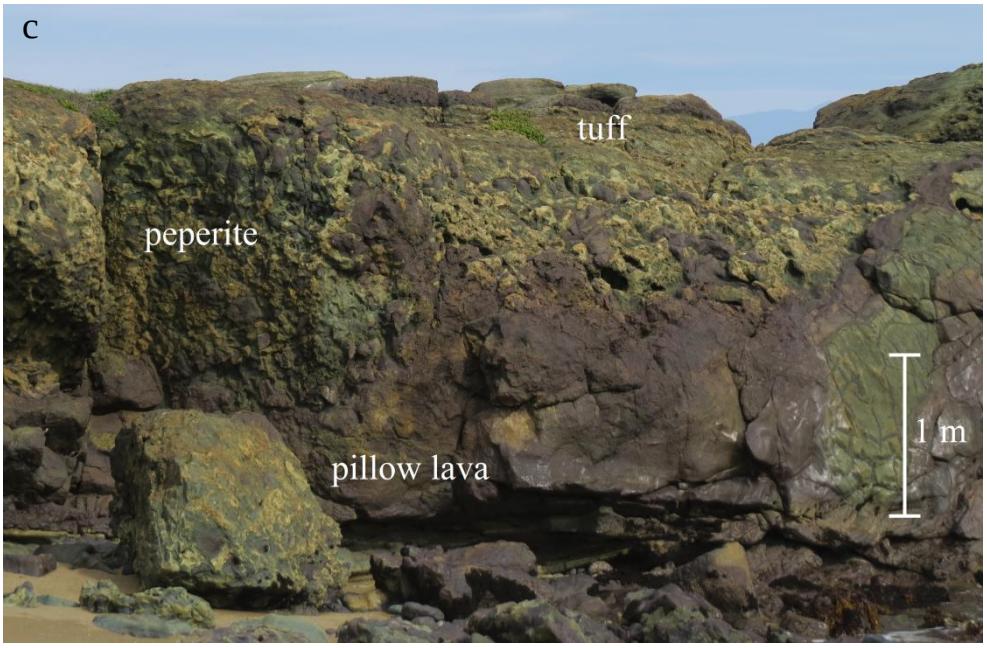

Figure 9 continued: c) peperitic contact between pillow lava below and tuff above at site 8. Photographs b and c by Professor James D.L. White, used by permission.

2.3.1 Petrography

The tuff is quite variable across the area in which it occurs; in some places its clasts resemble smaller versions of lapilli in the lapilli tuff, while elsewhere it is too fine-grained for such distinctions to be made. The degree of alteration is also variable.

Clasts in the coarser tuff range up to 2 mm; the lower size limit is not distinguishable because alteration makes the smallest grains indiscernible. Clasts are frequently irregular in shape and difficult to distinguish from the material surrounding them; this is inferred to be pseudomatrix, composed of clasts deformed (Dickinson, 1970) to the point that they are unrecognisable (fig. 10a). Many clasts comprise albite or quartz; a few are of K-feldspar. These are single crystals with rounded or a few with broken edges, many with dusty alteration. Also common are once-glassy clasts with abundant small (0.1-0.2 mm) amygdales, commonly infilled with chlorite (fig. 10b). Other clasts contain distinct laths of albite, some with phenocrysts (fig. 10a, b). One clast has a vein of apatite running through it. The smaller clasts include crystals of albite, quartz, clinopyroxene, K-feldspar, titanite, and apatite.

Pyrite occurs in small quantities throughout sample 4 (a sample from the region of the tuff where large euhedral pyrite crystals were observed in outcrop), with one larger (1 mm) cluster of pyrite crystals within the slide, and one large (1 mm) pyrite crystal with inclusions of prehnite. The cluster of pyrite is surrounded by a mantle of prehnite. Some irregular, wispy regions of chlorite also occur, commonly surrounded by small crystals of prehnite.

Sample 5 includes glomerocrysts of albite and clinopyroxene, 0.3-1 mm across. Some glomerocrysts comprise a mixture of albite and clinopyroxene, with intergrowth textures preserved.

There are rare grains of polycrystalline quartz in sample 30. Many of the basaltic clasts contain chlorite replacing albite laths. Some clasts are heavily altered to clay minerals, and may have been glassy before this alteration took place. Sample 30 also contains an unusually large clast (>4 mm) with abundant chlorite-filled amygdales 0.02-0.2 mm in size and multiple 0.2-1 mm albite phenocrysts.

The apparently finer-grained tuff is significantly more altered, and probably consists largely of pseudomatrix; regions of varying colour and slightly different groundmass may approximately designate the original clasts, which would thus have been 1-2 mm in size, implying an initial deposit of medium-very coarse ash. Clasts now consist mainly of albite, with some clinopyroxene, quartz, K-feldspar, apatite and titanite. Chalcopyrite and pyrite occur in scatters of very small crystals. Crystals within this tuff are very small, 0.2 mm or less, and heavily altered. A sinuous quartz vein runs through one sample, varying from 0.2-0.6 mm in width and including fine and coarse polycrystalline quartz with undulose extinction, with fine chlorite at the edges in many places (fig. 10c).

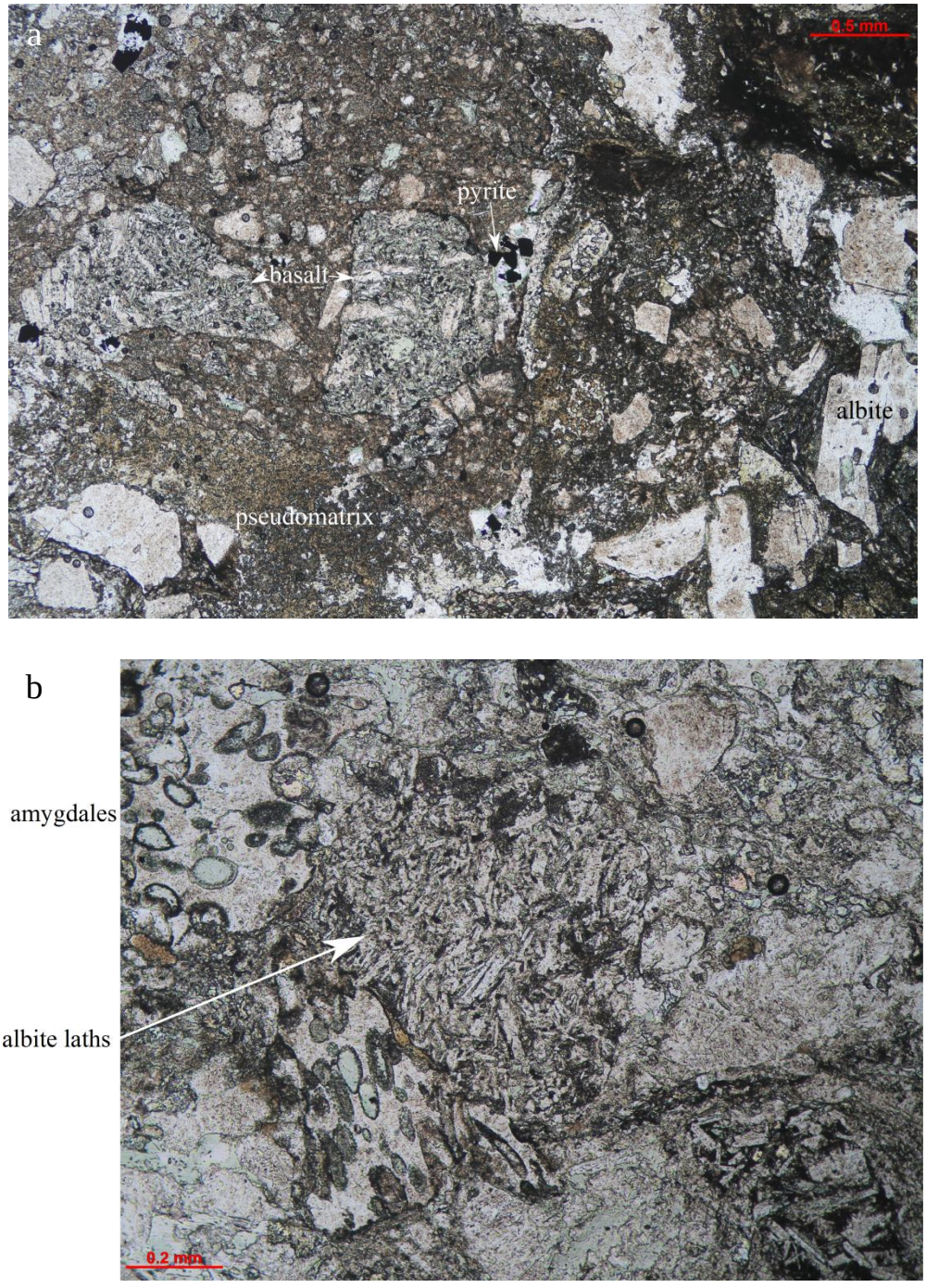

Figure 10: a) a general view of the tuff in sample 30, showing several altered basalt clasts, and the way clasts blend into one another to form pseudomatrix; b) examples of clasts within the tuff in sample 4, including those bearing chlorite-filled amygdales, and those with albite laths. Plane polarised light.

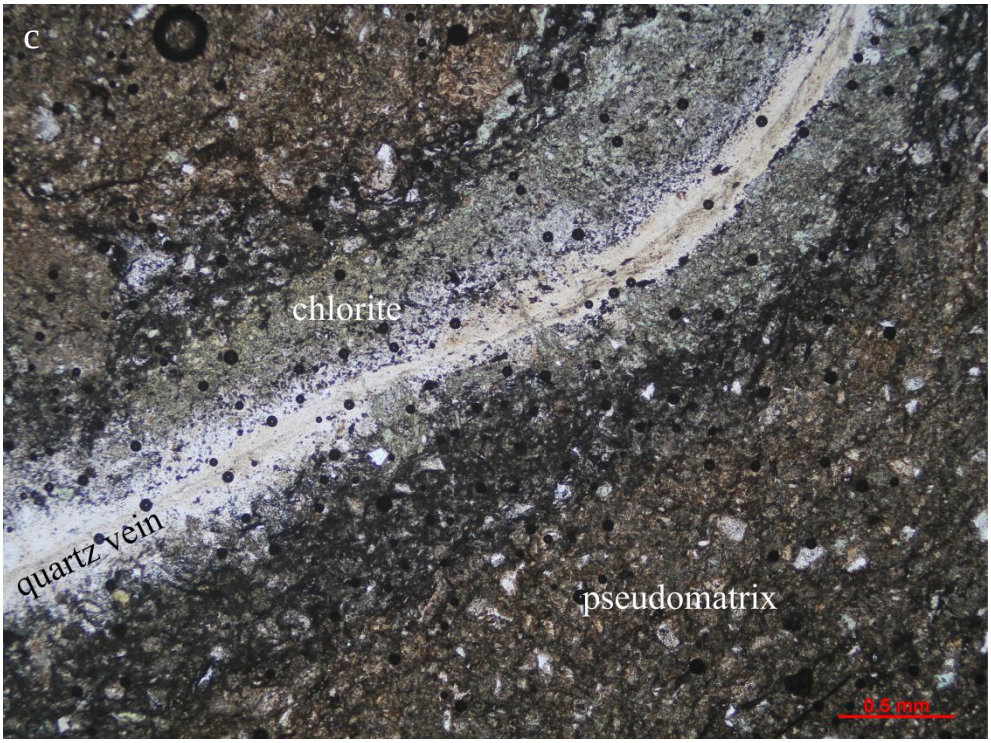

Figure 10 continued: c) quartz vein through the finer-grained tuff of sample 2a. Plane polarised light.

2.4 Argillite

The argillite forms large cliffs with distinct bedding. It is pale green on fresh surfaces, weathered to brown and grey in many places, and smooth to the touch. It is very fine grained (silt to very fine sand (3.9-125 μm)), and fractures in an irregular, almost conchoidal manner. Well-formed pyrite and chalcopyrite crystals are scattered throughout; these are usually <1 mm, though at site 30 they range up to 4 mm. In several places these crystals are concentrated in veins.

The argillite has a consistent contact with the tuff below, which commonly appears as a sharp, planar crack (fig. 11a). In places the crack is incised, and at site 7 there is a 20 cm thick zone of pale, highly weathered rock visible between the argillite and the tuff. In several places (at sites 5, 7, 8, and 25) there is a more gradual transition with interlayered argillite and tuff; the bands of argillite are 1-20 cm thick, while the tuff layers grow thicker further down the section (fig. 11b). The tuff layers are also internally banded in these areas, with this banding more pronounced adjacent to the argillite layers. The contact is generally shallowly dipping, with varying orientations from 116/28N to

120/08N in the W, to 155/05S at the eastern end of the section. There is also a layer of tuff overlying the argillite (marked T2 in Plate 1), which appears similar to the tuff observed elsewhere, though slightly coarser-grained.

The argillite has prominent bedding with thickness of 0.4-1 m. It is consistently laminated, and locally cross-laminated. Cross-laminations are trough-shaped, and indicate that way-up is upwards and flow direction is northwards (fig. 11c). At site 6 Bouma T_{b-e} sequences are visible (fig. 11d), suggesting that this unit was deposited as a series of turbidity currents. These are entirely fine-grained, lacking the massive coarse-grained T_a layer of the idealised sequence, and displaying the top fine-grained T_e layer. Elsewhere, only Bouma T_{d-e} divisions are visible.

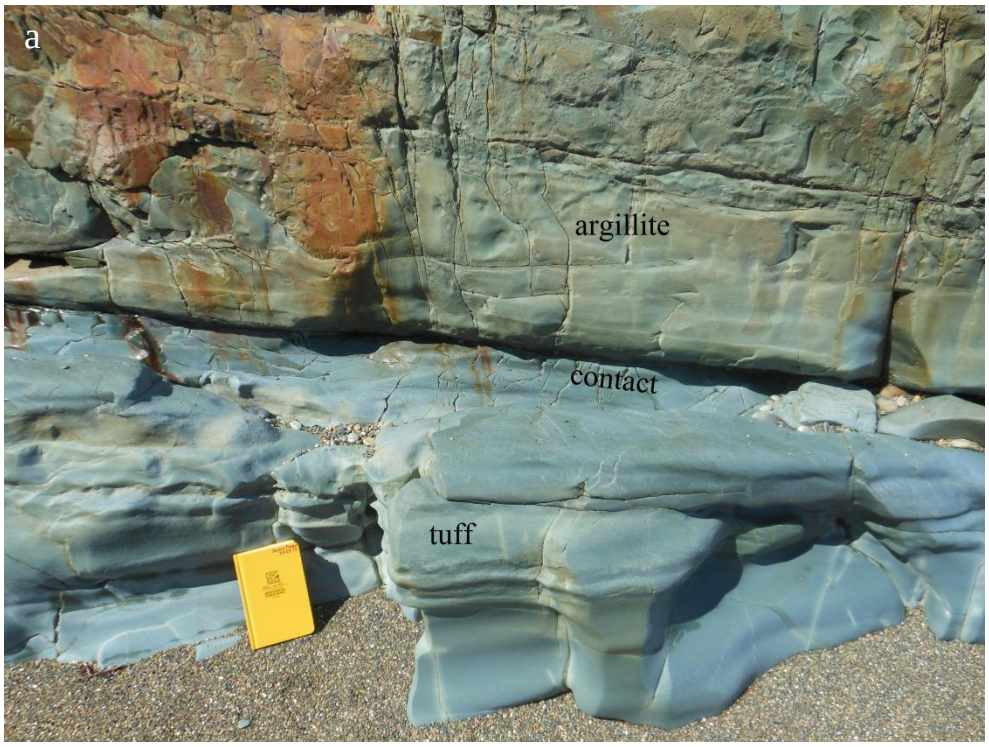

Figure 11: a) incised contact between argillite and the underlying tuff at site 6. Notebook for scale is 20 cm lengthways.

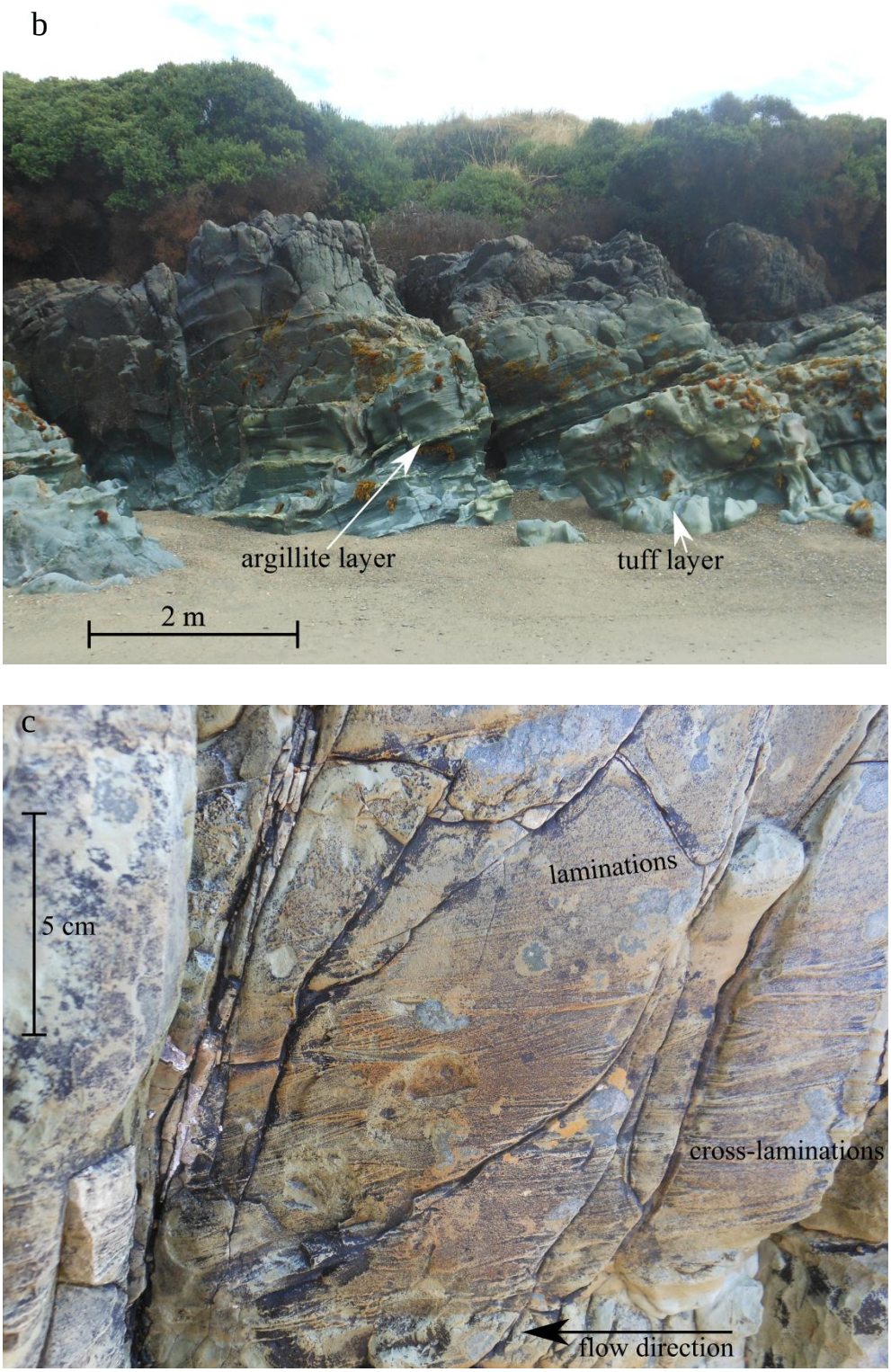

Figure 11 continued: b) argillite interbedded with the underlying tuff at site 25; c) cross-laminations in argillite at site 4.

Figure 11 continued: d) argillite showing Bouma sequence at site 6. Notebook for scale is 20 cm lengthways.

2.4.1 Petrography

The argillite is highly altered in thin section (sample 1), with crystal clasts in a calcite cement with abundant clay alteration. The dominant clasts are albite and clinopyroxene, and they are 0.01-0.3 mm and rounded to subangular in shape. K-feldspar, titanite and apatite are present in minor quantities. Pyrite and chalcopyrite are abundant, larger than the clasts (0.1-0.7 mm), with rounded to irregular shapes.

Faint layering is distinguishable at this scale, with layers of varying clast size and ratio of clasts to cement (fig. 12a). Within the slide are some round regions 3-4 mm in size with much finer grains, composed mostly of the calcite cement (fig. 12b); these are concretions. Some of the concretions have irregular shapes composed of larger calcite crystals within them, while others have round centres that more closely resemble the surrounding clastic areas.

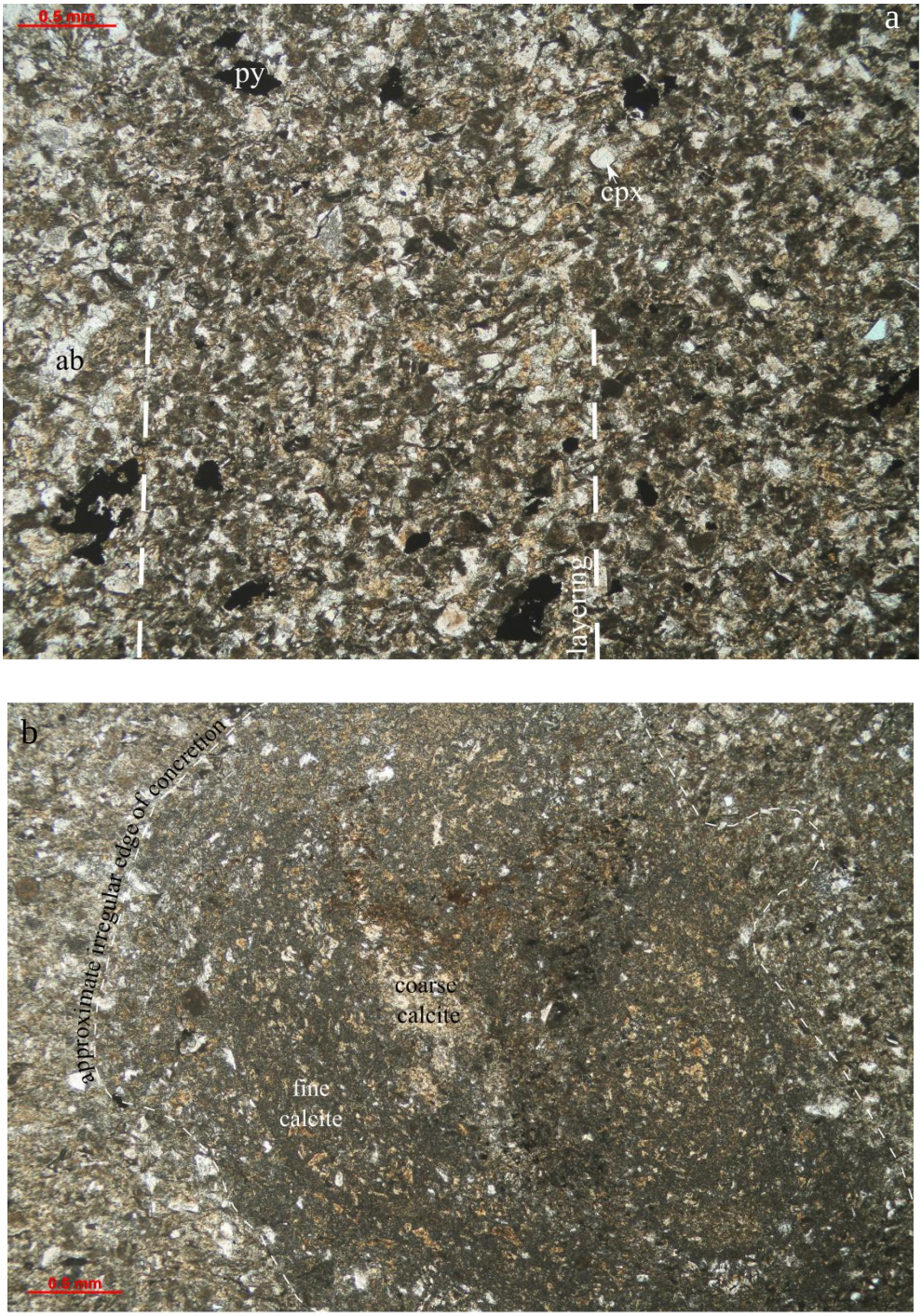

Figure 12: a) layering in argillite (dashed lines to emphasize layers); b) calcite concretion with irregular edges.

2.5 Dikes

A number of dikes cut through the sequence; they are 0.3-1 m thick. Most dikes are porphyritic with phenocrysts of pyroxene and plagioclase, though some are aphyric. Most have chilled margins (fig. 13a), and several display flow banding. Some have margins which are undulating on a decimetre scale. Some have multiple generations of chilled margins, and some have bands of varying vesicularity. Dikes vary in colour, from the same shade as the surrounding rock to very dark grey.

They have orientations of 149/58W, ~126/74SW, 140/84W, 150/90, 137/85W, 113/58S, 162/39N and 128/59S.

Where dikes appear in lapilli tuff, several of them display apophyses into the surrounding lapilli tuff (fig. 13b), and in places have engulfed domains or clasts of the lapilli tuff. In a few places there appear to be dikes running parallel and very close together, with a narrow band of lapilli tuff between them; at site 29 this band has more angular clasts than the surrounding lapilli tuff, and varies in thickness, mostly ~7 cm but as narrow as 0.5 cm, while at site 28 the intervening lapilli tuff forms a lens, and aligned with the lens the two dikes are directly in contact with chilled margins between them (fig. 13c).

Dikes are less common in pillow lava than in the lapilli tuff. One dike at site 26 appears to have an apophysis into the inter-pillow matrix. Some dikes in tuff are more coarsely crystalline (0.5-2 mm, with phenocrysts up to 10 mm).

At site 12 there is a thin dike (~30 cm) which is dark red and sinuous. At site 29 is a pair of cross-cutting dikes with orientations of 045/82W and 028/26W. At site 23 is a pair of cross-cutting dikes with undulating margins, one of which has a chilled margin against the other. One dike at site 19 comes to an end in the lapilli tuff with a bulbous, blobby form, with clasts that resemble the dike surrounding it in the lapilli tuff. At site 25 one dike has an offset segment (fig. 13d). Another narrows to a tip and ends.

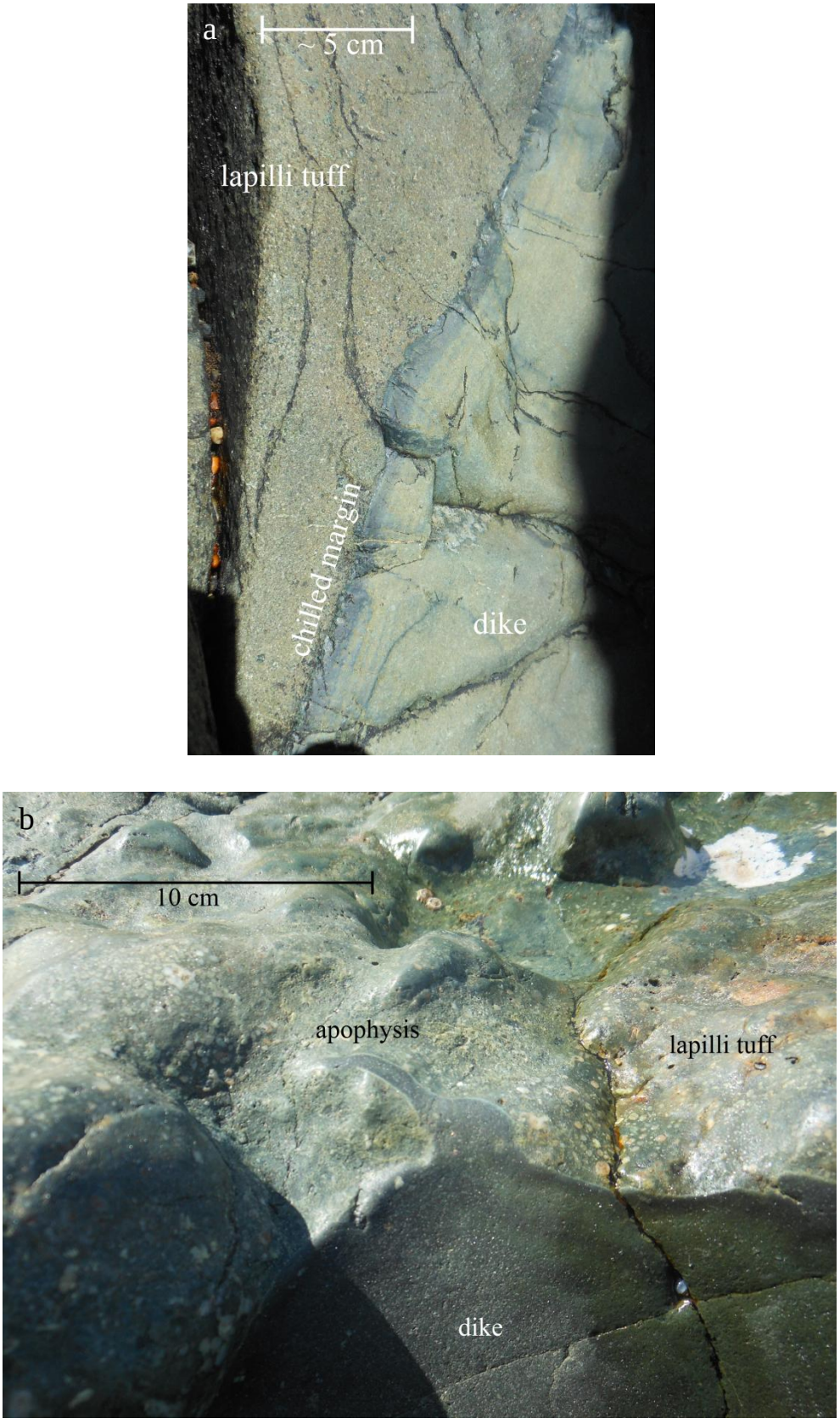

Figure 13: a) chilled margin of a dike within the lapilli tuff at site 28; b) apophysis of a dike into the surrounding lapilli tuff at site 19.

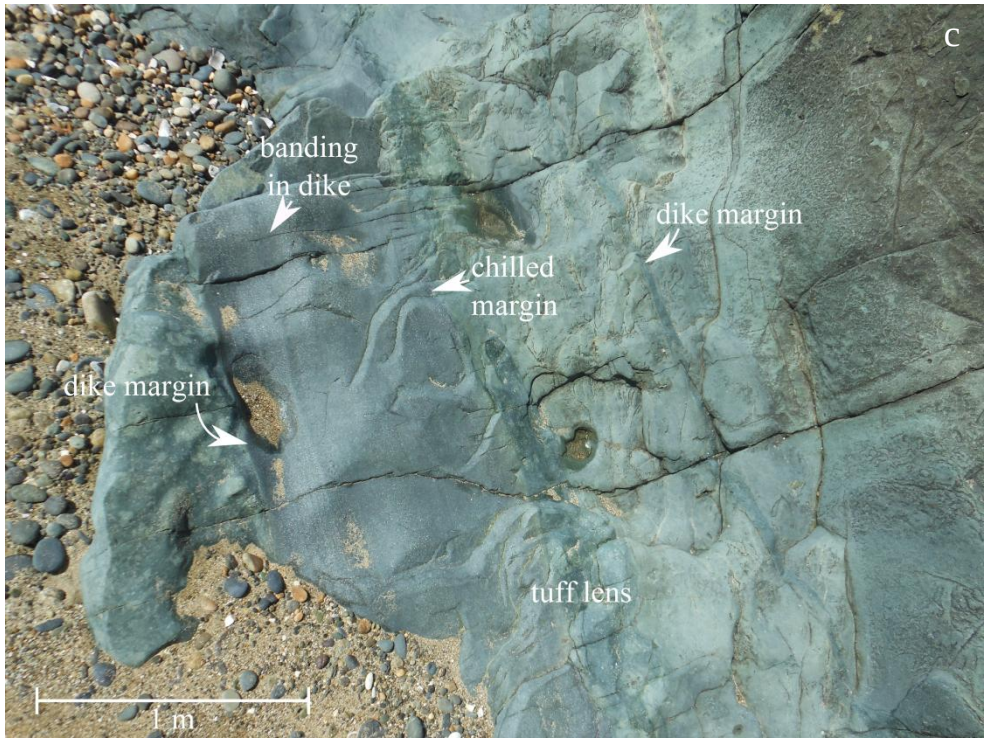

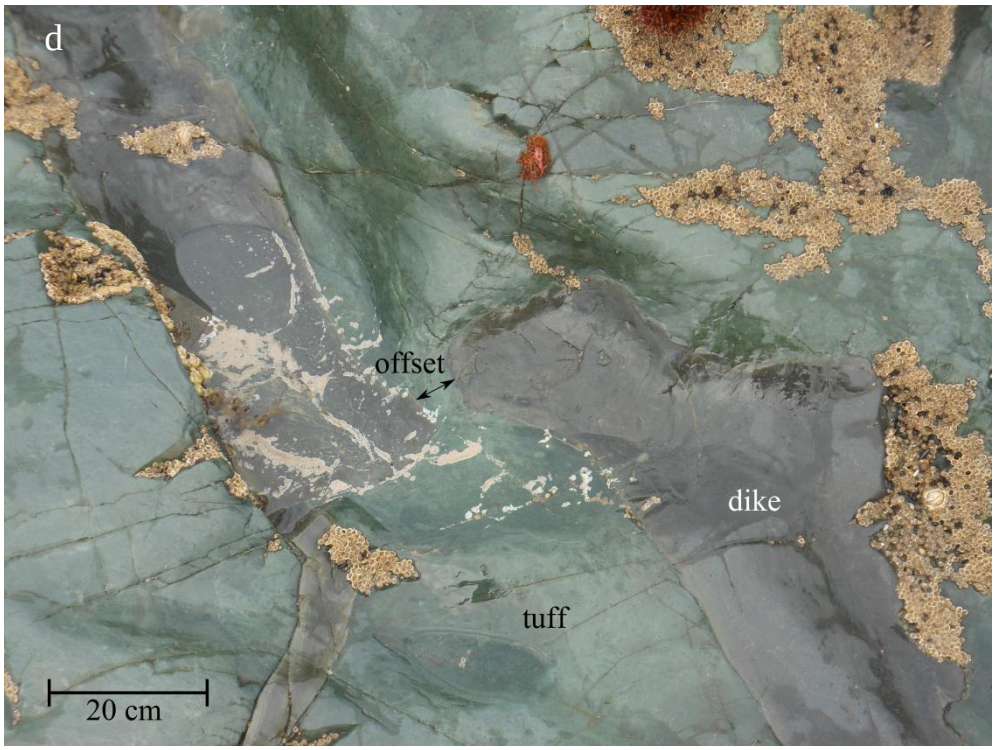

Figure 13 continued: c) a lapilli tuff lens between two closely spaced dikes at site 28; d) dike with offset in tuff at site 25.

2.5.1 Petrography

Despite their varying degrees of alteration as observed in outcrop, the dikes are remarkably consistent in thin section across the field area. They comprise a groundmass dominated by albite laths up to 0.5 mm in length, with abundant irregularly-shaped patches of chlorite and many smaller (0.01-0.03 mm) crystals of clinopyroxene. Many of these clinopyroxene crystals display rounded shapes, particularly in sample 21b (fig. 14a). Minor groundmass phases include titanite, chalcopyrite, and pumpellyite. Phenocrysts of albite and clinopyroxene are far more common than in the pillow lavas, and these minerals sometimes occur in glomerocrysts up to 2 mm across. Some show intergrowths of plagioclase and clinopyroxene. Many albite phenocrysts show abundant pumpellyite alteration as small irregularly-shaped patches within them. Some clinopyroxene phenocrysts display simple twinning, while a few albite crystals are zoned.

Amygdales are 0.2-0.4 mm across, significantly smaller than in the pillow lavas. They are commonly filled with prehnite, pumpellyite and quartz, and many have rims comprising radiating bundles of pumpellyite and larger crystalline quartz centres. These commonly include acicular pumpellyite crystals extending into the quartz. A few of them also contain crystals of chalcopyrite. In a few amygdales the centre is of prehnite rather than quartz (fig. 14b), but more commonly where prehnite fills a vesicle it does so entirely.

In sample 29a, thin (0.01-0.1 mm) quartz veins run across the slide, subparallel and anastomosing (fig. 14c).

The albite crystals in the groundmass of sample 21b are shorter but of a more consistent width than those in 29a, and display a more pervasive dusty alteration. Opaques are more common in the groundmass, and comprise iron oxide and iron-titanium oxide. Many of the amygdales are irregular in shape, constrained by the crystals around them. A region of the slide displays widespread diffuse iron-staining.

Sample 2b displays considerably more alteration than the other dike samples, with both groundmass and phenocryst albite showing dusty alteration. Chlorites are larger, with some the same size as phenocrysts, and many are euhedral in shape suggesting they are replacing the absent clinopyroxene phenocrysts. This sample also includes a few phenocrysts of pyrite, with inclusions of prehnite.

Figure 14: a) groundmass in sample 21b, showing albite laths, rounded clinopyroxene crystals, chlorite and minor titanite; b) amygdale in sample 21b with pumpellyite rim and centre of radial acicular prehnite. Plane polarised light.

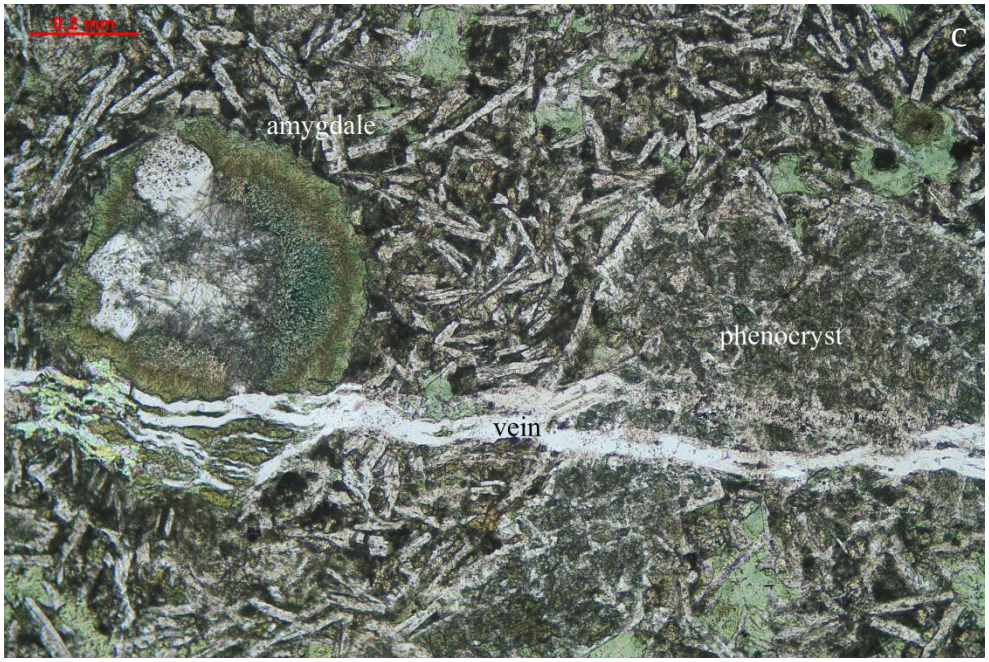

Figure 14 continued: c) vein in sample 29a, anastomosing and running through an amygdale with pumpellyite rim and quartz centre, and an albite phenocryst with pumpellyite alteration. Plane polarised light.

3. Major Element Geochemistry

3.1 Analytical methods

Energy-Dispersive x-ray Spectroscopy (EDS) analyses were conducted on thin sections of all rocks sampled to determine the major element compositions of their constituent minerals. This was conducted using the Zeiss Sigma VP variable-pressure field-emission scanning electron microscope of the Otago Centre for Electron Microscopy. The thin sections were polished and carbon coated. Point analyses, linescans, and element mapping were conducted; linescans provide a measure of zonation within minerals, and maps provide a picture of the distribution of elements across mapped areas of the slides.

3.2 Results

The EDS results generally support the mineralogy identified in thin section, and add major-element compositional information. Scanning Electron Microscope images collected at the same time reveal a few textural details notable at a finer scale than can be observed under a petrographic microscope. All data are presented in Appendix B.

3.2.1 Pillow lava

The EDS-determined compositions are consistent with the mineralogy observed in thin section. Pillow lavas have a groundmass of albite and clinopyroxene with chlorite and pumpellyite alteration, and amygdales comprising quartz, prehnite, pumpellyite, and chlorite. In sample 21a albite is also present in some vesicles, and clinopyroxene (diopside and hedenbergite) is present as phenocrysts. Here the groundmass clinopyroxene has $Wo_{43-48}En_{18-39}Fs_{13-28}$ and the phenocryst clinopyroxene $Wo_{47-48}En_{36-37}Fs_{15-16}$, and albite is Ab_{86-93} in the groundmass and Ab_{86-94} in amygdales. Mg# (Mg/Mg+Fe × 100) of clinopyroxene averages 76. Sample 20 has groundmass albite Ab_{92-96}, and clinopyroxene (augite and diopside) $Wo_{41-47}En_{28-41}Fs_{17-30}$, with Mg# averaging 73.

The regions of varying grainsize within sample 20 show minor systematic compositional variation (up to 4 wt% difference in major elements in area scans of each

region), with the finer-grained regions slightly more mafic. It is revealed that the circular darker regions surrounding segregation vesicles in sample 21a contain crystals of augite and albite.

The EDS analysis also reveals that in addition to calcite, quartz, and titanite, inter-pillow matrix sample 15 contains K-feldspar (Or_{97-98}) and iron oxide. The latter appears in small regions, but within these areas it is disseminated between and within the other minerals (fig. 15). Some parts of the slide appear to contain shapes resembling the outlines of crystals and vesicles, suggesting that perhaps this sample also bears the traces of clasts rendered mostly unrecognisable by alteration.

Sample 27 contains quartz, prehnite, epidote, chlorite, and albite. The few remnant clasts within this inter-pillow matrix are altered almost entirely to clay minerals, though scattered albite crystals remain. Some of the large prehnite crystals in the slide are zoned, with increase in Fe and corresponding decrease in Mg content towards the edges.

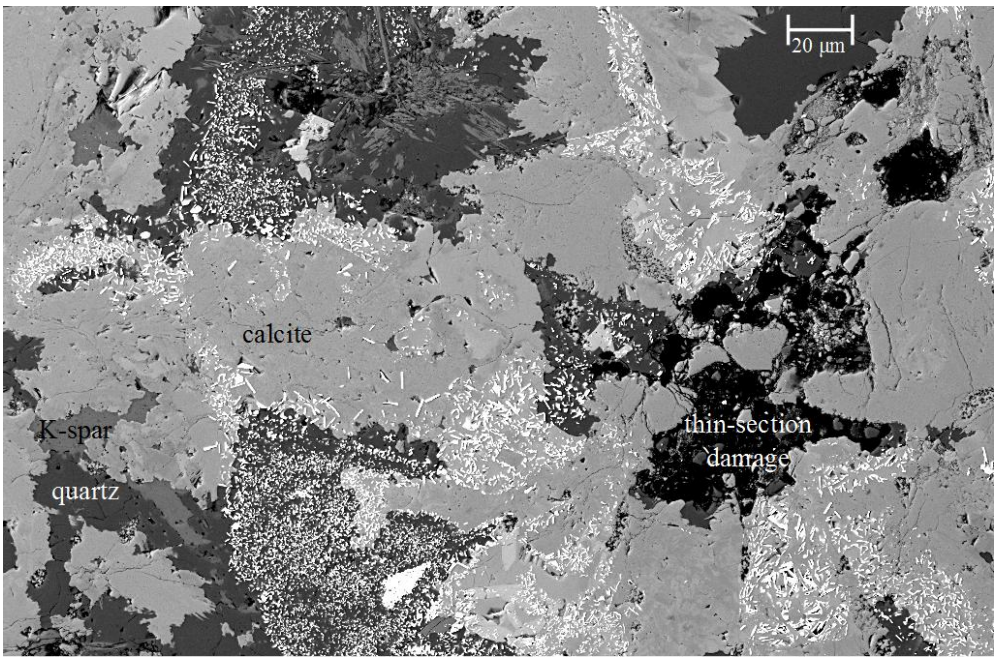

Figure 15: SEM close-up of iron oxide alteration (white) in sample 15, showing its relationship to other crystals (quartz, calcite and K-feldspar).

3.2.2 Lapilli tuff

The matrix of the lapilli tuff in sample 2c contains larger (up to 1 mm) crystals of albite (Ab_{94-99}), K-feldspar (Or_{97-98}), and quartz, and smaller crystals of augite (Wo_{23-30} $En_{29-40}Fs_{29-46}$, average Mg# 64), titanite, albite, and K-feldspar. It also includes iron oxide and quartz alteration products, and K-feldspar in a crack in albite. In sample 17 the larger crystal clasts are of augite ($Wo_{32-48}En_{35-42}Fs_{11-25}$, average Mg# 81), quartz, and K-feldspar, and the smaller ones are quartz and chalcopyrite. Some basalt clasts were also observed, and these contain crystals including augite, and amygdales infilled with quartz and chlorite.

Framework basalt clasts within the lapilli tuff (sample 29b) include phenocrysts of albite (Ab_{78-97}), diopside ($Wo_{47-48}En_{39-40}Fs_{12-13}$), and quartz, in a groundmass comprising diopside and augite ($Wo_{39-49}En_{26-39}Fs_{12-23}$), albite ($Ab_{92-96}$), chlorite, and titanite. Mg# of clinopyroxene averages 78. Amygdales are filled with prehnite, quartz, pumpellyite, and chlorite.

The unusual sample 28 includes phenocrysts of diopside ($Wo_{45-49}En_{37-41}Fs_{8-17}$), and albite with extensive alteration to prehnite and quartz. Its groundmass comprises albite (Ab_{83-95}), diopside, and titanite. Some diopside phenocrysts are zoned, with increasing Fe and Al and decreasing Mg and Ca towards the rims. Their Mg# averages 84.

3.2.3 Tuff

Relatively large (~ 100 μm – 0.5 mm) crystal clasts in tuff include albite (Ab_{92-97} in sample 4, Ab_{94-100} in sample 30), quartz, K-feldspar (Or_{97} in sample 4, Or_{97-98} in sample 30), and pyrite (only in sample 4), with some clasts altered to prehnite in sample 30. The pyrite crystals in sample 4 contain inclusions of prehnite. Basalt clasts within this tuff have mineralogy including albite, K-feldspar, quartz, pyrite and chalcopyrite, with chlorite filling amygdales and alteration of iron oxide and apatite (the latter in veins). Most clasts comprise extremely small crystals (< 10 μm), suggesting they may have metamorphically recrystallised from glass. The matrix (or pseudomatrix) consists of albite, quartz, K-feldspar, pyrite, titanite, and apatite.

The finer-grained tuff (sample 2a, without distinguishable larger clasts) comprises albite (Ab_{93-98}), K-feldspar (Or_{92-97}), quartz, pyrite, and chalcopyrite, with minor apatite and titanite. The pyrite and chalcopyrite are disseminated at the borders of other grains. The vein through this tuff has a centre entirely of quartz, with some K-feldspar at the finer-grained edges, and chlorite borders beyond that.

3.2.4 Argillite

The argillite contains clasts of augite ($Wo_{45-47}En_{31-40}Fs_{13-20}$, average Mg# 79), albite (Ab_{89-96}), and K-feldspar (Or_{94-98}), with minor amounts of titanite and apatite, and large and small crystals of pyrite throughout. Calcite forms the cement, and this appears under the SEM to comprise acicular or smoother crystals surrounding augite clasts (fig. 16). Pyrite is in places concentrated in veins, like those seen in hand specimen but much smaller.

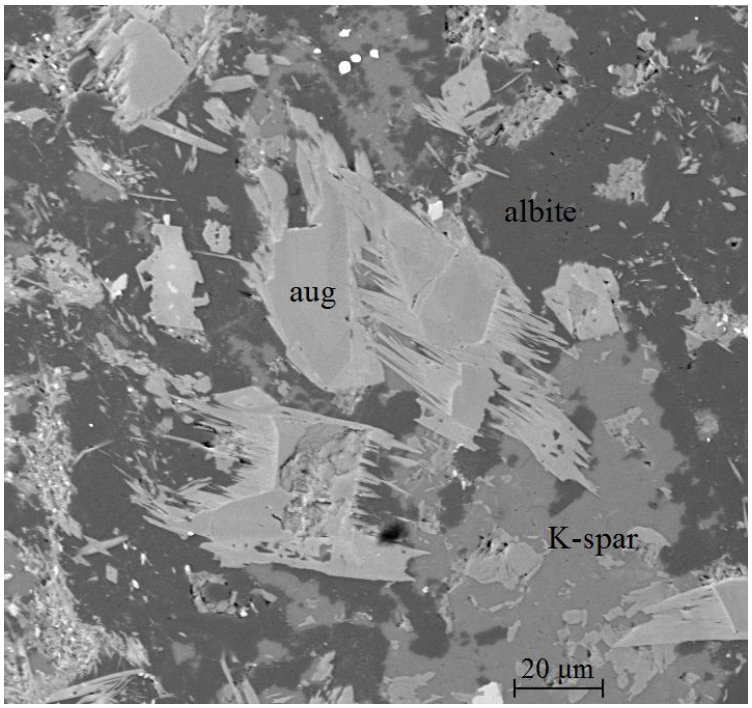

Figure 16: SEM image of acicular calcite crystals surrounding augite.

3.2.5 Dikes

Of the dikes, only sample 29a has phenocrysts of clinopyroxene (diopside and augite; $Wo_{43-47}En_{35-38}$ Fs_{14-18}), and the albite phenocrysts it contains are highly altered. The other dike samples have phenocrysts of albite (Ab_{90-97} in sample 2b, Ab_{86-92} in sample 21b) with K-feldspar zoning (Or_{97-99} in sample 2b, Or_{95-97} in sample 21b). The phenocrysts of sample 2b also have prehnite alteration. The groundmass in sample 29a consists of albite (Ab_{88-97}), clinopyroxene (diopside and augite; $Wo_{39-47}En_{27-37}Fs_{14-31}$), chalcopyrite, and titanite, while that in sample 21b comprises augite ($Wo_{37-46}En_{23-39}Fs_{19-38}$), albite ($Ab_{83-84}$), iron oxide, and titanite, and that in sample 2b contains albite (Ab_{87-97}), titanite, pyrite, and iron oxide, with no clinopyroxene. The average Mg# of clinopyroxene in 29a is 76, while that in 21b is 67. Amygdales in all three samples contain chlorite and prehnite, and those in sample 29a also include pumpellyite, quartz, and chalcopyrite. Some clinopyroxenes in sample 21b are zoned, including a few groundmass clinopyroxenes (fig. 17), with multiple concentric zones, and some groundmass titanite crystals have hopper crystal shapes (fig. 17). There is some compositional variation within prehnite-filled amygdales, with differences in Fe, Mg, and Ca content in a small area.

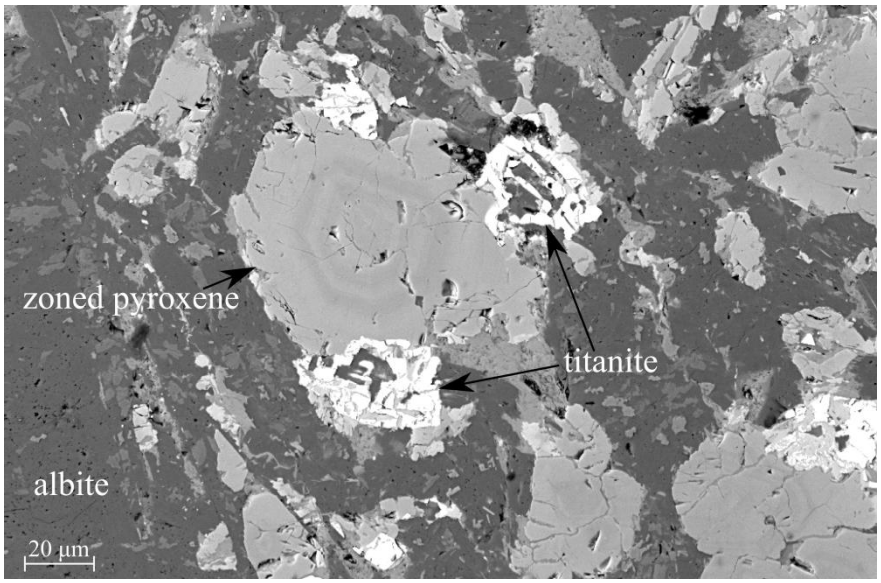

Figure 17: SEM image of oscillatory zoning in clinopyroxene and hopper titanite crystals filled with albite in sample 21b.

3.2.6 Clinopyroxenes

The majority of clinopyroxenes are compositionally classified as augites or diopsides, although one analysed falls in the hedenbergite field (fig. 18). The dikes occupy the largest compositional range, though it is clinopyroxenes from lapilli tuffs that fall furthest outside the range occupied by the other samples.

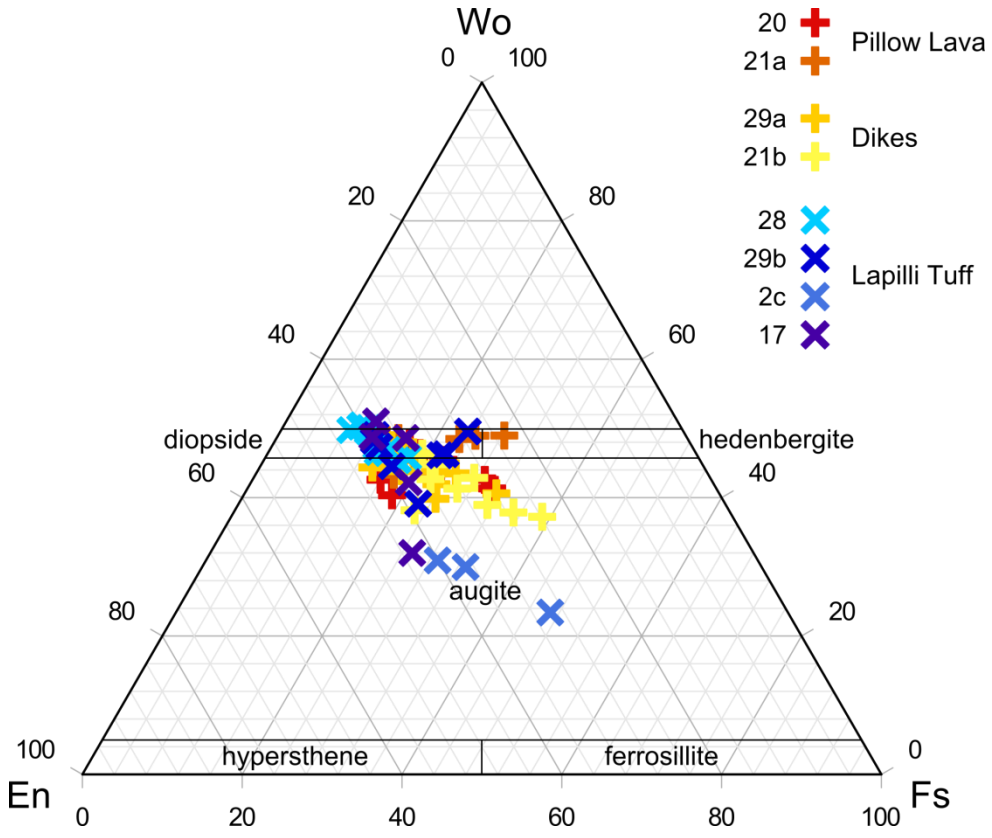

Figure 18: triangular diagram for clinopyroxene compositions.

4. Trace Element Geochemistry

4.1 Analytical methods

The trace element compositions of clinopyroxenes were analysed at the Centre for Trace Element Analysis at Otago University by laser ablation inductively coupled plasma mass spectrometry (LA-ICP-MS), using a Resonetics RESOlution M-50-LR excimer (193 nm) laser ablation system coupled to an Agilent 7500 cs/ce Quadrupole ICP mass spectrometer. Clinopyroxenes were used because they appear fresh in thin section and are thought to be largely unaffected by the metamorphic processes that have albitized the plagioclase and chloritized any olivine that might have originally been present in the rocks. The clinopyroxenes analysed are all augite, a primary phase in tholeiitic basalts.

Eight polished thin sections were analysed, including two pillow lavas (samples 20 and 21a), two dikes (samples 21b and 29a), two basalt clasts from within lapilli tuff (samples 28 and 29b), one sample from the matrix of lapilli tuff (sample 17), and one sample of tuff (sample 5). For all samples except the pillow lavas, five of the largest, freshest augites were selected and laser ablation tracks with 400 μm transects and 50 μm spot sizes were made along the rim and through the centre of each. The pillow lavas analysed lack phenocrysts so ten groundmass augites were analysed for each of them using a smaller spot size of 33 μm and transect of 200 μm. Ablation lasts for 40 s at 10 Hz with a fluence of 2.50 J/cm^2. All runs used a mixture of Ar and He as a carrier gas. Standard synthetic reference glass 610 was measured at the beginning and end of each thin section to correct for instrument drift. A rapid pre-analysis ablation was performed before each transect to clean the analysed surface.

Whole-rock trace element concentrations were estimated using clinopyroxene-liquid partition coefficients from Bédard (2014), in order to compare this data with whole-rock data from the Brook Street Terrane. Calculating simulated whole-rock data from clinopyroxene composition introduces some uncertainties, but given the petrographic evidence of pervasive mineralogic alteration in this hydrothermally altered rock it is thought to yield results closer to the original composition of the liquid than would a direct measurement of the whole rock. In order to perform these calculations, the distribution coefficients were taken from the supplemental data of Bédard (2014) (who had compiled

them from a number of sources), and an average of these values were used. The model whole-rock data were calculated for the averages of trace element concentrations from the cores of augites (table 1), using the equation $C_i^L = \frac{C_i^{cpx}}{D_i^{cpx/L}}$ where C_i^L is the concentration of a given element in the liquid, C_i^{cpx} is the concentration within clinopyroxene, and $D_i^{cpx/L}$ is the distribution coefficient between clinopyroxene and liquid.

4.2 Results

Trace element compositions of clinopyroxenes display patterns typical of island arc tholeiites (fig. 19). These data display a wide range of absolute concentrations of trace elements. Clinopyroxenes in basalts have significantly higher concentrations than do those in volcaniclastic rocks, and the unusual sample 28 has by far the lowest concentrations.

More heed is paid to core analyses because they are thought to be more reliable than rim analyses, several of which may be contaminated by the groundmass. Table 1 and Figure 19 display the averages of each set of core analyses, with a few outliers removed. All data are presented in Appendix A. Rims generally display slightly higher concentrations than cores, and most exhibit the same patterns. In addition to having lower concentrations, sample 28 shows a wider spread of concentrations among the clinopyroxenes analysed.

Table 1: average trace element concentrations (ppm) from the cores of augites for each sample.

Rock type	Pillow lavas		Dikes		Lapilli tuffs			Tuff
Sample	20	21a	21b	29a	17	28	29b	5
Li	2.10	1.27	1.17	1.07	0.68	0.73	0.77	0.77
Be	0.21	0.11	0.16	0.02	0.12	0.004	0.06	0.10
K	266.29	81.41	89.88	4.78	10.22	5.96	20.08	2.22
Sc	146.84	159.43	129.58	106.34	105.76	83.60	113.18	107.97
Ti	5071.81	3610.71	3249.26	2595.70	1488.83	1264.09	2049.57	1890.27
V	469.32	430.44	376.55	312.67	224.64	162.34	303.25	227.64
Cr	265.45	1156.20	1770.92	1573.34	3027.26	2926.86	1278.60	2576.45
Mn	1470.39	1297.27	1606.57	1564.94	937.66	843.62	1251.81	954.80
Co	44.61	43.45	44.81	40.87	36.61	32.97	41.06	34.65
Ni	67.43	140.89	128.74	166.12	186.93	173.26	118.18	185.54
Cu	37.61	8.48	3.80	8.16	3.18	2.44	6.67	5.07
Zn	39.91	28.05	43.81	39.64	21.16	16.06	27.35	21.45

Ga	7.76	6.34	5.62	4.52	3.30	2.22	3.55	3.37
Ge	2.57	2.46	2.84	3.08	2.56	2.44	2.90	2.68
As	0.51	0.34	0.23	0.16	0.12	0.08	0.17	0.22
Rb	1.71	0.12	0.31	0.04	0.08	0.05	0.19	0.02
Sr	27.58	17.58	18.47	28.32	13.49	13.17	14.78	16.43
Y	18.68	13.27	14.13	11.49	5.62	3.94	8.48	6.80
Zr	33.11	21.33	11.67	8.93	4.95	2.09	5.78	6.00
Nb	0.14	0.07	0.02	0.01	0.03	0.003	0.01	0.01
Cs	0.13	0.02	0.05	bdl	0.003	0.003	0.01	0.01
Ba	2.43	0.83	0.39	0.10	0.20	0.03	0.07	0.09
La	0.56	0.37	0.36	0.32	0.16	0.09	0.19	0.20
Ce	2.71	1.67	1.84	1.86	0.73	0.43	1.03	0.87
Pr	0.63	0.43	0.46	0.46	0.18	0.12	0.27	0.23
Nd	4.46	3.14	3.46	3.00	1.36	0.86	2.02	1.67
Sm	2.11	1.47	1.60	1.30	0.68	0.43	0.95	0.78
Eu	0.77	0.57	0.58	0.51	0.25	0.17	0.35	0.28
Gd	3.01	2.11	2.37	2.02	0.95	0.66	1.41	1.10
Tb	0.54	0.38	0.41	0.33	0.16	0.11	0.25	0.20
Dy	3.61	2.60	2.88	2.33	1.14	0.82	1.71	1.34
Ho	0.76	0.53	0.58	0.47	0.23	0.16	0.34	0.27
Er	2.15	1.55	1.67	1.34	0.65	0.46	0.96	0.79
Tm	0.28	0.20	0.22	0.18	0.09	0.06	0.13	0.10
Yb	1.88	1.38	1.45	1.15	0.57	0.37	0.83	0.64
Lu	0.27	0.19	0.21	0.16	0.08	0.05	0.12	0.09
Hf	1.61	1.11	0.64	0.49	0.26	0.13	0.32	0.32
Ta	0.02	0.01	0.002	0.0005	0.002	0.0001	0.0005	0.0003
Pb	0.45	0.12	0.10	0.59	0.35	0.03	0.05	0.26
Th	0.02	0.01	0.005	0.003	0.004	0.0002	0.001	0.001
U	0.02	0.01	0.002	0.0003	0.001	0.0003	0.001	0.001

A positive Pb anomaly, as seen in samples 5, 17, 20, and 29a, is characteristic of island arc rocks. However, some of these samples (21a, 21b, 28, and 29b) display a negative Pb anomaly, which is more commonly associated with mid-ocean ridge basalts or back-arc volcanics. With the exception of sample 28 (which is an unusual sample in every context in which it is examined), the samples with a negative Pb anomaly all have higher concentrations of Th than Ba, higher Ta than Nb, and a pronounced negative Sr anomaly. The samples with positive Pb anomalies are more variable, without any particular consistent trait common to them which is not common to all of the samples.

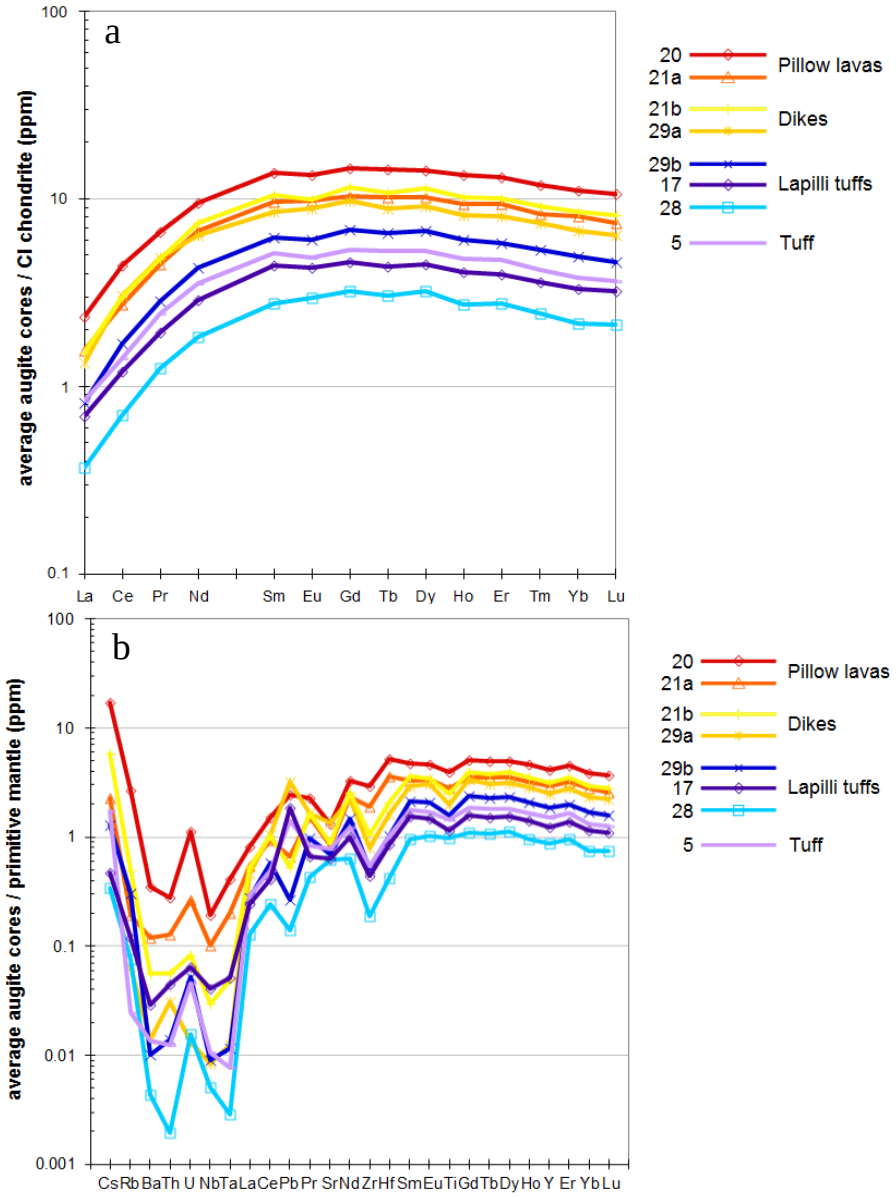

Figure 19: a) chondrite-normalised rare earth element (REE) and b) primitive mantle-normalised trace element profiles for the averages of the cores of augites for each sample. Normalising values from Sun and McDonough (1989).

A plot of Zr against Sr concentrations (fig. 20a) reveals a trend broadly consistent with the cpx + ol ± plag fractionation trend of Rossel et al. (2015), in which the pillow lavas appear most fractionated, though still at low values compared to those in the paper; the volcaniclastic rocks cluster at lower values (low degrees of fractionation), and the unusual clast 28 shows the lowest values. A Sr vs Yb plot (fig. 20b) supports this fractionation trend.

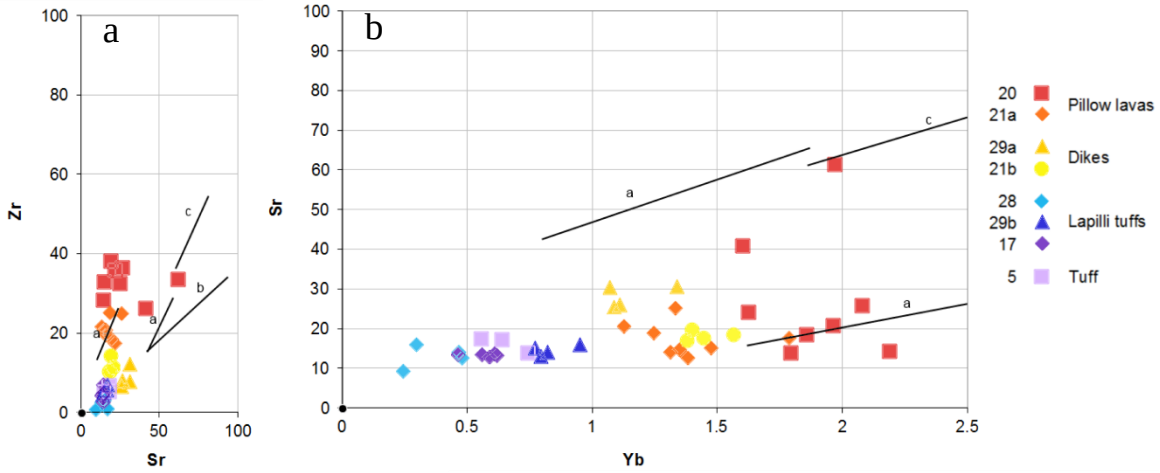

Figure 20: plot of a) Zr vs Sr, and b) Sr vs Yb. Black lines are fractionation patterns of Rossel et al. (2015): a = cpx + ol ± plag, b = cpx, c = cpx ± plag. Key applies to both graphs.

According to Maurice et al. (2012), it is possible to obtain an indication of the mobility of elements during hydrothermal alteration and metamorphism by plotting them against an immobile element such as Zr. Here a good correlation with Zr indicates low mobility. In my samples (fig. 21), Hf correlates very well with Zr; Nb, La, and Th correlate reasonably well; and Rb and Sm correlate poorly (suggesting that Rb and Sm were mobile during alteration).

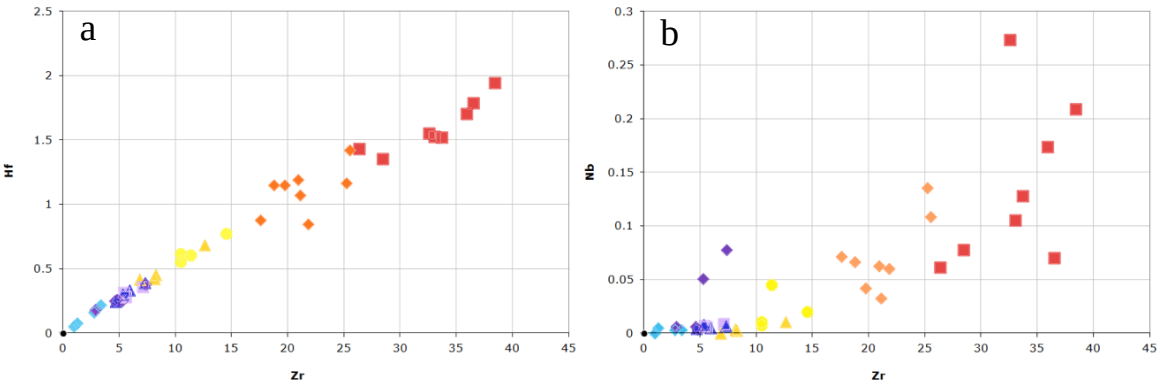

Figure 21: plots of major elements against Zr; key in bottom right (beside plot f) applies to all graphs.

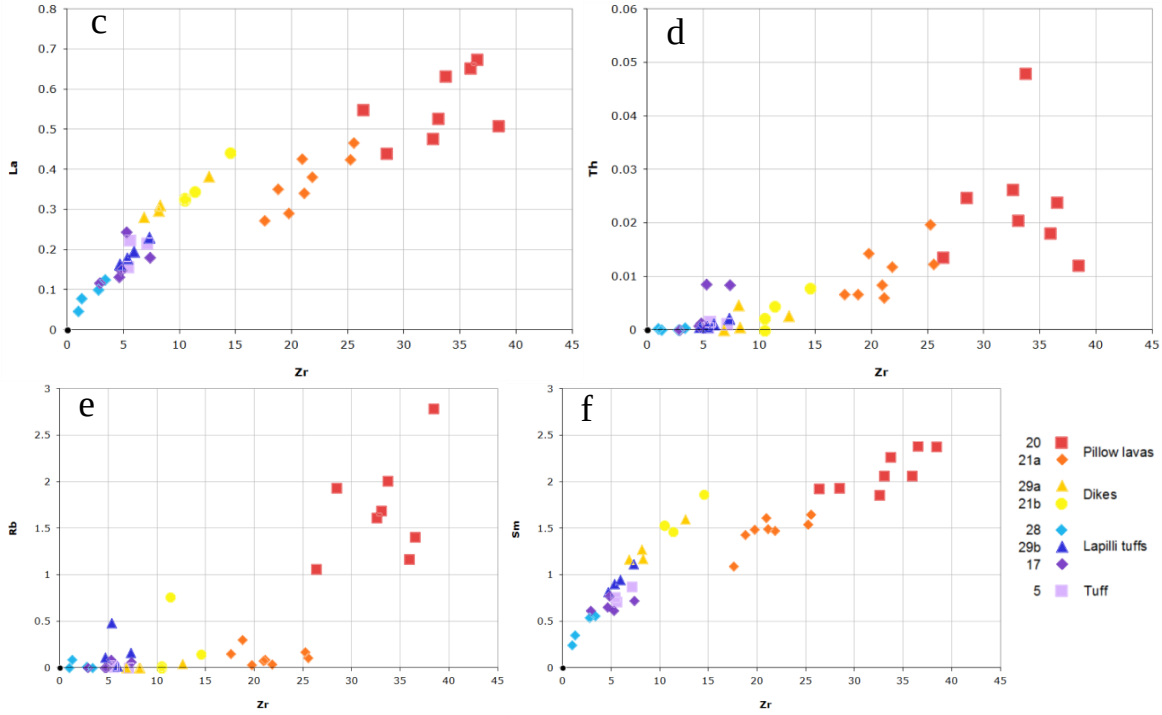

Figure 21 continued: plots of major elements against Zr; key in bottom right applies to all graphs.

Whole-rock compositions modelled from clinopyroxene data were calculated from the clinopyroxene trace element data; the results are displayed in Table 2 and Figure 22.

Table 2: model whole-rock compositions (ppm) calculated from average trace element concentrations from the cores of augites for each sample. Partition coefficients (D) are averages taken from Bédard (2014).

	D	Pillow lava		Dikes		Lapilli tuffs			Tuff
		20	21a	21b	29a	17	28	29b	5
Li	0.275	7.63	4.61	4.49	3.87	2.49	2.65	2.79	2.82
Be	0.054	3.87	1.95	3.15	0.34	2.28	0.08	1.03	1.90
K	0.0067	9744.75	12151.10	13414.88	713.35	1524.73	889.43	2996.87	330.63
Sc	1.675	87.68	95.19	76.72	63.49	63.15	49.91	67.58	64.46
Ti	0.317	6003.01	11383.30	10243.79	8183.32	4693.75	3985.24	6461.59	5959.36
V	2.098	223.74	205.21	178.29	149.06	107.09	77.40	144.57	108.52
Cr	5.15	51.54	224.51	368.74	305.50	587.82	568.32	248.27	500.28
Co	1.386	32.18	31.34	32.18	29.48	26.41	23.78	29.62	24.99
Ni	4.406	15.31	31.98	29.96	37.70	42.43	39.32	26.82	42.11
Cu	1.26	29.85	6.73	3.45	6.48	2.52	1.94	5.29	4.03
Zn	21.287	1.87	1.32	2.12	1.86	0.99	0.75	1.28	1.01
Ga	0.375	20.71	16.90	15.24	12.05	8.80	5.92	9.46	8.98
Ge	1.386	1.85	1.78	2.05	2.22	1.85	1.76	2.10	1.93
As	0.019	26.65	17.77	11.83	8.59	6.28	3.95	9.18	11.42

	D	Pillow lava		Dikes		Lapilli tuffs			Tuff
		20	21a	21b	29a	17	28	29b	5
Rb	0.012	137.12	9.93	34.04	3.29	6.12	3.83	15.61	1.26
Sr	0.090	305.14	194.56	207.93	313.39	149.23	145.71	163.54	181.80
Y	0.427	43.73	31.05	32.80	26.90	13.15	9.22	19.85	15.91
Zr	0.118	280.86	180.96	98.47	75.76	41.98	17.75	49.01	50.91
Nb	0.0046	30.05	15.86	5.74	1.31	6.41	0.79	1.41	1.65
Cs	0.0041	32.38	4.36	12.19	bdl	0.90	0.66	2.47	3.34
Ba	0.0052	468.26	159.94	112.87	18.58	38.58	5.80	13.69	18.29
La	0.048	11.64	7.70	7.42	6.65	3.44	1.82	4.01	4.13
Ce	0.088	30.66	18.97	20.65	21.03	8.29	4.85	11.67	9.86
Pr	0.125	5.03	3.39	3.60	3.66	1.46	0.95	2.16	1.85
Nd	0.209	21.31	15.00	16.35	14.30	6.48	4.12	9.65	7.96
Sm	0.324	6.52	4.55	4.85	4.02	2.09	1.32	2.93	2.41
Eu	0.397	1.95	1.44	1.44	1.30	0.63	0.44	0.88	0.71
Gd	0.412	7.30	5.12	5.73	4.89	2.30	1.60	3.41	2.67
Tb	0.381	1.41	0.99	1.05	0.88	0.43	0.30	0.65	0.52
Dy	0.518	6.98	5.01	5.49	4.51	2.20	1.59	3.30	2.58
Ho	0.431	1.77	1.24	1.33	1.08	0.54	0.36	0.80	0.63
Er	0.574	3.75	2.71	2.88	2.33	1.14	0.80	1.68	1.37
Tm	0.427	0.66	0.47	0.51	0.42	0.20	0.14	0.30	0.24
Yb	0.470	4.00	2.93	3.06	2.45	1.20	0.78	1.77	1.37
Lu	0.459	0.59	0.41	0.45	0.36	0.18	0.12	0.26	0.20
Hf	0.223	7.19	4.98	2.83	2.21	1.19	0.58	1.43	1.43
Ta	0.013	1.30	0.64	0.16	0.04	0.16	0.01	0.04	0.02
Pb	0.108	4.19	1.14	1.14	5.49	3.20	0.24	0.46	2.44
Th	0.012	1.92	0.89	0.39	0.21	0.31	0.01	0.10	0.09
U	0.015	1.60	0.38	0.12	0.02	0.09	0.02	0.08	0.07

These data were compared with published whole-rock data from the Brook Street Terrane taken from Spandler et al. (2005) (fig. 22). The two profiles from Spandler et al. (2005) shown in Figure 22 are from sites within the field area. These results generally match quite well, and confirm that my data are consistent with the island arc signature of the Brook Street Terrane as reported by other authors. Some mismatch occurs, attributable to a number of factors. My calculated melt values are based on distribution coefficients which have uncertainties, and the ‘bumps’ in Zr-Hf and Th-U (for example; fig. 22b) may be artefacts of this uncertainty, as might the jagged rare earth element (REE) patterns (fig. 22a). Large ion lithophile element (LILE) concentrations in clinopyroxene are low, and this in combination with uncertainties in distribution coefficients may result in some scatter. These rocks are altered, and Spandler et al. (2005) acknowledge that this alteration affected their data (particularly in Cs, Rb, Ba, Pb, Sr and U), which clinopyroxene data may be more robust to.

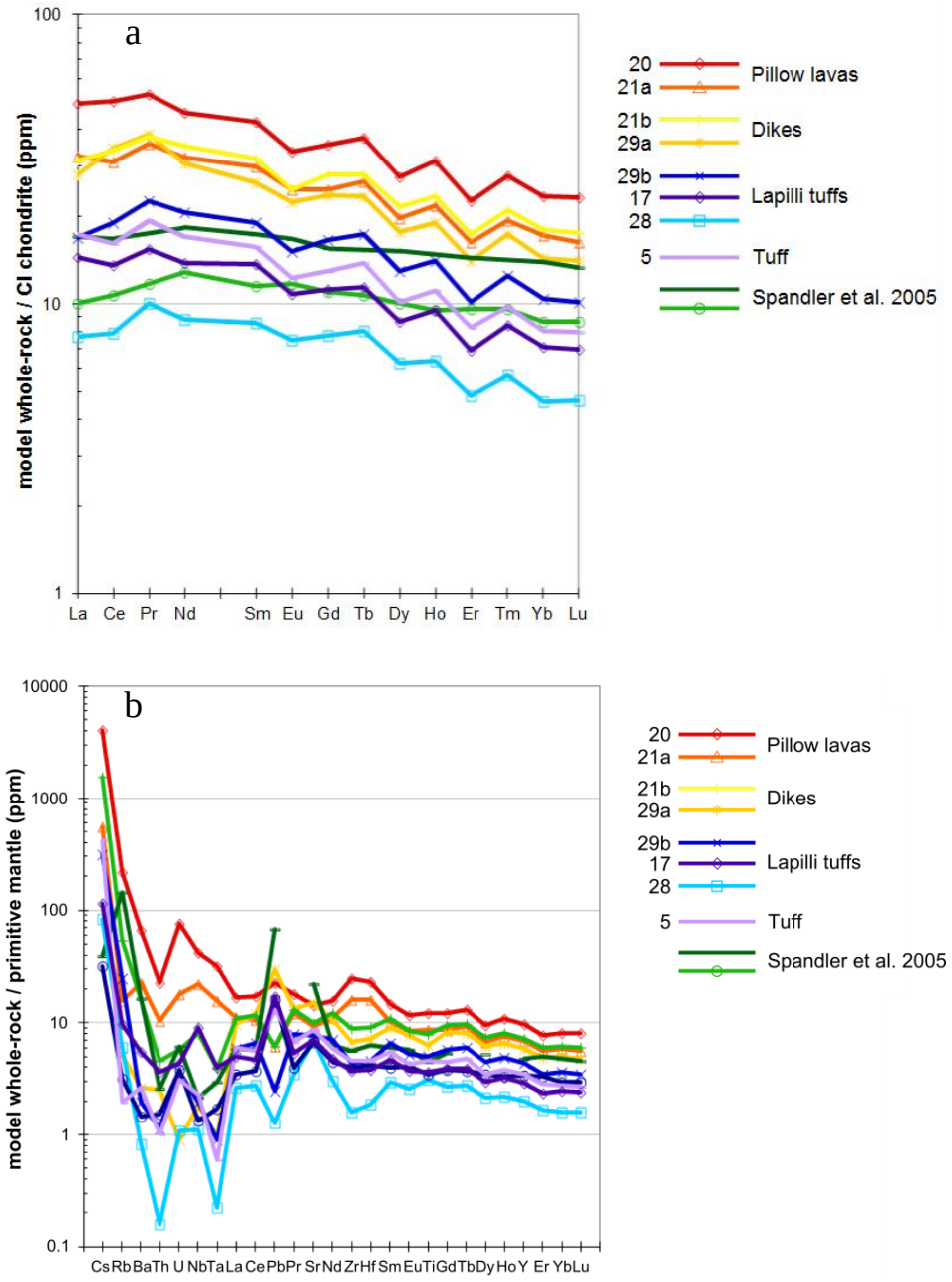

Figure 22: calculated model whole-rock a) chondrite-normalised rare earth element and b) primitive mantle-normalised trace element profiles, compared to whole-rock data from Spandler et al. (2005), showing similar patterns with a few notable differences (discussion in text). Normalising values from Sun and McDonough (1989).

High field strength elements (HFSE), LILE and LREE may be used in plots of M/Yb vs. Nb/Yb (where M is the element in question) to evaluate mantle and slab contributions to magma (fig. 23), as these are incompatible elements whose concentrations will change depending on these contributions (Pearce and Peate, 1995, Maurice et al.,

2012). HFSE behave conservatively during subduction, so their concentrations reflect the composition of the mantle wedge, whereas LILE and LREE are nonconservative and thus related to the contribution from the subducted slab. Maurice et al. (2012) use whole-rock compositions, so calculated whole-rock data is used to compare to theirs. On the HFSE Zr/Yb, Y/Yb, and Sm/Yb vs Nb/Yb diagrams, my samples plot within the mantle array (fig. 23a, b, c), indicating derivation from the mantle, with a wide spread that suggests a variably enriched and depleted source. Plots using the LREE La and the LILE Th, Ba, and U (fig. 23d, e, f, g) in the same way yield results scattered within, above and below the mantle array; positioning above the mantle array would indicate derivation from the subducted slab. According to Pearce and Stern (2006), plotting between the mantle array and the volcanic arc array on the Ba/Yb vs. Nb/Yb plot is characteristic of back-arc basin basalts, which are transitional between island-arc tholeiites and mid-ocean ridge basalts (MORB). The presence of data which plots within the mantle array indicates some involvement of a back-arc spreading ridge (Pearce and Stern, 2006). The paucity of the slab signal is consistent with the assertion of Faure (2001) that some island arc magmas have very little contribution from the subducted slab; although this has not been proven for the Brook Street arc, Houghton and Landis (1989) and Spandler et al. (2005) do state that the Brook Street Terrane is immature and contains little continental input. According to Maurice et al. (2012), low ratios of Th/Yb such as these should indicate a lack of input from melted sediments. The general pattern of enrichment in these plots is broadly consistent with the variation in absolute concentrations of incompatible elements (fig. 23, fig. 19). Pillow lavas form a group, which is generally more enriched than the other samples; these are more scattered. Samples plot in varying positions relative to N-MORB and E-MORB; most cluster around N-MORB, but the spread is significant. This is unusual, and may be an artefact of the calculation of whole-rock values; plots using the original data from clinopyroxenes are inconsistent with the whole-rock plotted positions of the mantle array, but they do consistently fall at lower values than N-MORB.

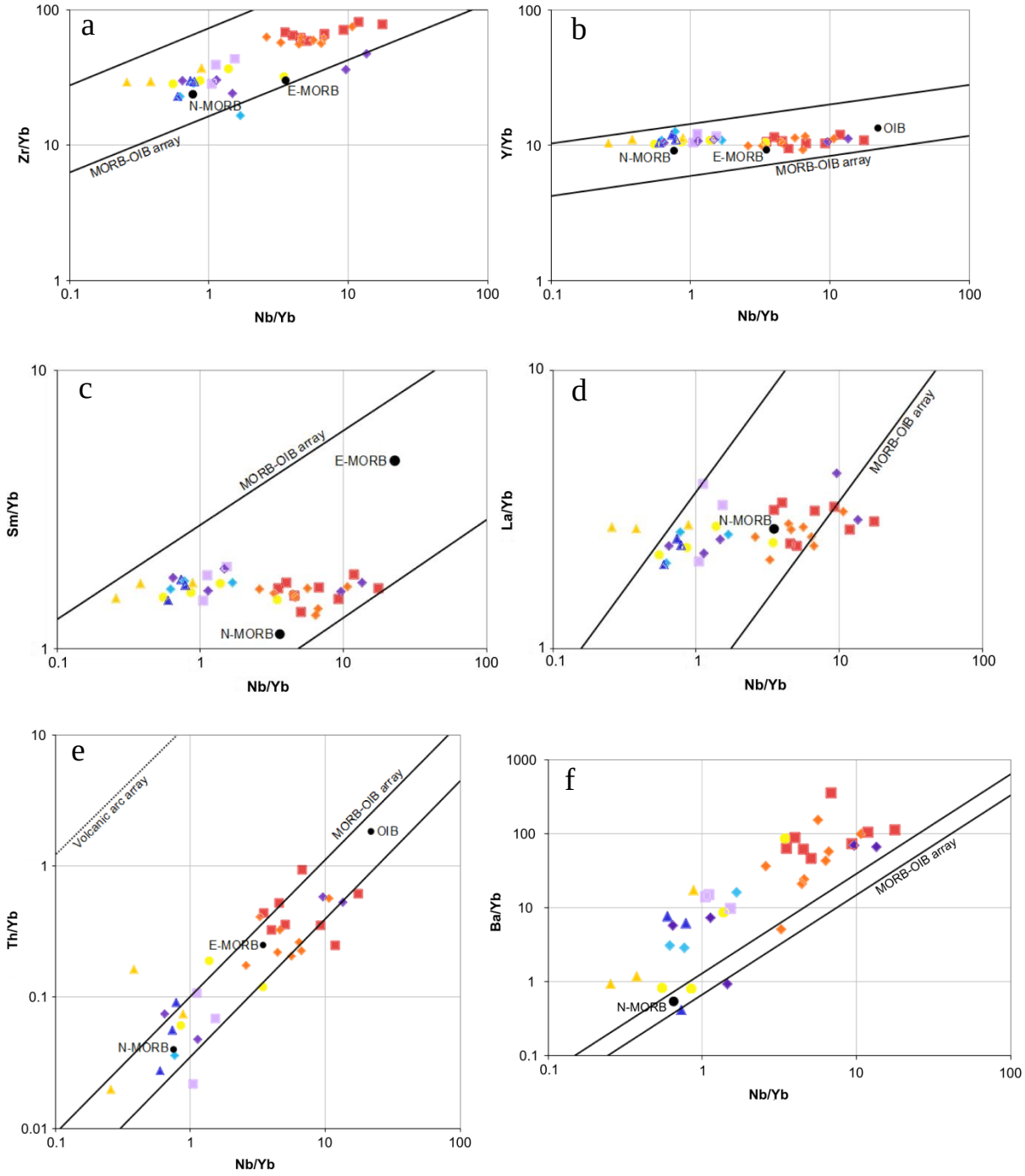

Figure 23: plots of M/Yb vs. Nb/Yb after Maurice et al. (2012) and Pearce and Stern (2006). Key beside diagram g applies to all diagrams.

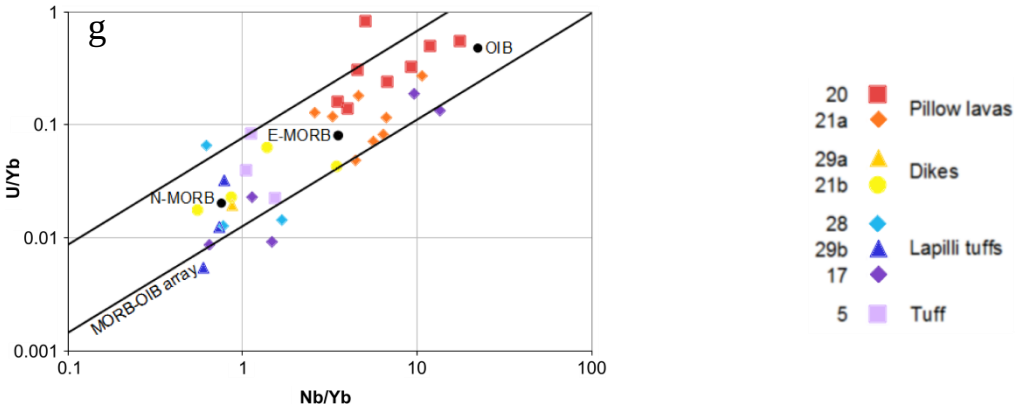

Figure 23 continued: plots of M/Yb vs. Nb/Yb after Maurice et al. (2012) and Pearce and Stern (2006). Key beside diagram g applies to all diagrams.

5. Secondary Features

All rocks in this area have undergone hydrothermal alteration and regional metamorphism, to varying degrees. All plagioclase (which would have been anorthite-rich in an unaltered rock of this composition) is albitised, and some also bears pumpellyite and clay alteration. The abundance of chlorite, some of which pseudomorphs crystal shapes, and absence of olivine suggests that all olivine has been chloritised. Calcite and/or quartz form secondary cement in argillite, lapilli tuff, and the recrystallised inter-pillow matrix. Pillow rims are either not preserved or have lost their glassy texture, and only devitrified glass is discernible in thin section. Some clasts in tuff and lapilli tuff are deformed to form pseudomatrix, and original matrix is not discernible. Throughout the section vesicles are infilled by prehnite, pumpellyite, chlorite, quartz and albite, forming amygdales. Dikes display the most variation in degree of alteration, with some altered to the same extent as the rock around them, while others appear relatively fresh.

Some pillows at site 19 are veined with networks of pale veins; some of these have splotchy alteration spreading out from them. This texture suggests that these veins originated as alteration along cracks. At site 16 there is a region of pillows which is dark red and far more weathered in appearance, with a rough, pitted surface, though the dikes through it do not display these characteristics.

The fact that vesicles at the edges of clasts in lapilli tuff are filled with matrix, rather than with secondary minerals (fig. 8b), suggests that hydrothermal alteration occurred after the deposition of the lapilli tuff. In some locations (sites 22, 26, 29) the matrix of the lapilli tuff has areas of prominent white quartz cement (fig. 7a); this is discontinuous, occurring over a few metres in each place, and at site 29 there are patches of matrix even within the affected region which lack quartz cement.

At site 4 there are scattered 7-30 cm circular shapes in the tuff, which appear coarser-grained and brighter green in colour. One layer at site 7 has similar spots, 2-20 cm and sometimes elongated. There is a layer at site 4 with pale elongate shapes surrounded by smaller pale blobs; these shapes are composed of quartz with a complex interwoven

texture (fig. 24a). This could be a metamorphic fluid flow feature, wherein permeating fluids follow the easiest path and precipitate as they do so.

Quartz veins are rarely present in these rocks. They are coarsely crystalline, ranging from white to yellow in colour, and varying from 1-70 mm in width along their observable length. Most cut through at low angles to horizontal, though some are steep or subvertical. At site 4 there is a set of cross-cutting veins, with steeply dipping veins offset along subvertical ones that must occupy small faults (fig. 24b). At site 33, in the lapilli tuff, several basalt clasts contain vugs up to 5 cm across with a dark red-brown botryoidal lining.

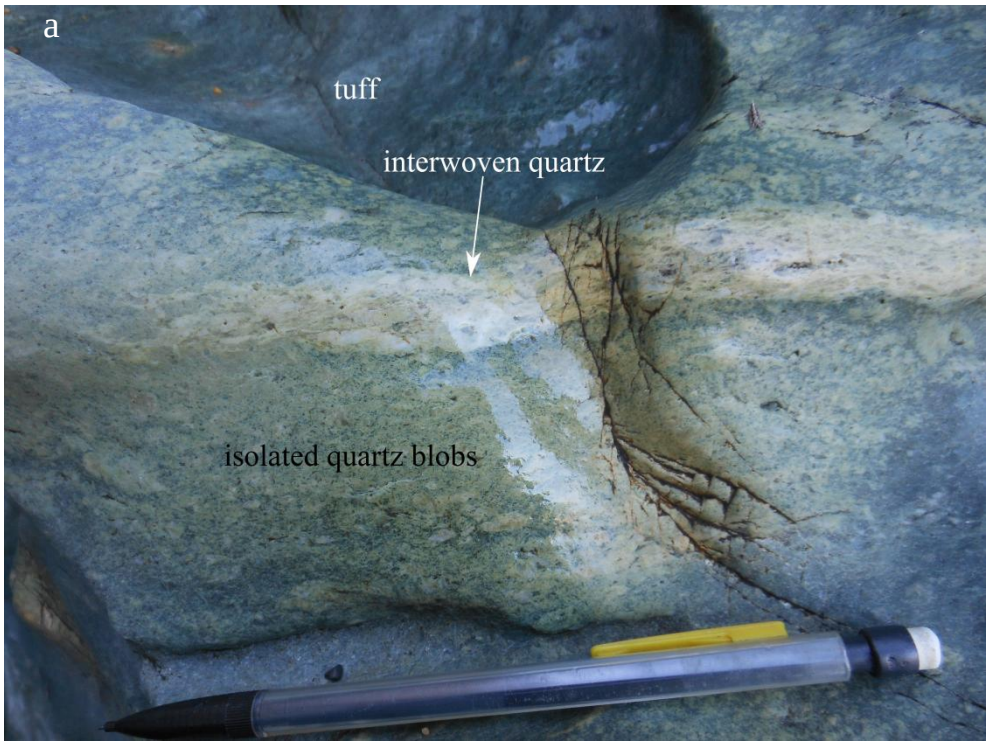

Figure 24: a) discontinuous quartz veins with interwoven texture in tuff (pencil for scale 15 cm).

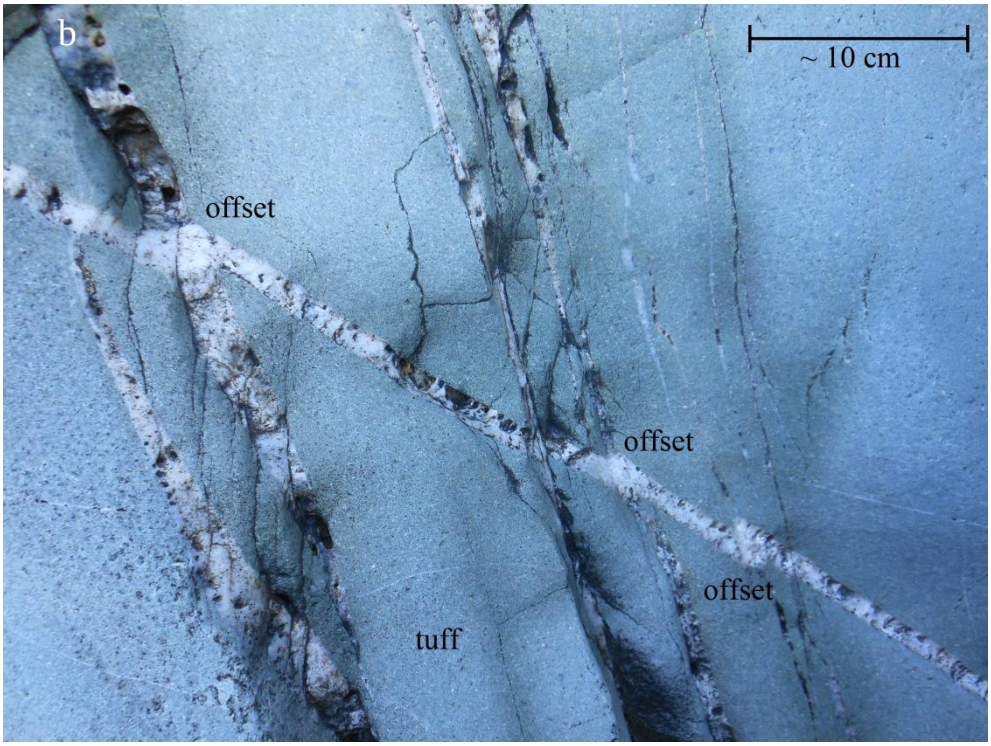

Figure 24 continued: b) cross-cutting quartz veins in tuff.

6. Structure

The orientations of bedding in the argillite vary widely, and can sometimes be seen to curve within a single outcrop (fig. 25). The shape is a broad anticline, with several shallow subordinate folds. Strike is at 101 ± 12, with dip varying from 21S to 08N.

The orientation of the tuff and lapilli tuff bedding varies over the area, with orientations including 097/22S, 131/21S, and 099/10S at site 2, 077/16S at site 7, 105/27S at site 10, 139/21S at site 14, 099/50S and ~129/49S at site 19, ~073/20S at site 21, 121/29S at site 23, and ~152/58W at site 29. Beds of these lithofacies were probably deposited with a small depositional dip, but the variation in orientation displayed is too great to be attributable to the slopes of a volcano. The varying dips of the tuff and lapilli tuff beds are thus interpreted as reflecting the same anticlinal structures, though these are less clear than they are within the argillite. Considering these orientations, it is likely that the trace of the anticline curves gradually southwards through the eastern end of the peninsula (plate 1).

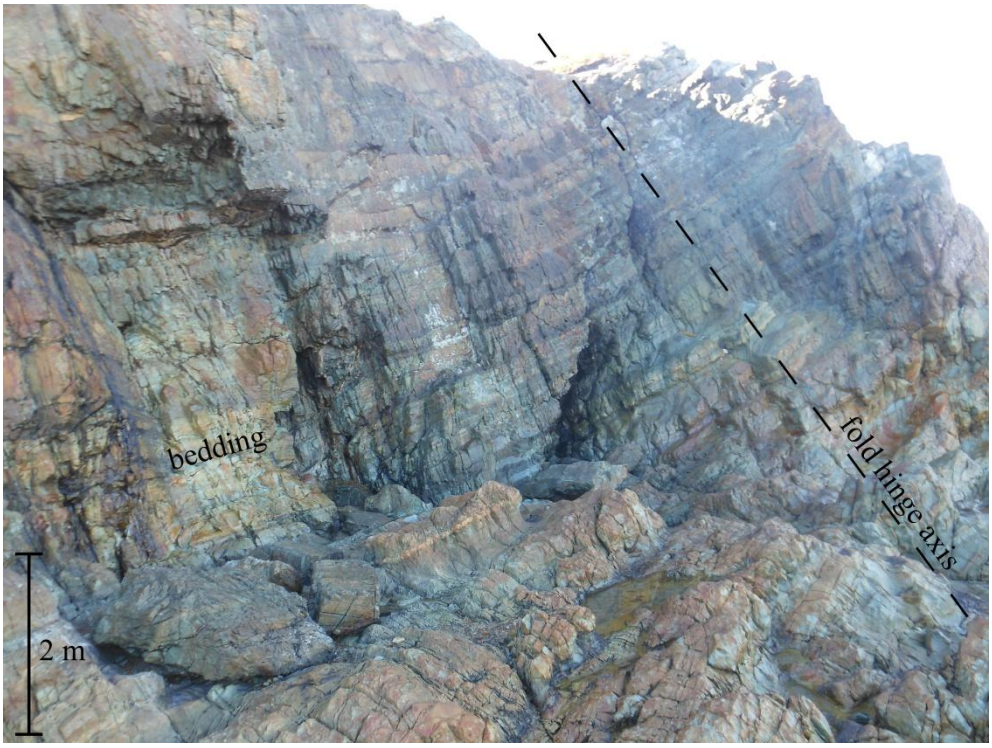

Figure 25: bedding within argillite at site 1 showing gradual change in orientation. Imaged outcrop face has overall NNW-SSE orientation.

7. Discussion

Submarine stratovolcanoes are highly heterogeneous, with changes between lithofacies at small spatial scales (Houghton and Landis, 1989, de Silva and Lindsay, 2015), as is observed in the Riverton section. The lateral changes in the Riverton section provide an indication of volcanic processes that occurred contemporaneously. Geochemical data allow me to develop a sequence of time and correlations regarding the relationship between source magma and surface deposits.

7.1 Interpretation of Geochemical Data

Trace element analyses of clinopyroxenes show these rocks to be island arc tholeiites, which are consistent with existing data from the Brook Street Terrane such as those from Spandler et al. (2005). On M/Yb vs Y/Yb plots, these data display patterns indicative of a back-arc basin origin, with a spreading ridge present. They probably had very little contribution from the subducted slab. These samples are variably enriched; pillow lavas are more enriched than the other samples.

Trace element analyses of clinopyroxenes in pillow lavas, dikes and volcaniclastic rocks reveal two distinct groups of geochemical signatures, one with a positive Pb anomaly, and the other with a negative Pb anomaly. Based on the differences between these two groups, the two pillow lavas analysed are two distinct units, and the volcaniclastics analysed divide into these two groups. With the exception of a dike at site 29, the two groups are distributed with the low-Pb rocks on the NE side of the Riverton peninsula, and the high-Pb group along the SW coast of Colac Bay.

Taking into account the lateral distribution of lithofacies, I interpret this to suggest the presence of two small volcanic centres: one centring on the largest pillow lava pile and displaying high-Pb signatures, the other to the NE with low-Pb signatures (fig. 26). The dike with a signature inconsistent with the area it outcrops in could have extended from the other volcanic centre; this suggests that the two vents were probably active contemporaneously. The presence of ‘segregation vesicles’ in sample 21a (fig. 5c)

suggests that this pillow lava (from the NE vent) had a higher volatile content than pillow lava sample 20 (from the SW vent).

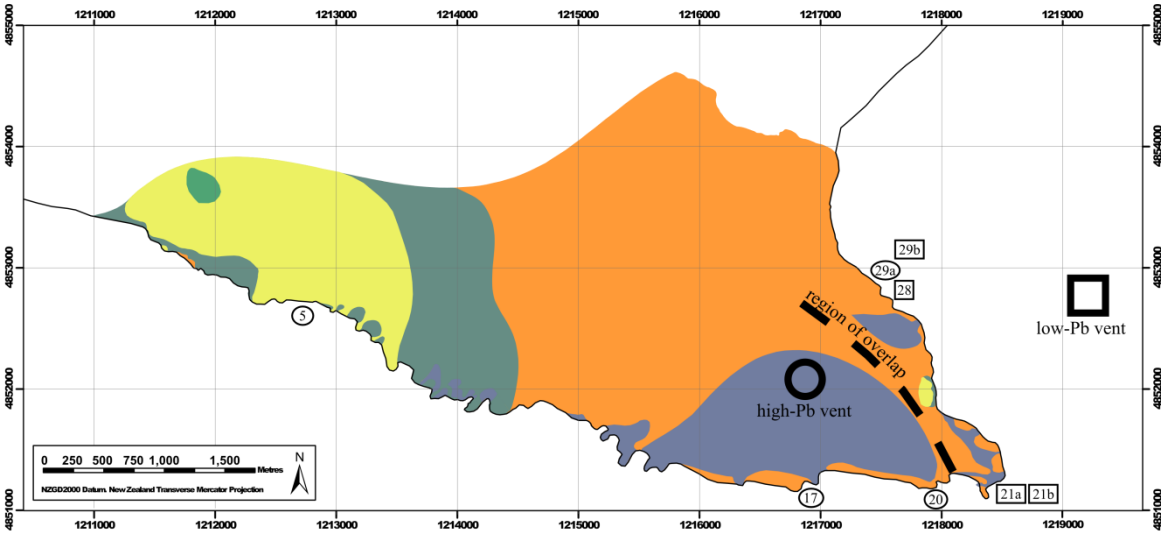

Figure 26: inferred positions of the proposed two small volcanic centres relative to mapped geology. Samples used for trace element geochemical analysis are marked on the map; those which display a positive Pb anomaly are marked with an oval symbol, and those with a negative Pb anomaly with a rectangle.

A positive Pb anomaly is generally considered characteristic of island arc rocks, whereas a negative Pb anomaly is associated with mid-ocean ridge basalt or back-arc volcanic affinities. According to Pearce and Stern (2006), many back-arc basin basalts are transitional in composition between arc and MORB. For example, in the Tonga-Kermadec arc and the Izu-Bonin arc, compositions vary across the arcs, related to the input of subduction-related and back-arc spreading-related magma, respectively (Ewart et al., 1998, Hochstaedter et al., 2000). Arc settings may display geochemical gradients between arc and back-arc, sometimes within restricted spatial extents (Ewart et al., 1998). Orton (1996) asserts that the volcanic arc and back-arc volcanoes can be as little as 5 km apart, and that the distinction between the two can be ill-defined. The Riverton rocks have island arc tholeiitic trace element patterns, and occupy back-arc positions on multi-element plots; together these characteristics suggest a transitional character, likely behind the arc but close to it. Thus, it is plausible for the two vents of this Riverton section to tap different mantle domains within a transitional arc-back-arc zone.

Island arc volcanoes are usually tens of kilometres in diameter and tens to hundreds of kilometres apart (Cas, 1992, Kano et al., 1993), so these small centres may be

satellite vents of a larger volcano. Satellite vents are commonly fed by small batches of magma which are separate from the main magma source and may vary widely in composition (Davidson and de Silva, 2000), so this is plausible in combination with the compositional variation.

Samples of clinopyroxenes from both the matrix of the tuff and lapilli tuff and the larger clasts within them all have lower concentrations of trace elements than those from the pillow lavas and dikes. This suggests that fractional crystallisation occurred in the magma reservoirs of both volcanic centres. Geochemical characteristics are consistent with these rocks following a cpx + ol + plag fractionation trend (Rossel et al., 2015), and the intergrowth of clinopyroxene and plagioclase observed in thin section suggests co-crystallisation of these minerals. The glomerocrysts present in some rocks indicate that magma was stored in a reservoir long enough for crystal mush to form at the margins of the reservoir, and later be caught up by erupting magma (Moore et al., 2014). The observation of zoned crystals in glomerocrysts and phenocrysts suggests that conditions fluctuated within the reservoirs during the times over which they formed (Moore et al., 2014).

7.2 Physical Processes

The presence of pillow lavas makes it clear that these volcanic rocks were formed in a subaqueous environment. Abundant turbidites and the absence of any wave-formed sedimentary structures suggest that the deposits formed below wave-base (Doucet et al., 1994, McPhie et al., 1993), and the abundance of fine-grained argillite suggests a relatively deep setting.

The pillow lava displays peperitic contacts (fig. 9c), and is thus inferred to have intruded unconsolidated deposits of ash and lapilli ash (White et al., 2015; fig. 28b). Inter-pillow matrix is present within most pillow lava outcrops; its composition and nature (fine- or coarse-grained) matches that of the volcaniclastic rock adjacent (tuff or lapilli tuff), and none has textures consistent with geopetal infilling (Garrison, 1972); all this is consistent with most pillow lava outcrops being intrusive. Many of the dikes display apophyses, undulating margins, and engulfed domains of lapilli tuff, indicating that they

also intruded unconsolidated material. Multiple layers of vesicles within both the dikes and the pillows indicate that multiple injections of magma occurred (Andrews, 2003). The large pillow lava pile may not be wholly intrusive, as it comprises a continuous edifice of pillow lava thicker than the lapilli tuff around it. Its lower and outer margins display peperitic contacts, implying intrusion into surrounding, previously emplaced volcaniclastic deposits. The pillowed intrusion is inferred to have continued growing upward until it emerged from the sediment and pillow lavas were ultimately extruded onto the seafloor (e.g. Garrison, 1972).

The lapilli tuff contains several distinct types of clasts. The dominant type closely resembles fragments of pillow lava, and these are present throughout the lapilli tuff, including in those parts of it which undoubtedly underlie the pillow lava observed. Fragments of dikes, identified by their characteristic flow banded texture and paucity of amygdales, are also present in the lapilli tuff. Within the matrix of the lapilli tuff, devitrified glassy clasts with abundant tiny (≤0.1 mm) amygdales are present; these could represent fragments of the quenched rims of pillows. While the rims of pillow lavas are too altered and weathered for direct comparison, the appearance and composition of amygdales is similar to that in the bodies of pillows, and it is plausible for pillow rims to include smaller vesicles than their associated pillows. Clasts are angular, many with curviplanar margins; these shapes suggest quench fragmentation processes (McPhie et al., 1993). There is no evidence for explosive eruption: no scoriaceous clasts, no matrix clasts displaying bubble-wall glass shards (McPhie et al., 1993), and no moulded or fluidal shapes that might suggest hot pyroclasts (Cousineau and Bedard, 2000). The observed features suggest that the lapilli tuff is resedimented hyaloclastite. One feeder dike was directly observed, coming to a bulbous end with fragments of dike rock surrounding it. However, the peperitic nature of contacts between the pillow lavas and the lapilli tuff, and the pillow-fragment clasts in lapilli tuff underlying pillow lavas, indicate that this hyaloclastite was formed from an earlier generation of pillow lava and dikes. These must underlie the pillow lava observed and are not (with the exception of the single feeder dike noted) seen in the section (fig. 28). This interpretation is also supported by the more enriched geochemistry of the pillow lavas, which could suggest they formed from a different batch of magma to the volcaniclastics. The vesicles in clasts of the lapilli tuff are smaller and less abundant, which could indicate that the unseen pillow lava they are

derived from had a lesser volatile content and/or formed at a greater depth than the observed pillow lavas. This initial stack of pillow lava would have been emplaced before the observed volcaniclastic rocks, and thus could have been emplaced without a pre-existing sedimentary host.

Clasts from hyaloclastite formed *in situ* may be transported and redeposited in mass flows to form deposits of great lateral and vertical extent (McPhie et al., 1993, Yamagishi, 1987, 1991). Both normal and reverse grading occurs in lapilli tuff beds, although reverse grading is more common. Beds commonly occur in sequences with one coarse-grained ungraded bed followed by three or four graded, finer-grained beds, and are 0.5-2 m thick. These bedding characteristics are consistent with the lapilli tuff having formed by mass flow processes, more specifically granular flows, which are described by McPhie et al. (1993) as occurring in normal graded, reverse graded or ungraded, centimetre- to decimetre-scale beds. Yamagishi (1987) describes similar stratified hyaloclastites as foreset-beds that grow as piles around feeder dikes and are redeposited in mass flows. Mass flows may be triggered by volcanic processes (Houghton and Landis, 1989), or by the inherent instability of the pile while lava is still intruding into it (Yamagishi, 1987).

The unusual block found in the lapilli tuff at site 28 displays lower concentrations of trace elements than every other sample, and while it displays a negative Pb anomaly like the other samples from the area it was found in, it does not exhibit any of the accompanying trace element patterns that they display. It bears larger phenocrysts and is more strongly altered than the other lapilli tuff clasts. As a block, it is also far larger than any other clast in the lapilli tuff. This suggests that it was not formed by the same hyaloclastite fragmentation process that produced the lapilli tuff it rests in, and that it was not a product of either of these vents. It could have been produced instead by some other nearby satellite vent, with a longer residence time in the magma source so it had time to grow larger crystals. Perhaps it was thrown away from its source in an explosive eruption, although it would need to be close by to reach its present position in such a way. Perhaps it was part of a deposit underlying those from the eastern vent and was caught up by its mass flows; this is the more likely explanation. In either case the presence of only one such clast is unlikely, but this could merely be due to limited outcrop extent.

The fine tuff shows some laminated beds, some that are massive, and some with cross-lamination; the latter is consistently indicative of westward flow. While there is no outcrop where a complete Bouma sequence is visible, it is reasonable to surmise that the variation present denotes a series of partial T_{a-c} Bouma sequences, and thus that the tuff was deposited as a series of turbidity currents (fig. 28).

The argillite may have formed as background sedimentation, or it may be of volcanic origin. The alteration of the rock makes it difficult to distinguish between these possibilities, although the fact that the constituent clasts include albite and augite suggests the latter is more likely (Houghton and Landis, 1989). Argillite shows clear Bouma T_{b-e} sequences (fig. 11d) indicating deposition from turbidity currents. Sequences displaying only T_{d-e} divisions suggest that many of these turbidity currents were weak and near-runout-end, but those with T_b and T_c divisions also preserved indicate that in some flows the current was stronger. Unidirectional ripple cross-lamination shows these currents flowed northwards, transverse to the turbidity currents which deposited the tuff. McPhie et al. (1993) assert that the lower massive, coarse-grained layer of the idealised Bouma sequence is commonly absent in distal settings, as it is in this argillite.

The tuff and argillite are interbedded towards the top of the tuff in several places. Elsewhere the contact appears to lack this interbedding, but as this contact is often exposed low to the ground and highly weathered, this observation is not entirely certain. The lowest argillite beds within the interbedded region are thin (~ 1 cm), and they grow progressively thicker upwards until this section passes entirely into argillite. As both units formed from turbidity currents from different directions, this interbedding could have been caused by alternating flows from their different source sites. If the volcanic centres of the Riverton section are satellite vents of a larger stratovolcano, the source of the extremely fine ash that formed the argillite could have been this main volcano. This then suggests that the main volcano sloped northwards, and therefore that its peak lay to the south of the Riverton section, and the local seafloor slope and therefore depositional dip at the western side of the section was westwards. Turbidity currents can continue to travel across extremely shallow slopes, so this does not imply anything about the distance to the main volcano. The tuff turbidite flows could have been erosive, wearing away the argillite to produce the thin argillite beds observed. McPhie et al. (1993) state that for the top massive

layer (Bouma T_e) of a turbidite to be deposited, time is needed for its mud-grade particles to settle. Thus, the successive flows that form the argillite (which display this layer) may have had time gaps between them. This supports the concept of alternating deposition of tuff and argillite turbidites, and the fact that the argillite turbidites interbedded with the tuff are less complete than the overlying ones which are solely argillite.

The tuff is inferred to comprise fines generated during hyaloclastite emplacement; little ash is produced by pillows at the initial fragmentation of hyaloclastite. Argillite could have been similarly produced at the main vent, or this vent could have undergone more explosive eruptions than its effusive satellite vents.

7.3 Volcanic Depositional Systems

The long lateral sequence along the coast of Colac Bay allows inferences to be made about the depositional systems of this submarine volcano. Such environments, with steep slopes and high supply of clastic material, commonly form sedimentary systems such as submarine fans, ramps and canyons (e.g. Orton, 1996, Gamberi, 2001, Weiß et al., 2016).

The lapilli tuff has beds that denote a series of granular flows. No flow-direction indicators were found amongst them, and beds are gently folded so any original dip is not apparent. Tuff forms a series of turbidites, and cross-laminations in the western part of the section indicate that these flowed westward. There is a zone where lapilli tuff appears in channels within tuff; the long axes of these channels also trend east-west.

An individual fan lobe forms a progradational succession (Nichols, 2009), which is consistent with the bedding patterns of the lapilli tuff and Yamagishi's (1987) assertion that stratified hyaloclastites can be emplaced as foreset-beds. The tuff turbidites could be the more distal deposit of this fan lobe. Debris flows may have fining, turbiditic tails (Brown et al., 2009), and the channels could be incised by the erosive head of the flow and later filled in by the coarse part of the next flow. The lensing of beds in the tuff around site 5 suggests that some weak channelization continued into the tuff. This is the most straightforward possibility, and the flow direction indicated by cross-lamination in the tuff and orientation of the channels are consistent with it (fig. 28a). However, the coarse-grained channel deposits are not obviously identical, in terms of particle types, to the

lapilli tuff, and there are also differences between the tuff to the west and the tuff within the channel zone.

Another possibility is that the lapilli tuff forms a large-scale channel deposit (fig. 27a), with tuff turbidites forming levees at its sides (Gamberi, 2001, Nichols, 2009). Channel deposits typically comprise coarse sands and gravels such as these, and may form graded beds (Nichols, 2009). Only partial distinct Bouma sequences are visible in the tuff, and although it is possible that this is due to obscuring by alteration and weathering, it is also possible that partial Bouma sequences is all they formed, and the latter is characteristic of levee turbidites (Nichols, 2009). The channels into the tuff could then be branches out from the main channel, forming the dendritic channel systems that sometimes occur on submarine fans (Gamberi, 2001). The flow direction of currents that deposited the tuff, away from the lapilli tuff, is consistent with this, but it is implausible for such a large channel to form very near a source. Vent positions may shift on the flanks of submarine stratovolcanoes (Orton, 1996), but it is unlikely that such a shift would have occurred over the relatively short timespan suggested by the intrusion of pillow lavas into unconsolidated hyaloclastite derived from a compositionally equivalent precursor. In addition, if levee deposits are from flows moving laterally away from the channel, and they flowed westwards, directly away from the pillow pile inferred to mark the vent (fig. 26), the channel cannot have originated from this vent. It could have originated instead from the main vent of the stratovolcano (already inferred from argillite cross-lamination to lie to the south). This implies that the main vent carries the same high-Pb geochemical signature as the western satellite vent; however, although magma may migrate from the main magma chamber to erupt at a satellite vent, it is unlikely for both this process and supply from small magma batches separate from the main source to occur in the same area (Davidson and de Silva, 2000).

The tuff and lapilli tuff could also be parts of separate lobes of a submarine fan (fig. 27b). This could explain the textural differences between the tuff in the channel zone and the tuff turbidites; the channel zone tuff would be part of the same lobe as the lapilli tuff, and the tuff turbidites part of a separate, adjacent/overlapping depositional system. As the tuff-depositing currents flowed directly westwards, and the lapilli tuff thus lies directly between the tuff and the inferred vent, it is difficult to see how these two separate lobes could relate to one another. While they could overlap, if the lapilli tuff-dominated lobe

directly overlies the tuff, the interpretation of two separate lobes is unsupported. The tuff could form an older, underlying lobe, but there is no evidence for this.

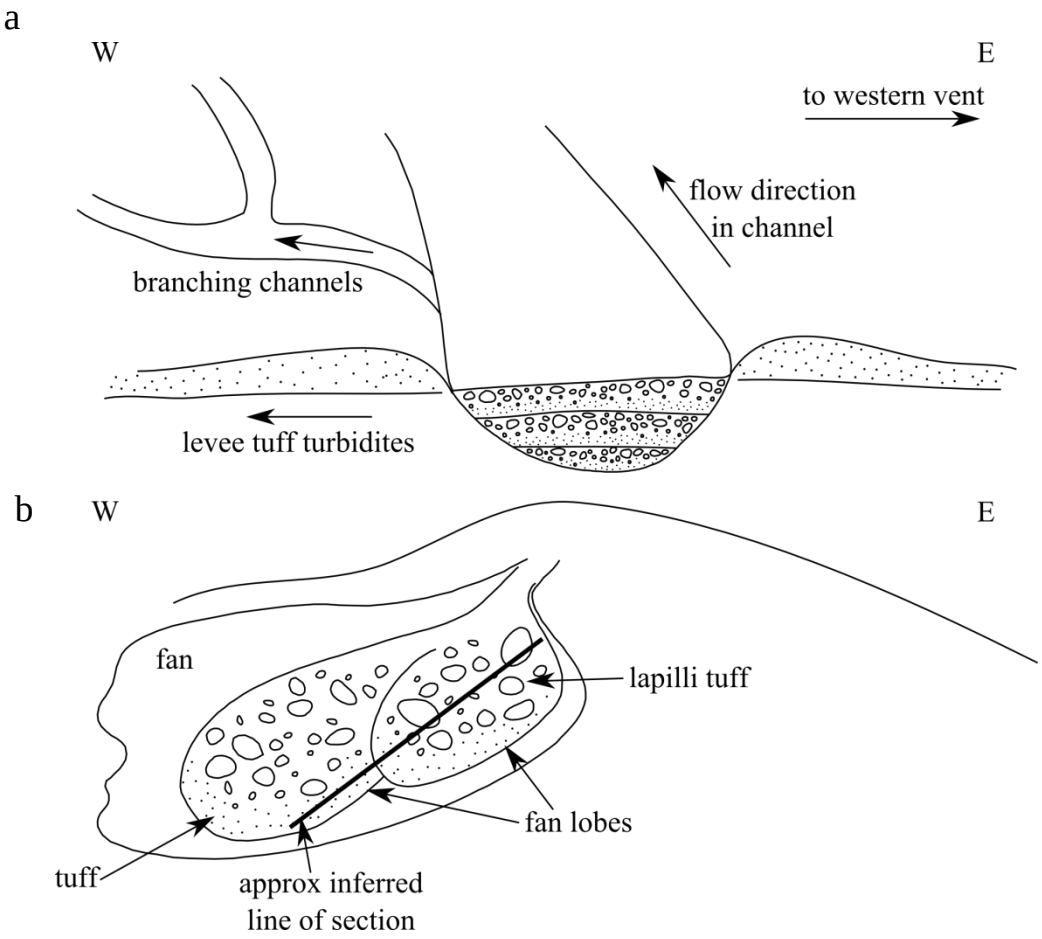

Figure 27: depositional system scenarios for the Colac Bay coast; a) large-scale lapilli tuff-filled channel with tuff turbidites forming levees; b) two overlapping submarine fan lobes.

Thus, of these possibilities, the interpretation of the western lapilli tuff-tuff sequence as deposits from a single submarine fan lobe is preferred (fig. 28). It is possible that the other areas of lapilli tuff around the western vent (those to the south of the pillow lava pile and the isolated outcrops further inland) represent partial deposits of other fan lobes, possibly from other fans (fig. 29).

There is also a layer of tuff at least 2 m thick overlying the argillite at the western end, with no interbedding. This could be a result of a shift in the depositional system, wherein the fan lobe on which tuff was accumulating shifted elsewhere leaving argillite to dominate, and later shifted back again. Such shifts are common in high-volume fan systems (Orton, 1996), and may be caused by avulsion, wherein individual lobes affect the slope of the fan surface and subsequent flows follow an altered gradient (Nichols, 2009).

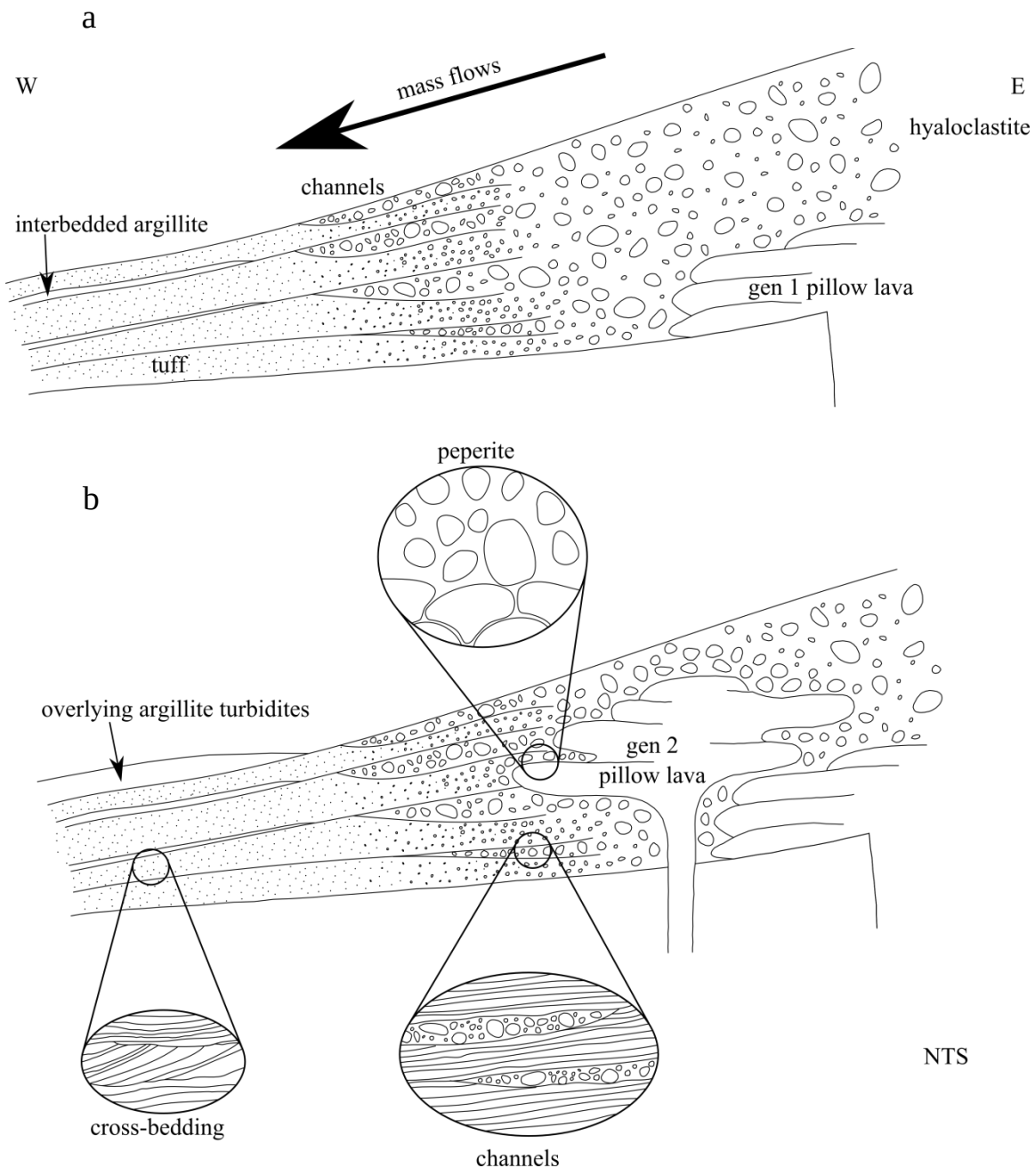

Figure 28: interpretative cross-section along Colac Bay, showing a proposed structure and sequence of events for deposits of the western vent: a) an initial generation of pillow lava forms hyaloclastite which is redeposited in a submarine fan lobe by a series of channel-forming mass flows; b) a second (observed) generation of pillow lava intrudes these deposits to form peperite. Lapilli tuff is bedded, but as the relationship of the bedding to the channel deposits is uncertain this bedding is not shown on the diagram.

The area from Howells Point northwards along the Riverton Peninsula is more difficult to interpret, especially in the absence of any flow-direction indicators from that side of the section. The volcanics in this area are interpreted to have originated from a separate vent to those along the Colac Bay coast, and have a different chemical composition (section 7.1). Here, lapilli tuff is interspersed with pillow lava, and in one extensive yet isolated outcrop tuff is interbedded with and passes upward into argillite. The lapilli tuff at this side has indistinct to nonexistent bedding from site 24 to site 27, is moderately well-bedded with beds 0.5-2 m thick at sites 28-29, and well-bedded with beds 0.3-2.5 m thick at sites 21 to 23.

Primary volcanic facies control the distribution of other facies in volcanic flank systems such as this (Gamberi, 2001). If the approximate placement of vents suggested in Figure 26 is correct, these resedimented volcaniclastic deposits were likely emplaced by flows from the eastern vent towards the western vent. Their path would thus have been influenced by the pillow lava and hyaloclastite pile forming at the vent. The precise location of the eastern vent is unknown, but pillow lavas do not extend far from their source vents (White et al., 2015), so it must be sufficiently nearby for pillow lavas from it to reach the observed section.

The two areas of lapilli tuff could represent two separate fan lobes, with their flow paths branching to travel around the topography formed by the other vent. In this case, the tuff could be the mingled deposits of fine material from the sides of these lobes. However, there is no evidence that this tuff has components from different sources, and this scenario does not account for the variation in lapilli tuff bedforms, specifically the absence of clear bedding in certain places.

Alternatively, Gamberi (2001) describes a process where a single gravity flow separates downstream, resulting in channels with longitudinal banks between them. Such banks are characterised by fine sediment; it is plausible that this arrangement could account for the relationships observed.

Channelised deposits may be massive or have indistinct bedding (Nichols, 2009), whereas fan lobes are more commonly bedded as described above. Thus, I interpret that the well-bedded portion of this area of coastline represents fan lobes from the eastern volcano, and the poorly bedded lapilli tuff and bedded tuff between them comprise a branching channel system (fig. 29).

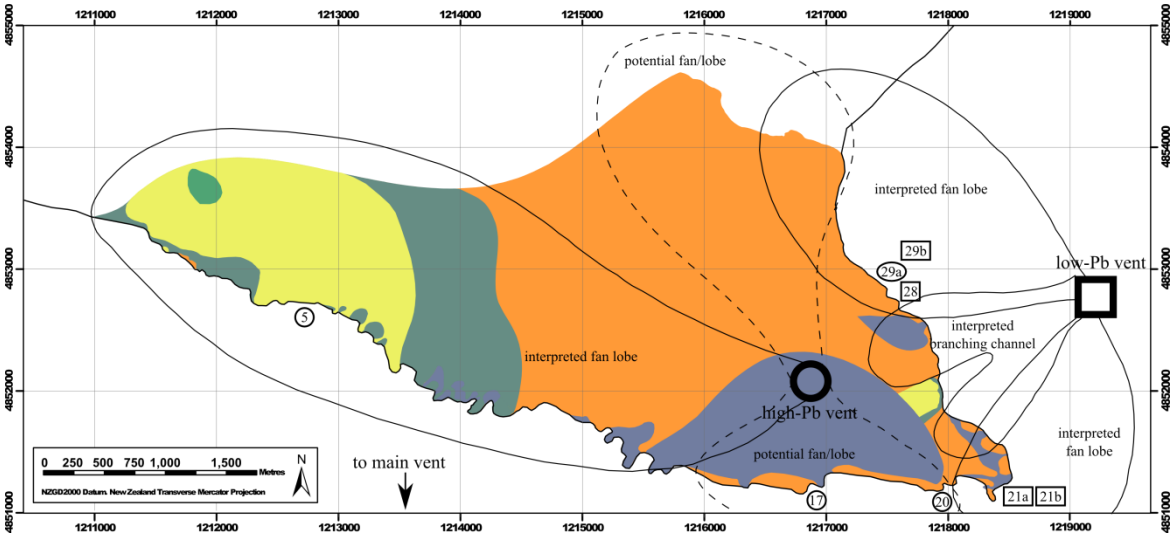

Figure 29: map showing interpretations of volcanic depositional systems. Interpreted fan lobes and branching channel indicate positions supported by geology, as discussed above. Potential fans or lobes indicate more approximately positions where these could have flowed, but which have little concrete support. Argillite is derived from the main vent; the lobes marked here refer to the tuff and lapilli tuff.

8. Conclusions

This lateral section provides a rare and valuable view of the small-scale variations and processes occurring simultaneously in a shallow submarine oceanic arc stratovolcano. Lithofacies and geochemical evidence suggest the presence of two small volcanic centres within the section. Their contrasting geochemical signatures suggest that the two vents tap different mantle domains within a transitional zone between the arc and back-arc. Their close proximity and small size renders them likely to be satellite vents on the flanks of a larger stratovolcano. Variation in geochemical characteristics indicates that the magmas underwent fractional crystallisation in their two separate source regions before erupting.

The lapilli tuff exposed is interpreted to be hyaloclastite, redeposited by a series of granular flows. It is inferred to have been produced by an earlier generation of pillow lavas and feeder dikes, not observed in this section. The fine tuff and argillite were both formed from series of turbidity currents, with alternating flows in different directions; the argillite derived from the main volcano, the tuff turbidites from the satellite vents.

At the western side of the section, the tuff turbidites and lapilli tuff granular flow deposits along the coast are interpreted as deposits of a single lobe of a fan system. Other lapilli tuff areas which do not lie along this axis could be parts of other lobes. This area of the depositional system shifted at least twice, resulting in the sequence of argillite beds underlain and overlain by tuff.

At the eastern side of the section, lapilli tuff forms two lobes, with a wide angle between them, and a channel system. The channel runs between the lobes (probably incised into them), and separates to form a longitudinal bank on which interbedded tuff and argillite are deposited. This system was likely influenced by the topography of the western vent. The dike from the western vent which intrudes the eastern deposits indicates that the two were contemporaneous. The two may have influenced each other, though the eastward-flowing deposits of the western vent are not discernible.

This, then, was the overall sequence of events. Feeder dikes and pillow lava piles from two small vents on the relatively deep-water flanks of a submarine island arc stratovolcano produced hyaloclastite, which was resedimented in systems of fans and channels. Simultaneously, argillite in turbidity currents from the volcano’s main vent

entered the area, and this series of flows alternated with tuff turbidites from the satellite vents. While these deposits were still unconsolidated, new pillow lavas and dikes emerged from both vents, intruding the volcaniclastics to produce peperites.

9. References

- Allen, S.R., Hayward, B.W., and Mathews, E. (2007). A facies model for a submarine volcaniclastic apron: the Miocene Manukau Subgroup, New Zealand. *Geological Society of America Bulletin*, 119, 725–742.
- Andrews, B. (2003). Eruptive and Depositional Mechanisms of an Eocene Shallow Submarine Volcano, Moeraki Peninsula, New Zealand. In J.D.L. White, J.L. Smellie, and D.A. Clague (Eds.), *Explosive Subaqueous Volcanism* (pp 179-188). Washington DC: American Geophysical Union.
- Bédard, J.H. (2014). Parameterizations of calcic clinopyroxene – Melt trace element partition coefficients. *Geochemistry Geophysics Geosystems*, 15(2), 303-336.
- Bradshaw, J.D. (1994). Brook Street and Murihiku terranes of New Zealand in the context of a mobile South Pacific Gondwana margin. *Journal of South American Earth Sciences*, 7(3), 325-332.
- Brown, D.J., Holohan, E.P., and Bell, B.R. (2009). Sedimentary and volcano-tectonic processes in the British Paleocene Igneous Province: a review. *Geological Magazine*, 146(3), 326-352.
- Caroff, M., Maury, R.C., Cotten, J., and Clément, J.-P. (2000). Segregation structures in vapour-differentiated basaltic flows. *Bulletin of Volcanology*, 62, 171-187.
- Cas, R.A.F. (1992). Submarine Volcanism Eruption Styles, Products, and Relevance to Understanding the Host-Rock Successions to Volcanic-Hosted Massive Sulfide Deposits. *Economic Geology*, 87, 511-541.
- Cousineau, P.A., and Bédard, J.H. (2000). Sedimentation in a subaqueous arc/back-arc setting: the Bobby Cove Formation, Snooks Arms Group, Newfoundland. *Precambrian Research*, 101, 111-134.
- Davidson, J., and De Silva, S. (2000). Composite volcanoes. In Sigurdursson, H., Houghton, B., Rymer, H., Stix, J., and McNutt, S. (Eds.), *Encyclopedia of Volcanoes* (1st ed., pp 663-681). London, England: Academic Press.
- De Silva, S.L., and Lindsay, J.M. (2015). Primary volcanic landforms. In Sigurdsson, H., Houghton, B.F., Rymer, H., Stix, J., and McNutt, S. (Eds.) *Encyclopedia of Volcanoes* (pp 274-295). New York, NY: Academic Press.

- Dickinson, W.R. (1970). Interpreting detrital modes of greywacke and arkose. *Journal of Sedimentary Petrology*, 40, 695-707.
- Doucet, P., Mueller, W., and Chartrand, F. (1994). Archean, deepwater, volcanic eruptive products associated with the Coniagas massive deposit, Quebec, Canada. *Canadian Journal of Earth Sciences*, 31, 1569–1584.
- Doyle, M.G. (2000). Clast shape and textural associations in peperite as a guide to hydromagmatic interactions: Upper Permian basaltic and basaltic andesite examples from Kiama, Australia. *Australian Journal of Earth Sciences*, 47, 167-177.
- Duraiswami, R.A., Inamdar, M.M., and Shaikh, T.N. (2013). Emplacement of pillow lavas from the ~ 2.8 Ga Chitradurga Greenstone Belt, South India: A physical volcanological, morphometric and geochemical perspective. *Journal of Volcanology and Geothermal Research*, 264, 134-149.
- Ewart, A., Collerson, K.D., Regelous, M., Wendt, J.I., and Niu, Y. (1998). Geochemical Evolution within the Tonga–Kermadec–Lau Arc–Back-arc Systems: the Role of Varying Mantle Wedge Composition in Space and Time. *Journal of Petrology*, 39(3), 331-368.
- Faure, G. (2001). *Origin of Igneous Rocks: The Isotopic Evidence*. Berlin: Springer-Verlag.
- Gamberi, F. (2001). Volcanic facies associations in a modern volcaniclastic apron (Lipari and Vulcano offshore, Aeolian Island Arc). *Bulletin of Volcanology*, 63, 264-273.
- Garrison, R.E. (1972). Inter- and Intrapillow Limestones of the Olympic Peninsula, Washington. *The Journal of Geology*, 80(3), 310-322.
- Haston, R.B., Luyendyk, B.P., Landis, C.A., and Coombs, D.S. (1989). Paleomagnetism and question of original location of the Permian Brook Street Terrane, New Zealand. *Tectonics*, 8, 791–801.
- Hekinian, R., Pineau, F., Shilobreeva, S., Bideau, D., Gracia, E., and Javoy, M. (2000). Deep sea explosive activity on the Mid-Atlantic Ridge near 34°50’ N: Magma composition, vesicularity and volatile content. *Journal of Volcanology and Geothermal Research*, 98, 49-77.
- Houghton, B.F., and Landis, C.A. (1989). Sedimentation and volcanism in a Permian arc-related basin, southern New Zealand. *Bulletin of Volcanology*, 51, 433-450.

- Jones, J.G. (1969). Pillow lavas as depth indicators. *American Journal of Science*, 267, 181-195.
- Kano, K., Yamamoto, T., and Takeuchi, K. (1993). A Miocene island-arc volcanic seamount: the Takashibiyama Formation, Shimane Peninsula, SW Japan. *Journal of Volcanology and Geothermal Research*, 59, 101-119.
- Kralj, P. (2012). Facies architecture of the Upper Oligocene submarine Smrekovec stratovolcano, Northern Slovenia. *Journal of Volcanology and Geothermal Research*, 247-248, 122-138.
- Manville, V., Nemeth, K., and Kano, K. (2009). Source to sink: a review of three decades of progress in the understanding of volcaniclastic processes, deposits, and hazards. *Sedimentary Geology*, 220, 136–161.
- Maurice, A.E., Basta, F.F., and Khiamy, A.A. (2012). Neoproterozoic nascent island arc volcanism from the Nubian Shield of Egypt: Magma genesis and generation of continental crust in intra-oceanic arcs. *Lithos*, 132-133, 1–20.
- McPhie, J., Doyle, M., and Allen, R. (1993). *Volcanic Textures: A guide to the interpretation of textures in volcanic rocks*. Hobart, Australia: CODES Key Centre, University of Tasmania.
- Moore, A., Coogan, L.A., Costa, F., and Perfit, M.R. (2014). Primitive melt replenishment and crystal-mush disaggregation in the weeks preceding the 2005–2006 eruption 9°50’ N, EPR. *Earth and Planetary Science Letters*, 403, 15-26.
- Moore, J.G. (1975). Mechanism of Formation of Pillow Lava: Pillow lava, produced as fluid lava cools underwater, is the most abundant volcanic rock on earth, but only recently have divers observed it forming. *American Scientist*, 63(3), 269-277.
- Mortimer, N., Gans, P., Calvert, A., and Walker, N. (1999). Geology and thermochronometry of the east edge of the Median Batholith (Median Tectonic Zone): a new perspective on Permian to Cretaceous growth of New Zealand. *The Island Arc*, 8, 404-425.
- Nichols, G. (2009). *Sedimentology and Stratigraphy*. Chichester, UK: Wiley-Blackwell.
- Orton, G.J. (1996). Volcanic Environments. In H.G. Reading (Ed.), *Sedimentary Environments: Processes, Facies, and Stratigraphy* (3rd ed, pp 485-566). Oxford; Cambridge, Mass: Blackwell Science.

- Pearce, J.A., and Peate, D.W. (1995). Tectonic implications of the composition of volcanic arc magmas. *Annual Reviews in Earth and Planetary Sciences*, 23, 251–285.
- Pearce, J.A., and Stern, R.J. (2006). Origin of Back-Arc Basin Magmas: Trace Element and Isotope Perspectives. Back-Arc Spreading Systems: Geological, Biological, Chemical, and Physical Interactions, *Geophysical Monograph Series*, 166, 63-86.
- Portner, R.A., Daczo, N.R., and Dickinson, J.A. (2010). Vitriclastic lithofacies from Macquarie Island (Southern Ocean): compositional influence on abyssal eruption explosivity in a dying Miocene spreading ridge. *Bulletin of Volcanology*, 72, 165-183.
- Price, R.C., Ireland, T.R., Maas, R., and Arculus, R.J. (2006). SHRIMP ion probe zircon geochronology and Sr and Nd isotope geochemistry for southern Longwood Range and Bluff Peninsula intrusive rocks of Southland, New Zealand. *New Zealand Journal of Geology and Geophysics*, 49(3), 291-303.
- Rossel, P., Oliveros, V., Ducea, M.N., and Hernandez, L. (2015). Across and along arc geochemical variations in altered volcanic rocks: Evidence from mineral chemistry of Jurassic lavas in northern Chile, and tectonic implications. *Lithos*, 239, 97-113.
- Schipper, C.I., White, J.D.L., Nichols, A.R.L., Burgisser, A., Hellebrand, E., and Murtagh, R.M. (2012). Incipient melt segregation as preserved in subaqueous pyroclasts. *Geology*, 40(4), 355-358.
- Sivell, W., and Rankin, P. (1983). Arc-tholeiite and ultramafic cumulates, Brook Street Volcanics, west D'Urville Island, New Zealand. *New Zealand Journal of Geology and Geophysics*, 26, 239-257.
- Skilling, I.P., White, J.D.L., and McPhie, J. (2002). Peperite: a review of magma-sediment mingling. *Journal of Volcanology and Geothermal Research*, 114, 1-17.
- Spandler, C., Worden, K., Arculus, R., and Eggins, S. (2005). Igneous rocks of the Brook Street Terrane, New Zealand: Implications for Permian tectonics of eastern Gondwana and magma genesis in modern intra-oceanic volcanic arcs. *New Zealand Journal of Geology and Geophysics*, 48(1), 167-183.
- Spandler, C.J., Arculus, R.J., Eggins, S.M., Mavrogenes, J.A., Price, R.C., and Reay, A.J. (2003). Petrogenesis of the Green Hills Complex, Southland, New Zealand: magmatic differentiation and cumulate formation at the roots of a Permian island arc volcano. *Contributions to Mineralogy and Petrology*, 144, 703-721.
- Sun, S.-S. and McDonough, W.F. (1989). Chemical and isotopic systematics of oceanic basalts: implications for mantle composition and processes. In Saunders, A.D., Norry,

M.J. (Eds.), *Magmatism in Ocean Basins* (pp. 313–345). London: Geological Society Special Publication.

- Weiß, B.J., Hübscher, C., Lüdmann, T., and Serra, N. (2016). Submarine sedimentation processes in the southeastern Terceira Rift/São Miguel region (Azores). *Marine Geology*, 374, 42-58.
- Wells, G., Bryan, W.B., and Pearce, T.H. (1979). Comparative Morphology of Ancient and Modern Pillow Lavas. *The Journal of Geology*, 87(4), 427-440.
- White, J.D.L., and Houghton, B.F. (2006). Primary volcaniclastic rocks. *Geological Society of America Bulletin*, 34, 677–680.
- White, J.D.L., McPhie, J., and Soule, S.A. (2015). Submarine Lavas and Hyaloclastite. In Sigurdsson, H., Houghton, B., Rymer, H., Stix, J., McNutt, S. (Eds.), *Encyclopedia of Volcanoes* (pp. 363–375). New York, NY: Academic Press.
- White, J.D.L., Smellie, J.L., and Clague, D.A. (2003). Introduction: A Deductive Outline and Topical Overview of Subaqueous Explosive Volcanism. In White, J.D.L., Smellie, J.L., and Clague, D.A. (Eds.), *Explosive Subaqueous Volcanism*. Washington, DC: American Geophysical Union.
- Yamagishi, H. (1987). Studies on the Neogene subaqueous lavas and hyaloclastites in Southwest Hokkaido. *Report of the Geological Survey of Hokkaido No. 59*, 55-117.
- Yamagishi, H. (1991). Morphological and sedimentological characteristics of the Neogene submarine coherent lavas and hyaloclastites in Southwest Hokkaido, Japan. *Sedimentary Geology*, 74, 5-23.

Appendix A: Trace Element Data

Trace element compositions of clinopyroxenes acquired by LA-ICP-MS are presented below. Suffixes c and r denote measurements taken from the cores and rims of clinopyroxenes, respectively. Columns with headers in bold indicate samples which were not included in the averages reported in the main text.

Sample 20 (pillow lava)

	20-1	20-2	20-3	20-4	20-5	20-6	20-7	20-8
Li	1.997	1.372	1.486	2.460	2.420	2.073	2.792	2.186
Be	0.426	0.080	0.111	0.468	0.187	bdl	bdl	0.000
K	183.569	155.445	144.283	234.744	120.122	222.551	883.851	185.753
Sc	144.446	132.437	160.239	149.560	157.072	149.389	137.750	143.829
Ti	5588.797	4375.130	4330.051	5461.524	5751.780	4623.498	4702.592	5741.145
V	485.521	460.684	408.423	456.417	538.425	466.480	415.018	523.616
Cr	190.855	244.260	385.843	221.796	282.287	294.165	263.601	240.776
Mn	1444.625	1390.957	1539.230	1650.678	1515.187	1502.458	1162.560	1557.436
Co	45.477	42.126	46.355	45.988	45.100	45.268	39.511	47.036
Ni	65.964	60.263	73.738	68.861	72.067	69.057	68.346	61.178
Cu	37.866	17.700	18.979	45.009	29.829	70.584	41.332	39.597
Zn	48.736	31.273	35.953	40.111	39.018	38.743	40.985	44.429
Ga	8.990	8.027	6.866	7.353	8.345	6.630	7.890	8.000
Ge	2.347	2.474	2.555	2.420	2.763	2.802	2.346	2.835
As	0.468	0.862	0.497	0.427	bdl	bdl	0.322	0.470
Rb	1.408	1.060	1.935	2.790	1.165	1.686	2.009	1.615
Sr	25.934	40.993	14.005	18.551	20.931	14.383	61.608	24.215
Y	20.568	17.139	17.853	20.493	18.835	19.175	18.865	16.533

Zr	36.521	26.375	28.417	38.401	35.905	33.022	33.679	32.562
Nb	0.070	0.061	0.078	0.209	0.174	0.105	0.128	0.274
Cs	0.124	0.049	0.078	0.168	0.064	0.312	0.111	0.166
Ba	1.514	1.606	1.276	2.221	1.658	1.169	7.915	2.094
La	0.674	0.550	0.441	0.510	0.653	0.528	0.634	0.479
Ce	3.041	2.735	2.150	2.508	2.895	3.014	2.612	2.694
Pr	0.735	0.608	0.555	0.546	0.689	0.693	0.630	0.581
Nd	4.795	4.438	4.041	4.406	4.778	4.460	4.269	4.529
Sm	2.385	1.929	1.936	2.381	2.069	2.067	2.269	1.860
Eu	0.863	0.790	0.759	0.810	0.787	0.809	0.682	0.687
Gd	3.663	2.649	2.614	3.096	3.245	3.132	2.885	2.792
Tb	0.610	0.491	0.579	0.581	0.499	0.531	0.508	0.490
Dy	3.955	3.406	3.452	3.668	3.870	3.780	3.604	3.184
Ho	0.825	0.677	0.691	0.821	0.803	0.823	0.778	0.686
Er	2.368	1.904	2.089	2.286	2.334	2.169	2.151	1.923
Tm	0.323	0.253	0.254	0.340	0.296	0.266	0.270	0.261
Yb	2.077	1.600	1.790	1.853	1.960	2.185	1.966	1.622
Lu	0.315	0.236	0.268	0.317	0.252	0.247	0.282	0.258
Hf	1.790	1.437	1.361	1.947	1.707	1.530	1.523	1.559
Ta	0.014	0.016	0.013	0.018	0.021	0.012	0.017	0.023
Pb	0.539	0.148	0.191	0.573	0.390	0.562	0.558	0.665
Th	0.024	0.014	0.025	0.012	0.018	0.021	0.048	0.026
U	0.011	0.007	0.018	0.030	0.020	0.058	0.015	0.029

Sample 21a (pillow lava)

	21a-0	21a-1	21a-2	**21a-3**	21a-4	21a-5	21a-6	21a-7	21a-8
Li	1.141	1.627	1.809	0.924	1.232	1.095	1.284	0.893	1.063
Be	0.101	bdl	0.138	bdl	bdl	bdl	bdl	0.081	bdl
K	205.606	54.183	137.611	28.105	46.390	80.166	35.847	16.439	75.057
Sc	170.024	151.230	161.623	124.586	172.139	144.038	147.988	167.054	161.356
Ti	3398.755	3540.241	3781.384	1914.999	3638.916	3187.843	3756.854	3696.646	3885.033
V	406.132	450.475	413.691	295.626	427.411	389.779	470.956	445.975	439.135
Cr	1458.270	1124.285	1095.920	2794.049	1146.111	1046.967	893.128	1268.502	1216.441
Mn	1224.315	1318.173	1320.862	1064.537	1257.920	1239.853	1524.783	1245.809	1246.426
Co	41.871	42.968	42.551	39.144	44.223	44.843	45.747	44.607	40.769
Ni	138.272	142.174	140.604	170.821	147.788	145.661	131.471	140.089	141.053
Cu	7.452	6.880	11.137	9.293	9.674	18.673	5.818	3.622	4.571
Zn	26.143	31.652	31.371	22.931	26.389	25.217	30.950	26.344	26.367
Ga	5.831	7.090	6.686	4.981	5.926	5.758	6.475	6.047	6.874
Ge	2.319	2.596	2.544	2.885	2.412	1.973	2.832	2.772	2.232
As	bdl	bdl	0.301	bdl	bdl	0.285	bdl	bdl	0.430
Rb	0.302	0.092	0.176	0.171	0.082	0.154	0.039	0.033	0.112
Sr	19.071	14.372	25.468	13.779	15.280	20.840	12.815	14.976	17.849
Y	13.052	12.027	13.760	7.174	14.496	12.055	13.098	12.299	15.346
Zr	18.762	21.104	25.230	8.762	20.924	17.600	21.794	19.735	25.516
Nb	0.067	0.033	0.136	0.010	0.062	0.072	0.060	0.042	0.108
Cs	0.014	bdl	0.009	bdl	bdl	0.031	bdl	bdl	bdl
Ba	2.153	0.541	1.502	0.187	0.355	0.746	0.384	0.079	0.883
La	0.351	0.341	0.426	0.204	0.428	0.273	0.382	0.291	0.466
Ce	1.514	1.627	1.795	0.959	1.780	1.389	1.656	1.526	2.112
Pr	0.396	0.366	0.460	0.229	0.456	0.375	0.455	0.382	0.512
Nd	2.960	2.952	3.470	1.765	3.488	2.504	3.025	3.141	3.601
Sm	1.429	1.495	1.545	0.713	1.612	1.092	1.479	1.487	1.648

Eu	0.537	0.508	0.564	0.337	0.610	0.515	0.562	0.533	0.734
Gd	1.881	1.887	2.243	1.085	2.236	1.920	2.098	2.216	2.412
Tb	0.382	0.305	0.423	0.217	0.393	0.353	0.341	0.380	0.455
Dy	2.612	2.503	2.474	1.341	3.025	2.196	2.558	2.393	3.015
Ho	0.561	0.491	0.536	0.296	0.544	0.485	0.474	0.498	0.671
Er	1.591	1.424	1.558	0.786	1.594	1.468	1.498	1.511	1.795
Tm	0.216	0.164	0.209	0.100	0.202	0.187	0.228	0.190	0.195
Yb	1.245	1.311	1.331	0.853	1.472	1.127	1.381	1.347	1.787
Lu	0.211	0.181	0.183	0.088	0.201	0.170	0.202	0.178	0.188
Hf	1.152	1.074	1.172	0.410	1.193	0.880	0.851	1.156	1.423
Ta	0.007	0.007	0.010	0.000	0.010	0.001	0.011	0.005	0.013
Pb	0.068	0.144	0.103	0.108	0.069	0.306	0.077	0.069	0.149
Th	0.007	0.006	0.020	0.004	0.008	0.007	0.012	0.014	0.012
U	0.003	0.005	0.011	0.004	0.002	0.004	0.008	0.005	0.005

Sample 21b (dike)

	21b-1c	21b-1r	21b-2c	21b-2r	21b-4c	21b-4r	21b-5c
Li	0.884	1.002	0.900	1.317	1.483	1.075	1.427
Be	bdl	0.198	bdl	0.102	0.205	0.096	0.107
K	4.941	15.864	bdl	24.811	212.306	42.452	52.392
Sc	124.246	98.499	131.6048	132.016	124.119	128.975	138.349
Ti	3163.758	2450.703	3263.278	3474.307	3103.31	3115.477	3466.711
V	382.416	318.069	367.5308	386.200	363.6434	342.193	392.612
Cr	2169.044	2616.804	774.8164	1982.471	2411.403	2419.778	1728.407
Mn	1594.892	1568.053	1674.689	1605.196	1579.638	1499.023	1577.042
Co	45.218	45.311	46.85937	43.666	43.846	42.341	43.298
Ni	131.434	163.441	105.3177	140.780	145.084	149.753	133.131
Cu	2.819	4.011	2.868727	5.491	6.534	4.035	2.995
Zn	40.290	38.769	39.49213	40.968	50.256	41.790	45.187

Ga	5.320	4.989	5.096921	6.221	6.094	5.340	5.965
Ge	2.796	2.917	2.796434	2.754	2.845	2.769	2.913
As	bdl	bdl	bdl	bdl	0.225	0.134	Bdl
Rb	0.025	0.059	bdl	0.082	0.760	0.133	0.150
Sr	17.216	16.481	17.84384	17.767	20.088	18.624	18.723
Y	13.558	9.647	13.72891	14.693	13.543	13.855	15.693
Zr	10.417	7.391	10.42271	13.236	11.356	10.867	14.489
Nb	0.011	0.021	0.007627	0.023	0.046	0.013	0.020
Cs	bdl	0.007	bdl	0.024	0.059	0.021	0.033
Ba	0.013	0.278	0.013857	0.220	1.373	0.143	0.157
La	0.327	0.255	0.322909	0.372	0.345	0.344	0.441
Ce	1.802	1.429	1.636727	1.803	1.769	1.599	2.140
Pr	0.452	0.341	0.440714	0.448	0.422	0.411	0.521
Nd	3.295	2.532	3.215578	3.440	3.276	3.258	4.067
Sm	1.532	1.223	1.535423	1.621	1.465	1.527	1.862
Eu	0.602	0.415	0.548461	0.597	0.539	0.530	0.628
Gd	2.265	1.457	2.25348	2.439	2.326	2.263	2.636
Tb	0.406	0.266	0.380915	0.407	0.373	0.395	0.459
Dy	2.846	1.872	2.805732	2.888	2.708	2.685	3.150
Ho	0.537	0.398	0.577399	0.595	0.552	0.545	0.649
Er	1.687	1.126	1.645036	1.732	1.561	1.555	1.796
Tm	0.206	0.147	0.214149	0.221	0.208	0.213	0.244
Yb	1.376	0.944	1.444165	1.588	1.399	1.365	1.564
Lu	0.202	0.144	0.194176	0.227	0.195	0.193	0.237
Hf	0.616	0.390	0.554819	0.705	0.608	0.585	0.770
Ta	0.003	0.002	0.001493	0.004	0.002	0.002	0.001
Pb	0.033	0.159	0.088172	0.356	0.223	0.095	0.048
Th	0.002	0.003	bdl	0.003	0.004	0.003	0.008
U	0.001	0.001	0.000821	0.003	0.002	0.001	0.003

Sample 29a (dike)

	29a-1c	29a-1r	29a-2c	29a-2r	29a-3c	29a-3r	29a-4c	29a-4r	**29a-5c**	**29a-5r**
Li	0.998	0.983	1.066	0.980	1.147	1.060	1.048	1.157	1.484	1.014
Be	bdl	0.063	0.019	bdl	bdl	0.111	0.018	0.118	0.121	0.086
K	2.564	10.865	1.568	bdl	12.900	95.873	2.087	17.926	7.642	1.513
Sc	101.469	107.071	98.323	119.605	124.259	123.5467	101.317	113.176	156.929	143.233
Ti	2493.889	2783.276	2309.810	3139.347	3131.114	3252.514	2447.973	2756.849	4610.819	4406.803
V	310.855	325.199	277.867	331.699	359.881	336.242	302.087	288.237	439.222	436.031
Cr	1125.852	1662.930	1338.329	1868.525	2280.256	1763.351	1548.915	1242.837	350.026	818.970
Mn	1625.077	1418.405	1543.794	1418.099	1541.497	1344.674	1549.405	1371.788	1890.361	1665.79
Co	41.995	39.519	41.511	38.501	39.572	38.827	40.417	37.810	43.671	39.991
Ni	149.013	170.617	169.727	177.628	174.192	168.938	171.531	165.972	124.059	135.557
Cu	3.806	4.871	3.694	2.965	21.886	23.741	3.268	5.101	7.122	3.986
Zn	38.107	35.097	37.463	33.440	48.076	54.198	34.911	33.424	47.787	38.090
Ga	4.266	4.959	3.859	5.246	5.634	5.437	4.317	4.328	6.291	6.763
Ge	3.086	2.895	2.844	3.084	3.151	3.130	3.235	2.839	3.082	2.846
As	bdl	0.159	bdl	bdl	0.220	0.230	0.107	0.094	bdl	0.100
Rb	bdl	0.028	bdl	bdl	0.041	0.104	bdl	0.043	0.018	bdl
Sr	30.535	32.154	25.668	31.148	30.911	32.829	26.177	33.392	25.805	29.222
Y	11.029	12.097	10.320	13.194	13.959	14.515	10.661	12.318	24.845	18.435
Zr	8.100	10.416	6.818	11.884	12.557	13.077	8.251	9.854	27.968	19.822
Nb	0.004	0.011	bdl	0.005	0.011	0.009	0.003	0.012	0.024	0.011
Cs	bdl	bdl	bdl	bdl	bdl	0.003	bdl	bdl	bdl	bdl
Ba	0.015	0.133	bdl	0.013	0.263	0.351	0.012	0.147	0.083	0.021
La	0.299	0.388	0.283	0.367	0.383	0.417	0.312	0.358	0.640	0.503
Ce	1.699	2.084	1.655	2.080	2.226	2.247	1.845	1.710	3.060	2.769
Pr	0.425	0.521	0.417	0.505	0.552	0.562	0.443	0.449	0.768	0.712
Nd	2.943	3.120	2.743	3.527	3.467	3.694	2.830	3.100	5.827	4.625
Sm	1.276	1.403	1.167	1.555	1.598	1.664	1.173	1.342	2.726	2.035

Eu	0.488	0.471	0.429	0.568	0.626	0.661	0.515	0.489	0.913	0.773
Gd	1.985	2.082	1.794	2.291	2.420	2.443	1.869	2.196	4.034	2.964
Tb	0.329	0.343	0.307	0.397	0.371	0.415	0.329	0.357	0.681	0.537
Dy	2.273	2.466	2.174	2.713	2.789	2.830	2.101	2.397	5.158	3.757
Ho	0.448	0.477	0.431	0.536	0.556	0.591	0.430	0.484	1.038	0.781
Er	1.247	1.346	1.322	1.544	1.592	1.606	1.197	1.517	2.861	2.118
Tm	0.178	0.193	0.162	0.189	0.217	0.212	0.153	0.196	0.378	0.278
Yb	1.070	1.193	1.084	1.336	1.336	1.428	1.109	1.172	2.510	1.831
Lu	0.170	0.162	0.146	0.183	0.194	0.205	0.143	0.192	0.335	0.265
Hf	0.424	0.547	0.417	0.630	0.683	0.748	0.455	0.512	1.513	1.070
Ta	0.0004	0.001	0.0004	0.001	0.001	0.0008	0.0003	0.0007	0.007	0.004
Pb	0.032	0.111	0.110	0.034	2.209	2.695	0.027	0.063	0.502	0.126
Th	0.005	0.002	bdl	0.003	0.003	0.003	0.001	0.002	0.004	0.004
U	bdl	0.000	0.000	0	0.001	0.0007	0.000	0	0.001	0.001

Sample 17 (lapilli tuff)

	17-1c	17-1r	17-2c	17-2r	17-3c	17-3r	17-4c	17-4r	17-5c	17-5r
Li	0.483	0.429	0.517	0.522	0.908	0.656	0.465	0.908	1.051	0.656
Be	bdl	bdl	0.079	bdl	0.055	0.074	0.133	0.239	0.231	0.246
K	0.922	0.969	3.328	3.139	15.775	26.982	1.578	20.914	29.474	10.291
Sc	94.426	85.298	104.869	98.630	103.533	111.350	108.905	129.911	117.066	140.303
Ti	1225.235	1299.743	1537.455	1315.698	1492.609	1422.710	1568.551	1847.558	1620.278	1734.398
V	178.089	203.766	230.959	193.784	230.488	225.455	232.660	254.270	250.988	256.471
Cr	4086.161	4768.940	2658.916	1996.333	2860.875	2382.922	2846.147	2398.457	2684.220	2527.434
Mn	820.681	858.389	928.488	936.210	952.208	978.818	917.998	1069.582	1068.921	1000.082
Co	33.727	35.654	36.251	36.208	36.876	37.183	35.804	39.129	40.417	36.435
Ni	216.375	205.214	181.358	181.754	184.541	183.758	178.457	182.680	173.927	172.452
Cu	2.023	2.307	1.849	1.977	4.197	2.154	3.176	4.543	4.643	2.430
Zn	16.313	19.135	19.385	19.795	22.405	21.119	19.971	24.869	27.709	22.071

Ga	2.489	3.080	3.188	2.614	3.486	2.994	3.414	3.911	3.925	3.800
Ge	2.325	1.879	2.616	2.445	2.664	2.319	2.600	2.416	2.618	2.323
As	bdl	bdl	bdl	bdl	bdl	0.215	0.124	0.213	0.115	bdl
Rb	bdl	bdl	bdl	0.008	0.090	0.021	bdl	0.062	0.063	0.034
Sr	13.626	13.099	12.971	12.356	13.583	12.471	13.381	13.157	13.871	14.032
Y	4.677	4.349	5.802	4.982	5.419	6.042	5.979	7.400	6.206	7.256
Zr	2.860	3.001	4.582	3.834	5.209	5.396	4.761	8.005	7.332	8.278
Nb	0.006	0.007	0.006	0.009	0.051	0.009	0.004	0.047	0.078	0.014
Cs	bdl	bdl	bdl	bdl	bdl	bdl	bdl	0.006	0.004	0.004
Ba	0.005	0.019	0.049	0.031	0.440	0.181	0.041	0.437	0.466	0.099
La	0.118	0.110	0.133	0.113	0.244	0.133	0.149	0.189	0.182	0.176
Ce	0.591	0.635	0.705	0.598	0.779	0.749	0.727	0.889	0.857	0.910
Pr	0.162	0.160	0.184	0.154	0.194	0.192	0.178	0.227	0.198	0.219
Nd	1.162	1.086	1.396	1.125	1.345	1.381	1.425	1.693	1.456	1.715
Sm	0.619	0.533	0.658	0.552	0.619	0.652	0.771	0.854	0.726	0.868
Eu	0.202	0.193	0.251	0.213	0.255	0.246	0.268	0.302	0.267	0.309
Gd	0.794	0.757	1.018	0.875	0.906	1.003	1.018	1.249	1.000	1.243
Tb	0.144	0.123	0.167	0.146	0.163	0.169	0.162	0.210	0.174	0.210
Dy	0.942	0.884	1.145	1.033	1.094	1.241	1.295	1.499	1.231	1.492
Ho	0.194	0.190	0.238	0.204	0.219	0.236	0.245	0.311	0.261	0.300
Er	0.535	0.494	0.687	0.601	0.652	0.691	0.671	0.861	0.727	0.862
Tm	0.070	0.073	0.090	0.073	0.082	0.100	0.093	0.120	0.098	0.107
Yb	0.461	0.419	0.585	0.505	0.557	0.657	0.617	0.727	0.606	0.764
Lu	0.068	0.061	0.083	0.076	0.083	0.093	0.077	0.107	0.096	0.118
Hf	0.180	0.186	0.252	0.190	0.250	0.297	0.259	0.437	0.383	0.437
Ta	0.001	0.001	0.0003	0.0001	0.003	0.001	0.001	0.005	0.006	0.001
Pb	0.036	0.094	0.138	0.097	0.673	0.152	0.098	0.981	0.787	0.182
Th	0.000	0.001	0.001	0.005	0.008	0.008	0.001	0.008	0.008	0.012
U	0.0001	0.0003	0.0004	0.0004	0.003	0.001	0.0002	0.002	0.003	0.001

Sample 28 (unusual clast in lapilli tuff)

	28-1c	28-1r	28-2c	28-2r	28-3c	28-3r	**28-4c**	28-4r	28-5c	28-5r
Li	0.667	0.946	0.616	0.968	0.829	0.948	0.876	0.945	0.806	0.950
Be	bdl	0.040	bdl	bdl	0.000	0.075	0.033	0.017	0.009	bdl
K	1.670	2.896	bdl	4.805	bdl	67.144	10.967	4.301	10.248	1.994
Sc	88.307	112.598	103.307	118.834	69.615	96.549	128.502	109.766	73.153	132.244
Ti	1537.772	2551.739	1762.686	2278.818	821.160	1709.776	3098.318	2108.794	934.744	2480.797
V	201.805	419.510	196.600	367.001	117.802	295.452	444.875	339.656	133.173	426.140
Cr	2124.676	1632.539	1909.420	2290.769	4030.572	1802.359	1076.296	2403.279	3642.774	2916.733
Mn	905.602	1541.264	868.397	1513.437	766.153	1620.398	1674.306	1485.610	834.336	1379.266
Co	33.003	44.778	34.910	39.172	32.316	41.397	44.587	39.576	31.657	39.739
Ni	137.929	160.650	195.584	131.514	185.620	136.729	155.793	138.490	173.894	130.405
Cu	3.365	3.096	1.520	3.223	2.023	6.254	3.812	6.379	2.855	2.861
Zn	17.997	36.916	16.573	32.149	13.897	35.828	39.318	32.746	15.792	30.463
Ga	2.643	5.003	2.840	4.503	1.485	3.468	4.851	4.241	1.905	4.995
Ge	2.540	2.902	2.283	2.891	2.511	2.813	2.810	2.842	2.417	3.158
As	bdl	0.124	bdl	0.152	0.075	0.383	0.111	0.104	bdl	bdl
Rb	0.010	0.016	bdl	0.017	bdl	0.149	0.020	0.017	0.085	bdl
Sr	12.831	14.856	14.254	14.949	9.344	12.612	15.837	13.975	16.247	15.224
Y	4.819	10.945	5.364	10.396	2.631	7.786	14.254	8.851	2.950	9.748
Zr	2.765	7.316	3.368	15.515	0.992	4.689	9.542	5.782	1.247	8.289
Nb	0.003	0.006	0.003	0.008	bdl	0.007	0.029	0.015	0.005	0.007
Cs	bdl	bdl	0.003	0.005	bdl	0.015	0.003	0.017	0.003	0.002
Ba	0.017	0.018	0.015	0.072	0.034	0.826	0.157	0.110	0.054	bdl
La	0.100	0.244	0.125	0.303	0.047	0.165	0.282	0.189	0.078	0.243
Ce	0.524	1.426	0.571	1.262	0.226	0.899	1.482	1.081	0.393	1.398
Pr	0.141	0.347	0.166	0.299	0.068	0.232	0.386	0.274	0.103	0.340
Nd	1.102	2.466	1.094	2.289	0.483	1.661	2.999	2.011	0.774	2.465
Sm	0.542	1.165	0.559	1.054	0.252	0.821	1.416	0.979	0.353	1.143

Eu	0.222	0.450	0.227	0.369	0.113	0.309	0.508	0.353	0.128	0.424
Gd	0.816	1.778	0.871	1.622	0.458	1.171	2.234	1.419	0.498	1.645
Tb	0.144	0.312	0.155	0.274	0.068	0.218	0.388	0.245	0.093	0.277
Dy	0.988	2.219	1.103	1.887	0.563	1.515	2.788	1.772	0.640	2.025
Ho	0.201	0.460	0.208	0.408	0.098	0.312	0.555	0.353	0.114	0.411
Er	0.576	1.267	0.626	1.258	0.296	0.934	1.601	1.017	0.341	1.152
Tm	0.069	0.171	0.078	0.173	0.041	0.112	0.221	0.130	0.046	0.156
Yb	0.476	1.099	0.461	1.343	0.242	0.828	1.441	0.892	0.294	1.006
Lu	0.063	0.158	0.071	0.214	0.040	0.126	0.202	0.129	0.044	0.137
Hf	0.164	0.389	0.220	0.601	0.053	0.224	0.495	0.309	0.082	0.551
Ta	0.0001	0.001	0.000	0.0005	0.000	0.001	0.001	0.001	0.000	0.001
Pb	0.038	0.070	0.017	0.064	0.012	0.053	0.060	0.067	0.035	0.025
Th	0.000	0.001	0.0004	0.003	0.0002	0.000	0.003	bdl	0.000	0.001
U	0.001	0.001	0.0002	0.003	0.000	0.001	0.002	0.001	0.0001	0.0003

Sample 29b (clast in lapilli tuff)

	29b-1c	29b-1r	29b-2c	29b-2r	29b-3c	**29b-3r**	29b-4c	29b-4r	29b-5c	29b-5r
Li	0.576	0.890	0.878	0.641	0.770	1.023	0.670	0.683	0.757	0.713
Be	bdl	bdl	bdl	bdl	bdl	0.286	0.018	bdl	0.094	0.057
K	12.818	22.109	45.114	bdl	19.141	60.600	2.444	13.423	13.617	6.870
Sc	80.315	114.338	104.261	99.999	131.080	139.646	115.156	108.955	102.230	104.346
Ti	1192.300	1889.117	1964.924	1853.877	2304.064	2601.549	2142.933	2059.298	1786.376	1898.324
V	195.219	273.095	316.871	273.168	314.731	388.307	304.233	304.520	277.153	275.438
Cr	4378.537	1220.417	993.274	1598.914	1427.119	756.370	1657.579	1718.418	1036.431	926.411
Mn	795.082	1258.857	1382.190	1121.536	1152.544	1479.239	1171.880	1173.738	1300.615	1187.255
Co	33.333	40.906	43.655	38.760	38.810	40.610	39.842	39.732	41.926	40.162
Ni	194.750	118.915	118.410	126.252	115.117	99.250	119.952	119.961	119.238	116.476
Cu	3.400	6.818	8.964	2.020	8.924	29.230	2.816	5.839	5.955	3.527
Zn	16.410	27.685	30.152	23.935	25.445	34.057	25.521	25.845	28.294	25.944

Ga	2.764	2.920	3.598	3.239	3.713	4.616	3.750	3.961	3.122	3.163
Ge	2.425	2.714	3.158	2.536	2.931	2.746	2.787	2.798	2.742	2.789
As	0.226	0.383	0.176	bdl	0.238	0.502	0.146	0.183	0.140	0.226
Rb	0.143	0.167	0.481	bdl	0.167	0.399	0.019	0.086	0.111	0.090
Sr	13.823	13.930	14.243	14.801	16.286	16.706	15.391	14.969	13.201	14.610
Y	3.778	8.284	8.073	6.924	9.727	12.473	8.486	7.824	7.630	7.454
Zr	2.727	6.207	5.285	4.442	7.238	13.665	5.917	5.891	4.669	4.815
Nb	0.006	0.005	0.009	0.007	0.007	0.009	0.005	0.005	0.005	0.004
Cs	0.004	0.006	0.010	bdl	0.010	0.019	bdl	bdl	bdl	bdl
Ba	0.034	0.095	0.143	0.013	0.068	0.302	0.004	0.031	0.069	0.027
La	0.096	0.178	0.179	0.158	0.231	0.355	0.197	0.194	0.164	0.172
Ce	0.588	0.970	1.004	0.930	1.123	1.498	1.089	1.052	0.905	0.945
Pr	0.138	0.252	0.255	0.237	0.315	0.394	0.278	0.266	0.235	0.247
Nd	1.038	1.954	1.869	1.649	2.325	2.946	2.147	1.931	1.742	1.877
Sm	0.462	0.906	0.906	0.817	1.116	1.355	0.947	0.867	0.821	0.861
Eu	0.195	0.346	0.336	0.317	0.380	0.510	0.367	0.344	0.315	0.325
Gd	0.653	1.405	1.320	1.190	1.621	2.016	1.413	1.260	1.276	1.240
Tb	0.109	0.240	0.239	0.208	0.280	0.335	0.246	0.236	0.223	0.206
Dy	0.795	1.632	1.617	1.435	1.928	2.371	1.752	1.578	1.550	1.464
Ho	0.164	0.333	0.328	0.268	0.387	0.503	0.352	0.319	0.305	0.304
Er	0.439	0.910	0.911	0.776	1.137	1.446	0.938	0.898	0.868	0.828
Tm	0.056	0.129	0.129	0.103	0.147	0.187	0.121	0.124	0.117	0.117
Yb	0.389	0.828	0.820	0.655	0.950	1.231	0.772	0.803	0.793	0.743
Lu	0.055	0.122	0.111	0.097	0.126	0.181	0.128	0.109	0.105	0.113
Hf	0.146	0.321	0.301	0.252	0.394	0.662	0.335	0.331	0.244	0.227
Ta	bdl	0.001	0.001	0.0003	0.0004	0.001	0.001	0.000	0.000	0.001
Pb	0.019	0.058	0.047	0.020	0.077	0.161	0.032	0.029	0.042	0.034
Th	bdl	0.002	0.001	0.001	0.002	0.012	0.001	0.0004	0.001	0.001
U	0.003	0.006	0.003	0.000	0.001	0.002	0.000	0.001	0.0001	0.0001

Sample 5 (tuff)

	5-1c	5-1r	5-2c	5-2r	5-3c	5-4c	**5-4r**	5-5r
Li	0.988	1.274	0.915	0.945	0.673	0.736	3.346	0.885
Be	0.140	0.084	0.170	0.112	bdl	0.038	0.245	0.151
K	7.726	28.798	1.831	112.315	1.334	3.481	199.252	8.515
Sc	120.612	119.877	99.739	125.276	109.827	114.332	128.843	105.860
Ti	2145.748	2171.636	1807.064	2354.184	2036.344	1827.404	3285.005	1712.142
V	280.483	255.162	214.683	256.587	210.856	257.368	310.285	223.102
Cr	1624.046	1228.987	2837.805	1651.645	2783.208	2108.336	1303.334	2006.298
Mn	1173.541	1198.685	934.917	1337.870	846.232	1083.252	1530.343	1102.932
Co	38.604	38.323	33.926	38.301	31.770	38.257	43.311	37.011
Ni	172.150	165.340	192.888	170.298	199.883	163.855	120.416	181.404
Cu	10.016	11.264	3.289	32.947	4.807	7.124	47.183	19.530
Zn	30.002	32.508	19.348	51.342	20.046	24.963	85.360	31.611
Ga	3.617	3.161	3.291	3.359	3.319	3.496	5.100	2.896
Ge	2.587	2.051	2.683	2.588	2.565	2.785	2.266	2.501
As	0.243	bdl	bdl	bdl	bdl	0.218	0.254	bdl
Rb	0.033	0.291	0.009	0.040	bdl	0.022	0.131	0.017
Sr	16.250	15.855	17.780	18.053	17.390	14.120	23.731	16.954
Y	8.810	8.283	6.228	8.022	6.930	7.234	10.866	7.039
Zr	9.429	9.575	5.551	22.600	7.064	5.390	36.949	6.906
Nb	0.018	0.051	0.006	0.114	0.009	0.007	0.372	0.012
Cs	0.036	0.027	0.011	0.050	bdl	0.017	0.076	0.015
Ba	0.212	0.339	0.095	0.518	0.071	0.119	7.775	0.163
La	0.266	0.231	0.223	0.284	0.216	0.157	0.472	0.222
Ce	1.219	1.081	0.870	1.216	0.965	0.777	1.743	0.896
Pr	0.296	0.265	0.233	0.271	0.251	0.211	0.348	0.226
Nd	2.104	1.906	1.693	1.906	1.719	1.590	2.440	1.600
Sm	1.105	0.954	0.708	0.977	0.871	0.764	1.140	0.741

Eu	0.344	0.333	0.256	0.338	0.316	0.275	0.367	0.292
Gd	1.463	1.384	1.043	1.390	1.153	1.112	1.561	1.200
Tb	0.246	0.243	0.179	0.226	0.216	0.197	0.266	0.197
Dy	1.731	1.638	1.188	1.622	1.404	1.422	2.021	1.404
Ho	0.360	0.338	0.243	0.330	0.278	0.289	0.414	0.277
Er	0.995	0.976	0.710	1.010	0.791	0.860	1.278	0.883
Tm	0.125	0.117	0.092	0.155	0.100	0.110	0.183	0.108
Yb	0.869	0.887	0.555	1.118	0.637	0.740	1.452	0.723
Lu	0.124	0.125	0.086	0.187	0.090	0.102	0.220	0.110
Hf	0.512	0.426	0.282	0.848	0.360	0.314	1.268	0.323
Ta	0.002	0.005	0.000	0.014	0.001	0.0002	0.028	0.001
Pb	0.541	0.721	0.163	1.589	0.337	0.291	2.933	0.771
Th	0.002	0.005	0.002	0.020	0.001	0.0004	0.054	0.003
U	0.002	0.002	0.001	0.008	0.0004	0.001	0.018	0.002